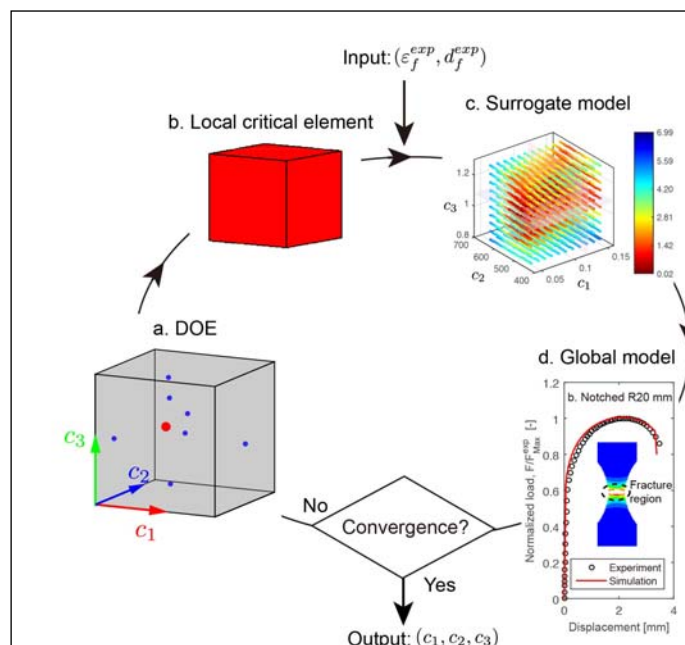


Par Yuliang HOU

*Modelling of plasticity and fracture behaviors of dual-phase steel*

Thèse présentée  
pour l'obtention du grade  
de Docteur de l'UTC



Soutenue le 26 octobre 2016  
**Spécialité** : Advanced Mechanics

D2302

# Modelling of plasticity and fracture behaviors of dual-phase steel

**Yuliang HOU**

Laboratoire Roberval, CNRS UMR 7337

Sorbonne Universités, Université de Technologie de Compiègne

This dissertation is submitted for the degree of

*Doctor of Advanced Mechanics*

26 october 2016

## Composition of the Jury

### Reviewers:

Sandrine THUILLIER, Université Bretagne Sud, France

Mario FAFARD, Université Laval, Canada

### Examiners:

Farid ABED-MERAIM, Ecole Nationale Supérieure d'Arts et Métiers, France

Jérôme FAVERGEON, Université de Technologie de Compiègne, France

Pierre CULIERE, ESI Group, France

Mohamed RACHIK, Université de Technologie de Compiègne, France (Supervisor)



Laboratoire **Roberval**  
Unité de recherche en mécanique





*I would like to dedicate this PhD thesis to my loving  
parents, sister and nephew.*





## Acknowledgments

First of all, I need to thank my supervisor, Prof. Mohamed Rachik, for offering me great insight and advice through my three years of PhD research at UTC. I highly acknowledge a lot for our countless discussions and his continuous guidance on scientific research and daily life. I also thank him for the freedom that he has granted me to pursue various research interests. He has always been encouraging and supporting me to participate academic activities, which expand my knowledge and enrich my experience. When I encountered horrible difficulties, he gave me his hands and made me feel the warmth of the world. I have learnt a lot from him during his supervision. This work is carried out in the “Spot weld project”, which is funded by ESI group. The scholarship of the “UT-CSC” program funded by the China Scholarship Council (CSC) is also highly appreciated.

I received many valuable help and comments from Pierre Culière, Alexandre Dumon and Chenfei Lu, who work in the Shanghai office of ESI group, during my PhD research. They provided me numerous quantities of solid experimental data and monthly discussions, which inspired me and validated my ideas. The time with them was truly joyful and unforgettable. I learnt the basics of being a good researcher from them. I am very thankful for them have always supported me to finish my PhD research.

I would like to express particular thanks to Thanethan Sapanathan, Liang Xia and Liang Meng for their passion and rigorous attitude in our collaboration, which continue to motivate me to pursue higher-quality researchers.

Additional thanks go to Prof. Sandrine Thuillier and Prof. Mario Fafard who have kindly agreed to review the work and also to all other members of my PhD thesis committee.

I would like to thank all my colleagues from *Laboratoire Roberval* in particular the members of *l'Équipe Numérique* who have either explicitly or implicitly helped me to attain the results in the present form. They have created a friendly atmosphere and have shared great mind together.

Last but not least I would like to express my thanks to all people outside of the scientific scope, namely my friends and my family. They offered me great support and

gave me lots of confidence, which encourage me to finish my PhD research during the past three years.

Compi ègne, August 2016

*Yuliang HOU*

## Abstract

Dual-phase (DP) steel has been developed by automotive industry for the purpose of weight reduction, improvement in safety performance and fuel efficiency. Usually, DP steel contains hard martensite islands embedded in a soft ferrite matrix. Synergy between these two phases with the inhomogeneous microstructure exhibits excellent mechanical properties. The mechanical properties (plasticity and damage behaviors) of DP steel are mostly derived from its microstructure, e.g., volume fraction, size, distribution and morphology of each constituent phase.

Micromechanical approaches are vastly applied to predict plasticity and other mechanical properties of DP steel under various loading scenarios. In this work, micromechanical modelling of DP steel has been performed using real or artificial microstructures. A real microstructure is obtained from metallographic image, while an artificial microstructure generator with an enhanced phase assignment algorithm based on material topology optimization is proposed to investigate the mechanical properties.

In this artificial generator, phase assignment process is performed on a modified Voronoi tessellation to achieve the tailored representative volume element (RVE) with a good convergence. The proposed method also includes a proper orthogonal decomposition (POD) reduction of flow curves (snapshots), which are computed using the asymptotic extension homogenization (AEH) scheme, to identify the optimal controlling parameters for DP steel. This numerical method is verified using DP590 and DP980 steels that indicate a good agreement with the flow stress from measurements and RVE prediction based on real microstructures. Predictions of plastic strain patterns including shear bands using the artificial microstructure closely resemble the actual mechanical behavior under similar loading conditions. Moreover, an interpolation has been adopted to obtain a correlation between these controlling parameters based on the identification for various DP steels.

Additionally, a bi-level reduced surrogate model is developed and presented to identify the material parameters of the Mohr-Coulomb (MMC) fracture criterion. Using this method, the identification process becomes feasible with a limited number of experimental tests. The method combines local critical elements associated with global models. The surrogate model of fracture strain constructed using the diffuse

approximation and the local elements, reduced the computational cost for searching material parameters. Global fracture simulations are performed to update the target fracture strain and to compute the corresponding failure onset displacement. Convincing results are obtained via successive application of design of experiment (DOE) and enhanced design space transformation algorithms. The proposed identification protocol is validated with DP590 steel. Robustness of the method is confirmed with different initial values.

These numerical investigations provide new direction for multiscale simulations of the plasticity and damage behaviors of DP steel. Moreover, they efficiently contribute to bridge the gap between scientific research and engineering application of heterogeneous materials.

## **List of publications related to the thesis**

- [J1] Y. Hou, T. Sapanathan, A. Dumon, P. Culière, M. Rachik, A novel artificial dual-phase microstructure generator based on topology optimization, Computational Materials Science, Volume 123, October 2016, Pages 188-200.
- [J2] Y. Hou, T. Sapanathan, A. Dumon, P. Culière, M. Rachik, Material parameter identification of the modified Mohr-Coulomb fracture criterion using bi-level reduced surrogate model, International Journal of Solids and Structures. (Under Review)

## **List of conference participations related to the thesis**

- [C1] Y. Hou, A. Dumon, P. Culière, M. Rachik, Calibration and Evaluation of Fracture Models of Dual-Phase Steel, 9<sup>th</sup> International Conference on Advanced Computational Engineering and Experimenting, Munich, Germany, 1<sup>st</sup> July 2015.
- [C2] Y. Hou, A. Dumon, P. Culière, M. Rachik, Micromechanical modelling of Multiphase Steel, 9<sup>th</sup> European Solid Mechanics Conference, Madrid, Spain, 9<sup>th</sup> July 2015.
- [C3] Y. Hou, A. Dumon, P. Culière, M. Rachik, Micromechanical modelling of dual-phase steel based on real/artificial microstructures, 40 ans de Mécanique Numérique, Compiègne, France, 26<sup>th</sup> November 2016.
- [C4] Y. Hou, 9<sup>th</sup> annual US-France symposium of the International Center for Applied Computational Mechanics, Compiègne, France, 1<sup>st</sup> June 2016.
- [C5] Y. Hou, A. Dumon, P. Culière, M. Rachik, Artificial microstructure generator for dual-phase steels, 7<sup>th</sup> European Congress on Computational Methods in Applied Sciences and Engineering, Crete Island, Greece, 5<sup>th</sup> June 2016.
- [C6] Y. Hou, M. Rachik, A. Dumon, P. Culière, Micromechanical modelling of dual-phase steel based on artificial microstructures, 12<sup>th</sup> World Congress on Computational Mechanics, Seoul, Korea, 24<sup>th</sup> July 2016.

## List of frequently used symbols

$\boldsymbol{\varepsilon}_p$	Plastic strain tensor
$\boldsymbol{\sigma}$	Cauchy stress tensor
$\mathbf{s}$	Deviatoric stress tensor
$\boldsymbol{\phi}_i$	$i$ -th eigenvector of $\mathbf{C}$
$\mathbf{a}$	Grain area vector in artificial RVE
$\mathbf{E}$	Correlation matrix of martensite islands' neighboring coefficient in artificial RVE
$(\mathbf{S}, \mathbf{C}, \mathbf{D})$	Snapshot matrix, covariance and deviation matrices of $\mathbf{S}$
$(\mathbf{S}_k, \tilde{\mathbf{S}}_k, \bar{\mathbf{S}})$	Original and reconstructed of $k$ -th flow stress snapshot, average flow stress snapshot
$\alpha_{ik}$	Projection coefficient of the $k$ -th snapshot on the $i$ -th eigenmode
$\beta$	Loading angle in bi-axial fracture experiments
$\gamma$	Amount of crystallographic slip
$\delta$	Positive move limit in topology optimization
$\Delta_j^k$	Distance for each pair of parallel edges of $k$ -th RVE
$\varepsilon(l)$	Reconstruction error used $l$ retained modes
$\varepsilon_f$	Fracture strain
$\varepsilon_M$	Equivalent plastic strain in the matrix material
$\bar{\varepsilon}_{ij}$	Global average strain tensor of RVE
$\bar{\varepsilon}_f$	Equivalent plastic strain at the onset of fracture
$\bar{\varepsilon}_p$	Equivalent plastic strain
$(\varepsilon_N, s_N, f_N)$	Void nucleation law parameters of GTN fracture model
$\zeta$	Numerical damping coefficient in topology optimization

$\eta$	Stress triaxiality
$\theta$	Macroscopic hardening factor
$\bar{\theta}$	Normalized Lode angle parameter
$\lambda$	Lagrangian multiplier
$\mu$	Shear modulus
$\xi$	Current microstructure state
$\rho$	Dislocation density
$\rho_0$	Initial dislocation density
$\sigma$	Flow stress
$\sigma_0$	Peierls stress
$\Delta\sigma$	Addition strength of precipitation or carbon in solution
$\Delta\sigma_\varepsilon$	Effects of dislocation strengthening
$\sigma_m$	Mean stress
$\sigma_n$	Normal stress
$\sigma_Y$	Yield stress of the principal phase material
$\bar{\sigma}$	Von Mises stress
$(\sigma_I, \sigma_{II}, \sigma_{III})$	Principal stresses
$\tau$	Shear stress
$\Phi_{GTN}$	Yield potential function of GTN fracture model
$w(\ \mathbf{c} - \mathbf{c}_k\ )$	Gaussian weighting function
$a$	Material constant in physically based model
$(A_0, A_f)$	Initial and fracture cross section areas of a specimen
$(A_M, A_T)$	Martensite and total phase area in artificial RVE



$\bar{A}$	Average cell area of Vorono itessellation
$b$	Burgers vector
$(c_1, c_2, c_3, c_\theta)$	Parameters of MMC fracture model
$C_M$	Neighboring coefficient of martensite grains
$(C_{SS}^F, C_{SS}^M)$	Carbon content in ferrite and martensite phases
$D$	Damage indicator of MMC fracture model
$(d_f, d_f^{exp})$	Predicted and measured fracture onset displacements
$f^*$	Modified damage parameter of GTN fracture model
$f_0$	Initial void volume fraction
$f_C$	Critical void volume fraction corresponding to the onset of coalescence
$f_F$	Void volume fraction corresponding to the onset of material fracture
$(\dot{f}, \dot{f}_G, \dot{f}_N)$	Total, growth and nucleation change of voids
$L$	Dislocation mean free path
$(L_{FM}, L_{MM})$	Length of specific ferrite-martensite and martensite-martensite boundaries in artificial RVE
$LSE.$	Least square error
$M$	Taylor factor
$N_{SS}$	Carbon content in DP steel
$p$	Penalty factor in topology optimization
$P_F$	Ferrite phase fraction
$P_M$	Martensite phase fraction
$Q_e$	Pseudo-density in topology optimization
$(q_1, q_2, q_3)$	Phenomenological fitting parameters of GTN fracture model
$s$	Standard deviation of cell area distribution of Vorono ï tessellation

$(u_i^{k-}, u_i^{k+})$	Displacement on the pair of parallel opposite edges of $k$ -th RVE
$(x_i, x_i^{k-}, x_i^{k+})$	Position vector from a reference point to a point on the RVE boundary

# Contents

<b>Part I. Plasticity</b>	<b>1</b>
<b>1. Introduction</b>	<b>2</b>
<b>1.1. Context</b>	<b>2</b>
<i>1.1.1 Automotive history</i>	<i>2</i>
<i>1.1.2 Development of new materials</i>	<i>3</i>
<i>1.1.3 Dual-Phase steels in automotive industry</i>	<i>5</i>
<b>1.2. Dual-Phase steels</b>	<b>5</b>
<i>1.2.1 Microstructures</i>	<i>5</i>
<i>1.2.2 Mechanical properties</i>	<i>7</i>
<b>1.3. Micromechanics</b>	<b>9</b>
<b>1.4. Research objectives</b>	<b>10</b>
<b>2. Literature review</b>	<b>12</b>
<b>2.1. Micromechanical modelling of Dual-Phase steels</b>	<b>12</b>
<b>2.2. Representative Volume Elements (RVEs)</b>	<b>13</b>
<i>2.2.1 RVEs based on real microstructure</i>	<i>14</i>
<i>2.2.2 RVEs based on artificial microstructure</i>	<i>16</i>
<i>2.2.3 RVE size and element size convergence</i>	<i>19</i>
<b>2.3. Prediction of flow curve of each single phase</b>	<b>20</b>
<i>2.3.1 Empirical models</i>	<i>20</i>
<i>2.3.2 Physically based models</i>	<i>21</i>
<b>2.4. Boundary conditions in micromechanics</b>	<b>23</b>
<i>2.4.1 Conventional boundary conditions</i>	<i>23</i>
<i>2.4.2 Periodic boundary condition (PBC)</i>	<i>24</i>
<b>2.5. Homogenization scheme</b>	<b>26</b>
<i>2.5.1 Homogenization method based on crystal plasticity</i>	<i>27</i>
<i>2.5.2 Asymptotic expansion homogenization (AEH) method</i>	<i>28</i>
<b>3. Micromechanical model based on real microstructure</b>	<b>28</b>
<b>3.1. Generation of RVEs</b>	<b>29</b>
<i>3.1.1 Acquisition process of real microstructure</i>	<i>29</i>
<i>3.1.2 Image analysis process</i>	<i>31</i>
<b>3.2. Calculation of flow curve of each single phase</b>	<b>33</b>
<i>3.2.1 Chemical composition measurement</i>	<i>33</i>

3.2.2 Flow curves	34
<b>3.3. Prescription of PBC</b>	<b>35</b>
<b>3.4. Homogenization process</b>	<b>37</b>
<b>3.5. Validation on tensile test analysis</b>	<b>38</b>
3.5.1 Micromechanical modelling of DP 590 steel	38
3.5.2 Micromechanical modelling of DP 600 steel	42
<b>3.6. Conclusions</b>	<b>45</b>
<b>4. Micromechanical model based on artificial microstructure</b>	<b>47</b>
<b>4.1. Artificial microstructure generator</b>	<b>47</b>
4.1.1 Modified Voronoï tessellation	47
4.1.2 Phase assignment algorithm based on topology optimization	50
4.1.3 Numerical examples	55
<b>4.2. Identification of controlling parameters using POD approach</b>	<b>56</b>
<b>4.3. Parametric study of artificial microstructure generator</b>	<b>58</b>
4.3.1 Identification of optimal controlling parameters	58
4.3.2 Benefits of RVE generation with the modified Voronoï tessellation	61
<b>4.4. Validation of the optimal artificial RVE</b>	<b>62</b>
<b>4.5. Relation between controlling parameters</b>	<b>66</b>
<b>4.6. Conclusions</b>	<b>68</b>
<b>Part II. Damage</b>	<b>71</b>
<b>5. Introduction</b>	<b>72</b>
<b>5.1. Background</b>	<b>72</b>
5.1.1 Damage problems	72
5.1.2 Damage of Dual-Phase steel	74
<b>5.2. Ductile fracture</b>	<b>75</b>
<b>5.3. Research objectives</b>	<b>78</b>
<b>6. Literature review</b>	<b>80</b>
<b>6.1. Ductile fracture criteria</b>	<b>80</b>
6.1.1 Gurson-Tvergaard-Needleman (GTN) fracture criterion	80
6.1.2 Modified Mohr-Coulomb (MMC) fracture criterion	82
<b>6.2. Calibration of ductile fracture criteria</b>	<b>86</b>
6.2.1 X-ray tomography techniques	86
6.2.2 Fracture tests and inverse calibration	88
<b>6.3. Combination of damage and micromechanics</b>	<b>94</b>

<b>7. Calibration process based on bi-level reduced surrogate model</b>	<b>97</b>
<b>7.1. Experimental work</b>	<b>98</b>
7.1.1 <i>Material description</i>	98
7.1.2 <i>Specimen and experimental procedure</i>	98
7.1.3 <i>Strain hardening parameters fitting</i>	100
<b>7.2. Surrogate model</b>	<b>101</b>
7.2.1 <i>Response surface methodology</i>	101
7.2.2 <i>Diffuse approximation</i>	103
<b>7.3. Bi-level modelling reduction strategy</b>	<b>104</b>
7.3.1 <i>Global finite element model</i>	105
7.3.2 <i>Local critical element</i>	105
7.3.3 <i>Adaptive correlation between fracture onset displacement and strain</i>	109
<b>7.4. Diffuse approximation of fracture strain prediction</b>	<b>110</b>
<b>7.5. Design and transformation of DOE</b>	<b>111</b>
<b>7.6. Validation on DP590 steel</b>	<b>112</b>
7.6.1 <i>Mesh dependency of MMC3 fracture criterion</i>	112
7.6.2 <i>MMC3 fracture criterion calibration for DP590 steel</i>	115
7.6.3 <i>Validation of robustness</i>	118
<b>7.7. Conclusions</b>	<b>121</b>
<b>8. Conclusions and perspectives</b>	<b>123</b>
<b>References</b>	<b>128</b>



## **Part I. Plasticity**

# **Chapter 1**

## **Introduction**

The physical phenomenon of plasticity occurs almost everywhere in our daily lives, such as the forming process of our beautiful plastic flowers from polymer particles, kids' plasticine, etc. Some of these plasticity phenomena are controlled by us and some others are spontaneous. Instinctively we, human beings, are exceptionally curious of the plasticity formation and process. The problem of the strength of materials has been one of the most active scientific fields since the establishment of modern science.

The industrial applications promoted the research of strength of materials. A number of new materials are produced and used in various new applications. Among various materials, metals were widely applied to build bridges, ships, land vehicles, railways, airplanes and various appliances. The strength and ductility of metals are greatly appreciated by the modern civilization. However, there are also such a number of unsolved problems in the metal ductility and plasticity. Theoreticians want to understand how the plastic phenomenon happens at the micro- or nano- levels. Practitioners on the other hand want to solve industrial problems, e.g., the sheet metal forming, the strength of car bodies, etc. Both of the theoreticians and practitioners have been the most active sources in the understanding related to plasticity.

### **1.1. Context**

#### ***1.1.1 Automotive history***

The blueprint for the modern automobile was perfected in France and Germany in the late 1800s [1]. And, since Americans revolutionized the automobile industry in the early 1900s [2], the car dominance in our daily lives has dramatically changed our habits and makes towns and cities much closer. But, the side effects accompanied with the lasting innovations in automotive industry, such as environment pollution, climate change, fossil fuel depletion, have settled new



challenges. Therefore, more recently, the economic crisis has pushed the car industry to reduce the weight of car body, and to improve energy saving considerations. In order to achieve these goals, it requires using lighter materials and lightweight structures.

The car from 1908 (Fig. 1.1a) still has the same mean features as today's concept, i.g., four wheels, front-engine, etc. But, the design and the efficiency are quite different compared to the modern model (Fig. 1.1b).

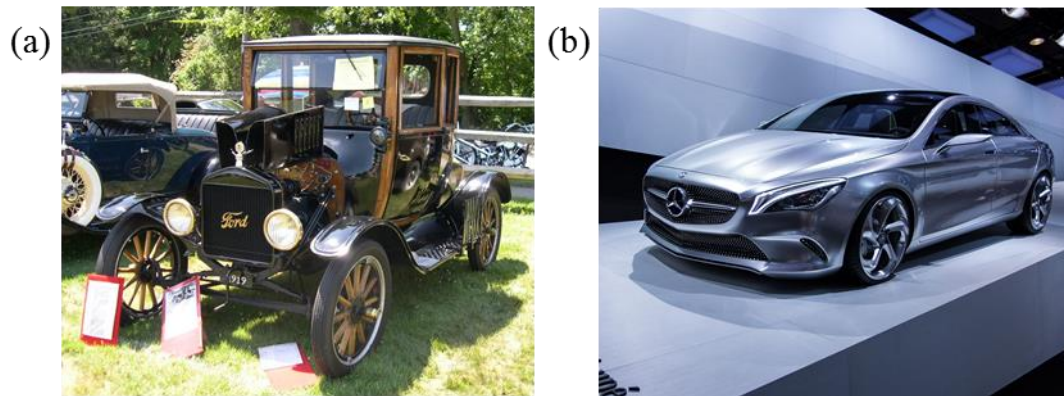


Figure 1.1: (a) Ford Model T from 1908 and (b) Mercedes-Benz concept style coupe (preview 2013 CLA-Class) at 2012 Paris Auto Show.

### ***1.1.2 Development of new materials***

In 1980s, carmakers are challenged to improve safety, to reduce fuel consumption and car bodies' weight. Advanced High-Strength Steels (AHSS) tremendously help them to meet requirements for safety, fuel efficiency, exhaust air pollution, manufacturability, durability, environment politics and quality as a relatively low cost [3].

According to steel manufacturers, AHSS are a new generation of steel grades which can provide extremely high-strength and other advantageous mechanical properties, while maintaining the high formability. And, AHSS have been used in industrial application for many years, but with additional research and development of AHSS, carmakers are using these steel grades in more applications.

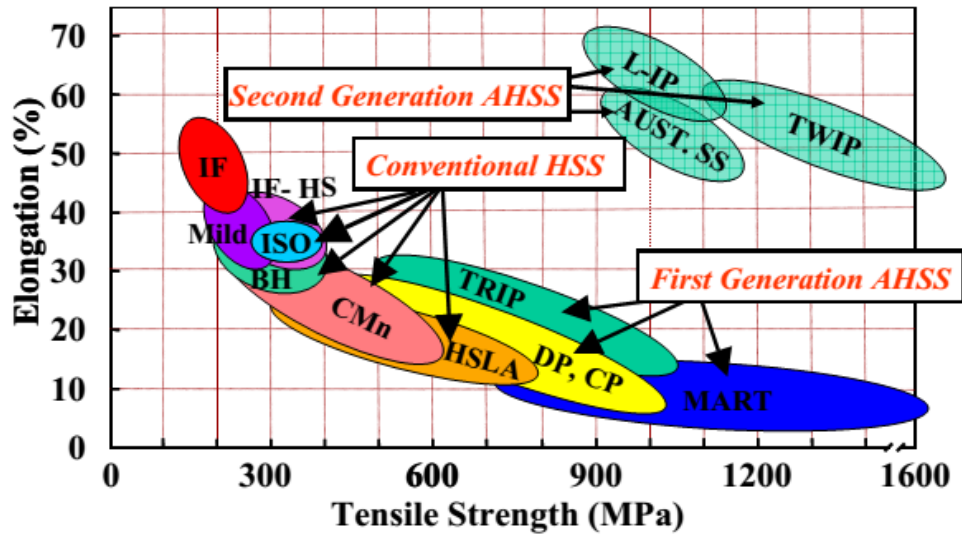


Figure 1.2: Tensile Strength-Elongation curve for low strength, conventional HSS and first generation AHSS steels [4].

A set of AHSS grades is shown in Fig. 1.2. In this figure, the ordinate describes the elongation in percent and the abscissa plots the tensile strength. This figure shows the particular combinations of material and mechanical properties in a banana form. And, most of the included materials result from tailored heating or cooling process.

Fig. 1.2 also describes a wide range of AHSS such as High-Strength Low-Alloy (HSLA), Dual-Phase (DP), Ferritic-Bainitic (DB), Complex Phase (CP), Martensitic (MART) and Transformation Induced Plasticity (TRIP) steels. The recent research is focusing on same grades of DP steels providing various mechanical properties. DP steel usually consists of hard martensite islands embedded in soft ferrite [5]. This special microstructure makes them exhibit several mechanical characteristics, such as relatively high ultimate tensile strength (UTS), low yield strength (YS) to tensile strength ratio and absence of yield point elongation. Therefore, in automotive industry, their excellent mechanical properties have provided benefits of reducing the weight of car body, improving passive safety feature, energy saving considerations and good formability.

By 2007, the average vehicle contained 11.6% medium- and high-strength steels, for a total steel vehicle content of 57% [3]. Due to the growing application of AHSS in practical, it has led to the investigation to improve its mechanical performance with less in quantity. Therefore, nowadays, the most challenging task for engineers is to select the material with the right combination of strength, ductility, toughness, and fatigue properties.

### 1.1.3 Dual-Phase steels in automobile industry

As mentioned above, DP steels are currently widely used in automotive industry. Automakers are increasingly employing DP steels to increase strength and down gauge HSLA structural components. What is important to consider when designing with DP steels, as with other AHSS, is the effect of strain and bake hardening. DP steels may be developed with low to high yield strength (YS) to ultimate tensile strength (UTS) ratios, allowing for a broad range of applications from crumple zone to body structure. DP is sometimes selected for visible body parts and closures, such as doors, hoods, front and rear rails. Other popular applications include: beams and cross members; rocker, sill, and pillar reinforcements; cowl inner and outer; crush cans; shock towers, fasteners, and wheels [6-8]. The applications of various grades of DP steels in automotive industry are shown in Fig. 1.3.

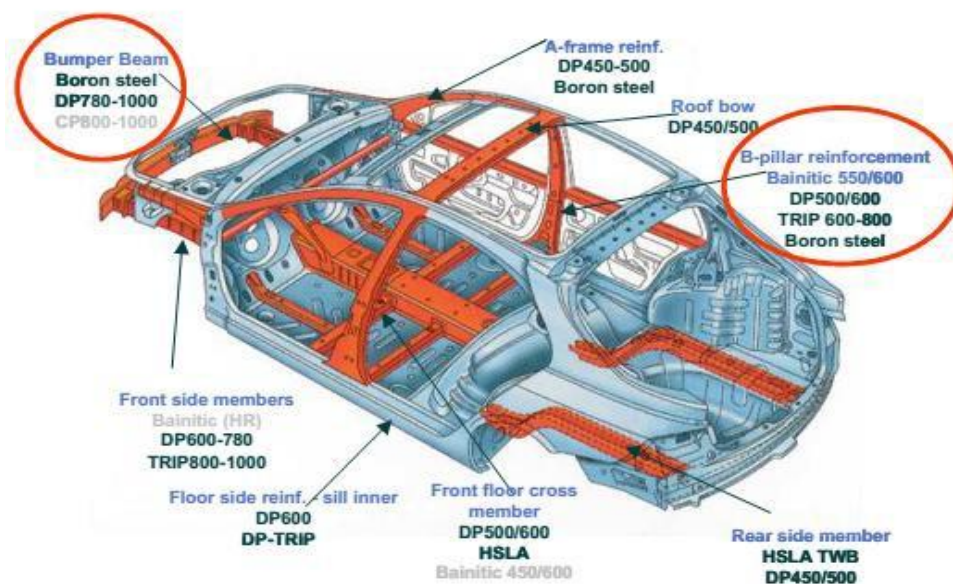


Figure 1.3: Applications of DP steels in automotive industry [6].

## 1.2. Dual-Phase steels

### 1.2.1 Microstructures

Most commonly, Dual-Phase steels, which contain special microstructure with hard martensite ( $\alpha'$ ) islands in a soft ferrite ( $\alpha$ ) matrix [9], have been extensively applied

in low carbon strips and structural steel for various industrial applications. Their very special microstructure provides an outstanding combination of strength and ductility. Fig. 1.4 represents SEM and TEM micrographs of typical DP steels' microstructure.

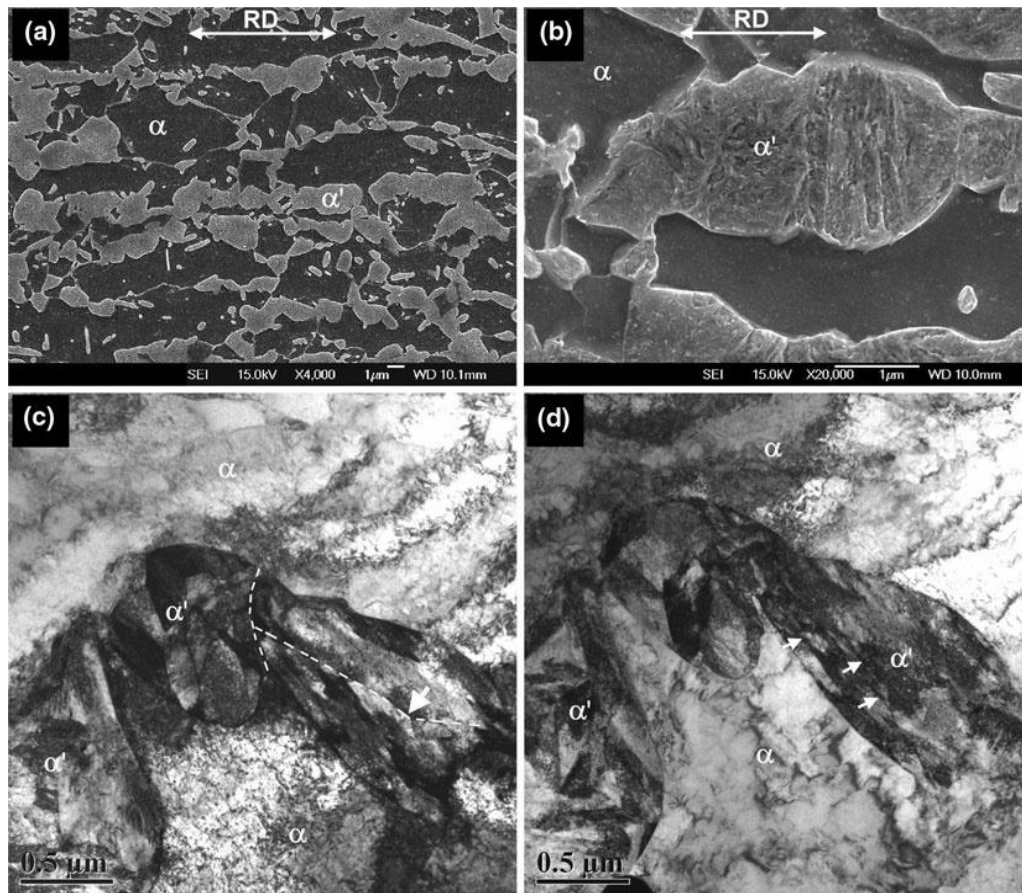


Figure 1.4: Micrographs of DP steels' microstructure, SEM: (a) ferrite  $\alpha$ -ferrite along with banded islands of martensite ( $\alpha'$ ), (b) sub-structure within  $\alpha'$  phase; TEM: (c) and (d) are taken at two tilt angles illustrating  $\alpha'$  phase and  $\alpha$  phase [9].

From the literature [3] and [10-11], the microstructure of DP steels is manufactured by inter critical heat operation of an initial ferrite/pearlite ( $\alpha + \text{Fe}_3\text{C}$ ) microstructure followed by an accelerated cooling as shown in Fig. 1.5. During the heating operation, the austenitic phase  $\gamma$  appears for a temperature  $\theta > A_1$ . The amount of austenite, being later the amount of martensite, is controlled by the temperature level comprised between  $A_1$  and  $A_3$ . The final quenching allows the transformation  $\gamma \rightarrow \alpha$  to take place, which could result in the final microstructure of DP steels.

Although the main part of the microstructure of DP steels is ferrite and martensite phase, sometime a small amount of residual austenite may appear after the heat

operation. This kind of residual microstructure could lead to an influence on the macro mechanical properties of DP steels. And, the presence of austenite phase reduces the martensite volume fraction and affects its distribution after the heat treatment as well. Several literatures [12-13] about experimental aspect have reported that the variation of the martensite quantity and the microstructural features of the martensite distribution have an important influence on the macroscopic behavior of the DP steel.

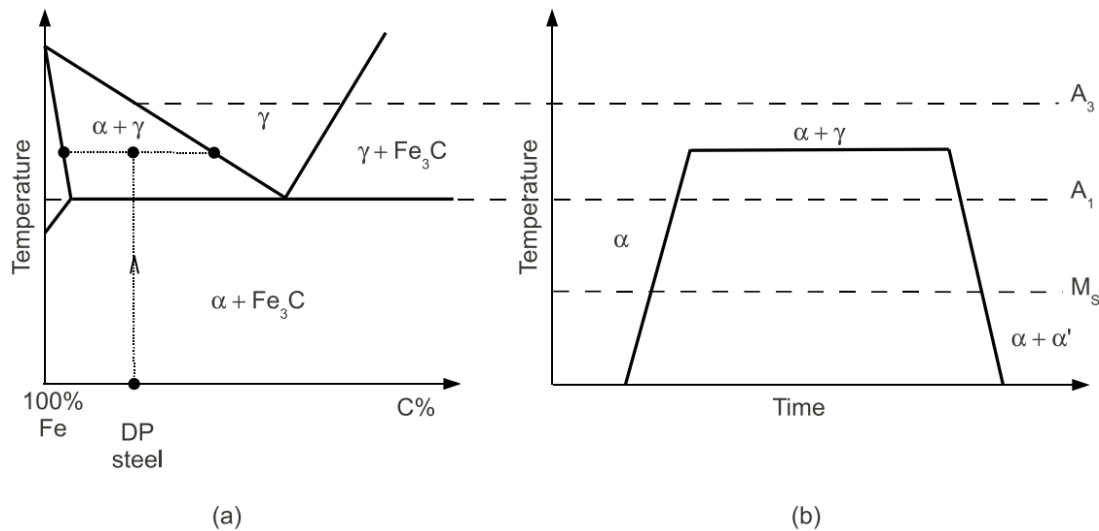


Figure 1.5: Thermal cycle of heat treatment to obtain a microstructure of DP steels: (a) schematic Fe-C diagram, (d) applied heat treatment [10].

### 1.2.2 Mechanical properties

As mentioned in last section, the variation of the martensite proportion and the microstructural features of the martensite distribution affect the macroscopic mechanical properties of the DP steel such as the tensile strength and the elongation. Table 1.1 summarizes the product property requirements for various types of DP steels, according to ArcelorMittal standard 20×80 mm ISO tensile specimens (thickness: less than 3mm) [14].

Steel grade	Yield Strength (YS) [MPa]	Ultimate Tensile Strength (UTS) [MPa]	Total Elongation [%]	Direction
-------------	---------------------------	---------------------------------------	----------------------	-----------

DP 450	280-340	450-530	$\geq 27$	Transversal
DP 500	300-380	500-600	$\geq 25$	Longitudinal
DP 600	330-410	600-700	$\geq 21$	Longitudinal
DP 780 Y450	450-550	780-900	$\geq 15$	Longitudinal
DP 780 Y500	500-600	780-900	$\geq 13$	Longitudinal
DP 980 Y700	700-850	980-1100	$\geq 8$	Longitudinal
DP 1180	900-1100	$\geq 1180$	$\geq 5$	Longitudinal

Table 1.1: Various types of DP steels and their mechanical property requirements [14].

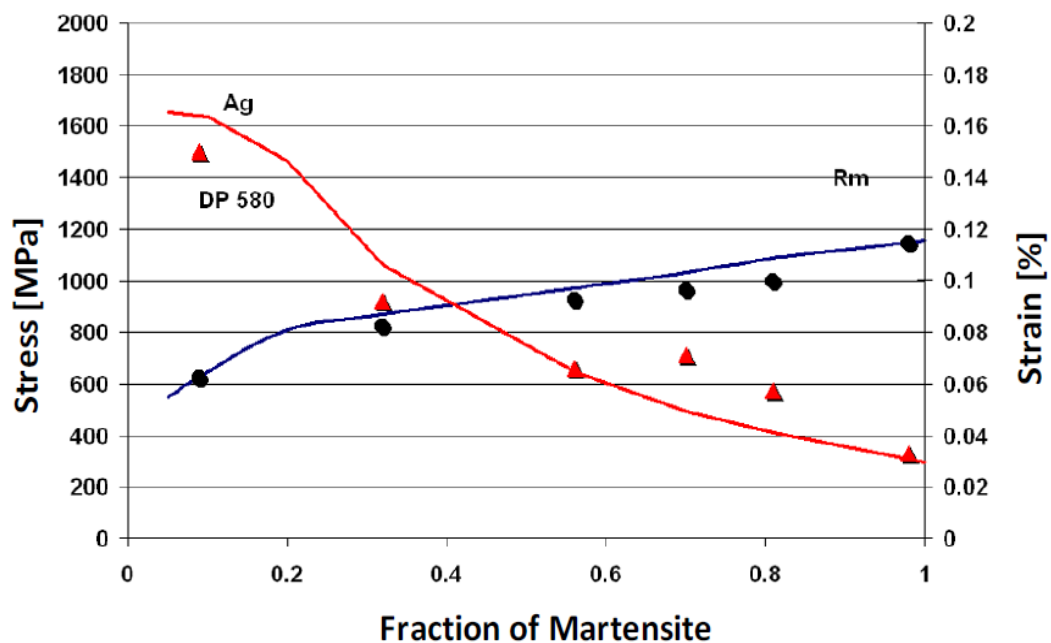


Figure 1.6: Mechanical properties in function of the volume fraction of martensite.  $R_m$  is the tensile strength and  $A_g$  the elongation for DP580 [15,16].

Fig. 1.6 shows the tendency of the mechanical properties in function of the volume proportion of martensite for the DP 580 steel (Chemical composition: Fe 0.09, C 1.9, Mn 0.1, Si 0.3, Cr 0.15, Mo) [15]. From this figure, it can be seen that, the tensile strength rises with the volume proportion of martensite increasing. But, the elongation declines while increasing the fraction of martensite.



In summary, due to the special dual phase microstructures in DP steels, they present an excellent candidate for the car body structural components. Usually, some safety parts in the car body, which maintain passenger surviving space in crash events, are produced by using DP steels. Also, the application of this kind of steel provides the possibility of reducing the weight of the vehicle.

### 1.3. Micromechanics

In the view of the special microstructures in DP steels, this kind of steels can be considered as heterogeneous materials at the micro level, which consist of clearly distinguishable phases (ferrite and martensite). From the results of several researchers [17-24], micromechanical modelling using numerical tensile test of a representative volume element (RVE) can be considered as an appropriate procedure to study and model the flow stress as well as damage of multiphase steels. As this procedure can provide a good description of the deformation of the material on the micro-scale giving insight into the stress and strain evolution and their distribution in the phases, it is very advantageous. However, a good RVE should be constructed so that the shape, morphology, size and randomness of constituent phases can be involved to be representative of the microstructure under consideration. Hence, the size of a well-quality RVE has to be sufficiently large to consist of the microstructural characteristics but also small enough for the stress-strain relation to be considered as homogeneous. The material on the macroscopic scale can be statistically homogeneous, and the FE model size must be at least as large as the RVE.

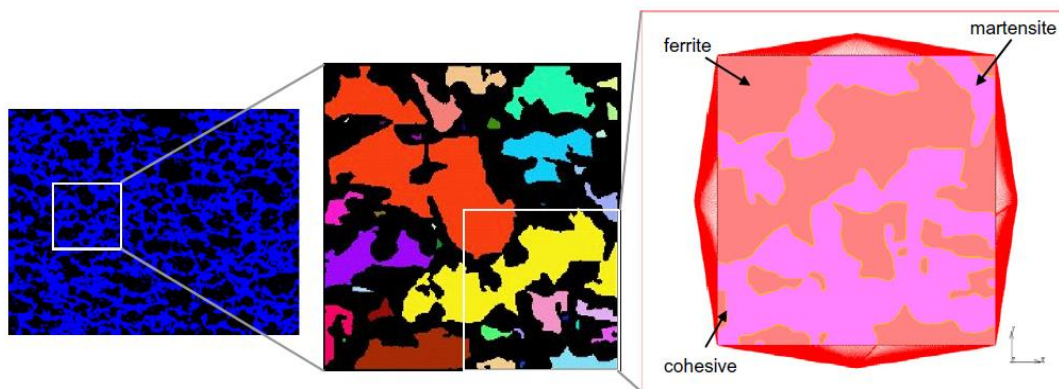


Figure 1.7: 2D RVE including cohesive elements of DP600 steel (left: micrograph, middle: enlarged image, right: FE RVE model with boundary conditions) [31].

Fig. 1.7 shows a 2D RVE selected to construct a finite element model including cohesive elements (for grain joint) of the DP600 steel based on real microstructure using metallographic images. This kind of images is fragmented into dissimilar parts with black and blue colors indicating the martensite islands and ferrite matrix respectively.

#### 1.4 Research objectives

A constitutive modeling of materials and structures framework has been proposed, and this PhD thesis is integrated into it. Under this framework, it plans to model and simulate the interactions between materials, processes and their usage properties. It includes 4 main parts, as shown in Fig. 1.8.

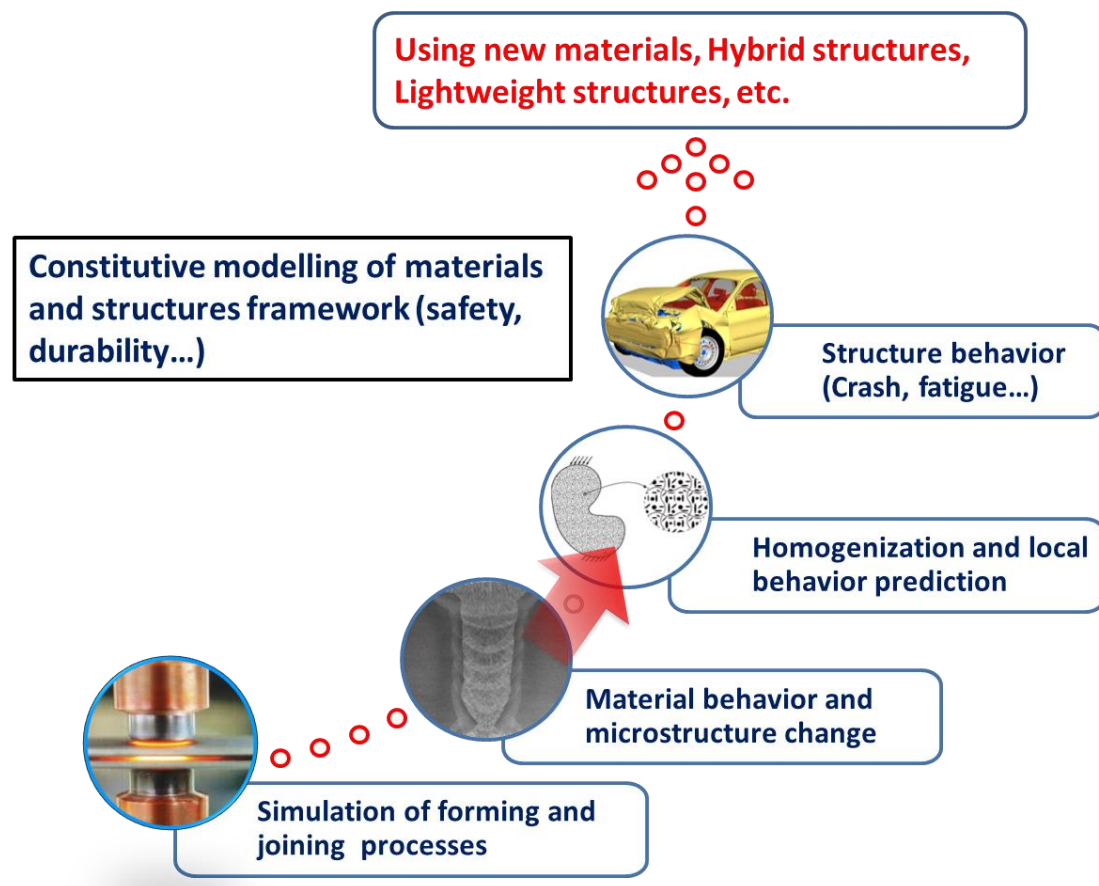


Figure 1.8: Constitutive modelling of materials and structures.

In order to ensure the usage of new materials, hybrid structures, lightweight structures in practical design, it is necessary to bridge the gaps between these parts. So, one goal of this research is to bridge the gap between the parts of “Material behavior and microstructure change” and “Homogenization and local behavior



prediction”. In other word, we need to compute the homogenized properties of materials which are generated from processes, based on the material behavior and microstructure change.

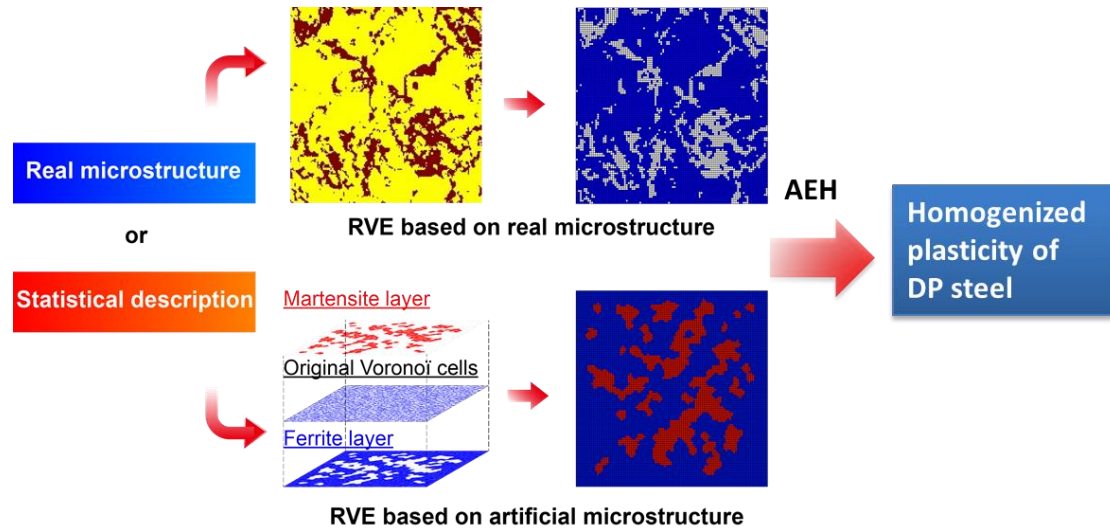


Figure 1.8: Illustration of the homogenization procedure of DP steel.

Therefore, the first goal of this research is to develop computer codes and models for the micromechanical modelling of DP steel based on real and artificial microstructures. From the flowchart as shown in Fig. 1.9, we can get details about this procedure: firstly, the real microstructures and statistical description of DP steel can be obtained from measurements; secondly, artificial microstructures are generated using topology optimization with pre-defined controlling parameters; thirdly, RVEs are constructed based on real and artificial microstructures; finally, the homogenized plasticity of DP steel is calculated using an asymptotic expansion homogenization (AEH) scheme.

## **Chapter 2**

### **Literature review**

The previous chapter presented DP steels as the coexistence of hard martensite islands embedded in soft ferrite matrix. This special microstructure makes them exhibit several mechanical characteristics, such as relatively high ultimate tensile strength, low yield strength to tensile strength ratio and absence of yield point elongation. In automotive industry, their excellent mechanical properties have provided benefits of reducing the weight of car body, improving passive safety feature, and energy saving considerations. The increasing demand by the market of steel products with enhanced mechanical behavior has led to the investigation of advanced engineering materials to improve their mechanical performance with less in quantity.

Therefore, this chapter will describe state of the art, which is focused on the microscopic approach. This approach physically describes the heterogeneity of plastic strain within the material. In addition, it allows understanding the material plastic deformation and validating the phenomenological approach.

#### **2.1. Micromechanical modelling of Dual-Phase steels**

Recently, many scientific researchers have done a lot of work to investigate the mechanical properties of DP steels by using micromechanics. From several researchers' technique reports [17,18,25], aiming to investigate tensile properties of DP steel, it has been concluded that the dislocation density accumulation along the grain boundaries leads to local hardening in the boundaries and hardening in the microstructure. Void initiation around martensite islands, void growth and coalescence inside ferrite matrix can be observed during the damage process. Cleavage cracking of martensite at low strain levels can be considered as the failure mode for harder embedded particles in DP steel. Since the microstructure of DP steel is affected by the chemical composition and the processing conditions. In previous experimental investigations, SEM graphs showed that the martensite phase in the DP590 and DP600 was island shaped; fractography indicated that the fracture

mode of DP steel is ductile failure with dimple appearance; the microcracks are then propagated along the ferrite/martensite interfaces.

Al-Abbasi and Nemes [26] developed a micromechanical model for DP steels, which are composed of martensite particles with two different sizes dispersed in a ferrite matrix. Accordingly, they reported that the strength of the RVE model increased with increasing the volume fraction of martensite. After that, several investigations with different boundary conditions have been done by Sun *et al.* [18]. It was found that the shear mode or split mode perpendicular to the loading direction can be considered as the final failure mode. Hosseini-Toudeshky *et al.* [27] studied the deformation pattern and mechanical behavior by using large and small deformation theories. In their work, the stress–strain behavior of DP600 was predicted by using a real microstructure-based RVE model. Ramazani *et al.* [21] applied periodic boundary conditions to calculate stress-strain curves for real microstructure-based RVE, and reported that the smaller RVEs prescribed with periodic boundary conditions was closer to the converged effective result. Recently, Uthaisangasuk *et al.* [22-24] used the real microstructure-based RVEs to investigate deformation and failure initiation at the micro level, emphasizing microcrack propagation in martensite by using extended finite element method (XFEM). All their investigations indicate that, the micromechanical modelling approach is a suitable method to simulate the local behaviors of DP steel.

After the microstructure modelling, in order to predict the mechanical behavior of dual-phase steels at the macro level, proper homogenization process need to be done. Nowadays, several homogenization procedures have been proposed. And, these approaches will be described in details in following chapter.

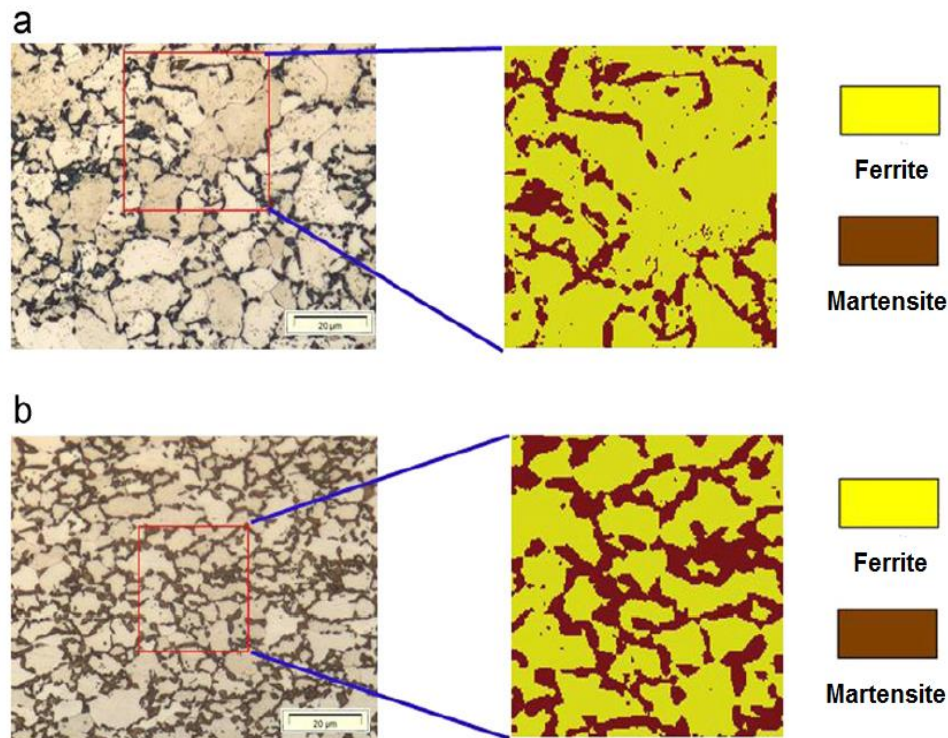
## **2.2. Representative Volume Elements (RVEs)**

As mentioned in previous chapter, micromechanical modelling using numerical analysis of tensile test of a representative volume element (RVE) can be considered as an appropriate procedure to study and model the flow stress of multiphase steels. Therefore, in this sub-section, the construction of RVEs based on real and artificial microstructures will be presented, and size convergence of RVEs and element size will be extensively discussed.

### 2.2.1 RVEs based on real microstructure

Generally, the real microstructure of the DP steel can be detected by taking light optical microscopy (LOM) images or scanning electron microscopy (SEM) graphs. In the study reported by Asgari *et al.* [28], 2D RVE based on DP real micrographs was generated by using a specialized meshing program OOF (Object Oriented Finite element analysis software [29]). After that, Ramazani *et al.* [21] have repeated this work, in which they converted real micrographs into 2D RVE by using an in-house program that makes use of the color difference of martensite and ferrite after etching. Fig. 2.1 shows several 2D RVE models based on real microstructure of DP600 steel with 20%, 37% and 46% martensite. From this figure, phase distribution and phase fraction of martensite and ferrite can be properly described in these 2D RVEs.

Although 2D RVE can satisfy the prediction of flow stress based on continuum mechanical assumptions, such as the plane strain and the plane stress conditions, while a 3D RVE can offer more reality in these predictions. Therefore, Ramazani *et al.* [30] later introduced 3D RVE constructed statistically with random distribution of martensite and ferrite phases. This kind of 3D RVE is cubic as shown in Fig. 2.2.



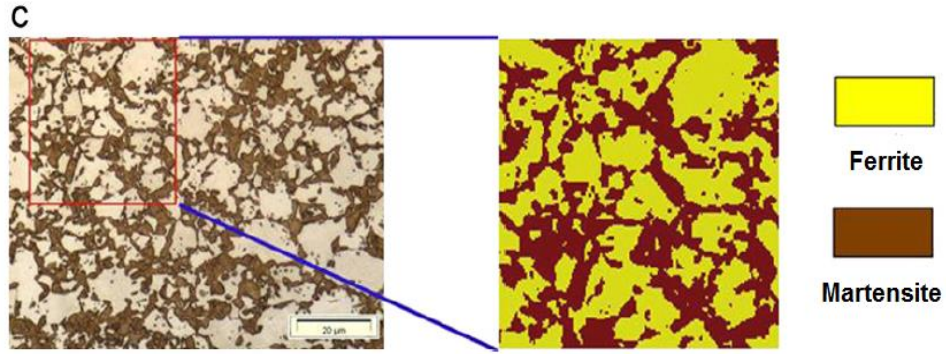


Figure 2.1: Examples of 2D RVEs based on real microstructure for micromechanical modelling of DP600 steel with (a) 20%, (b) 37% and (c) 46% martensite [30].

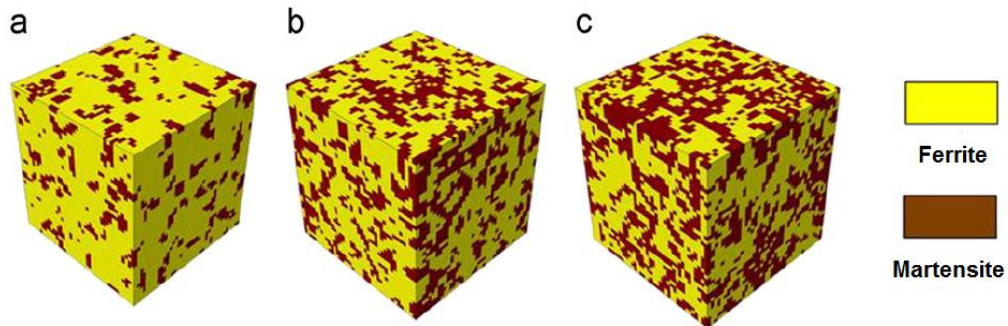


Figure 2.2: Examples of 3D RVEs based on static microstructure for micromechanical modelling of DP600 steel with (a) 20%, (b) 37% and (c) 46% martensite [30].

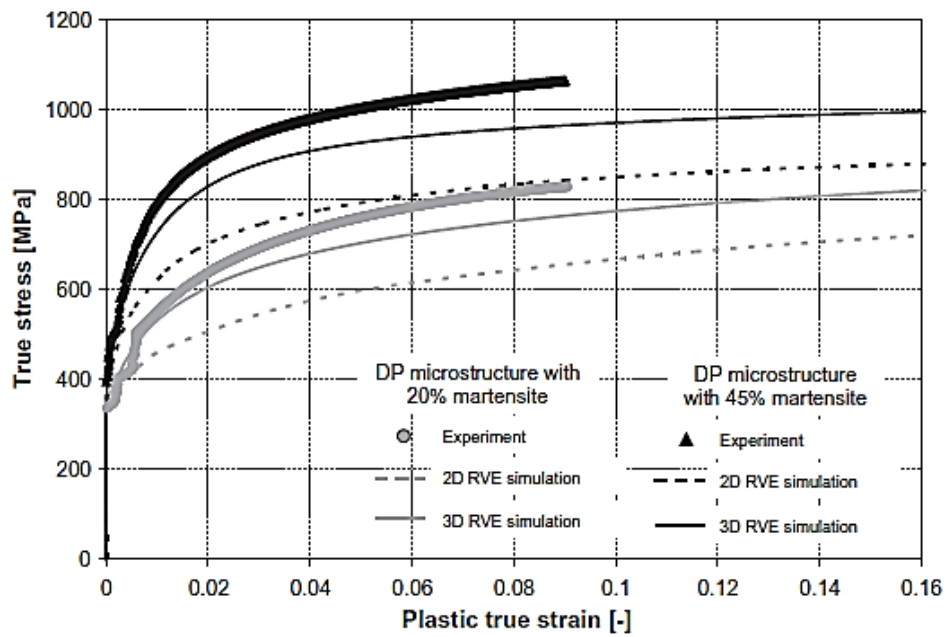


Figure 2.3: Comparison of true stress–strain curves from 2D and 3D RVE simulations of DP microstructures consisting of 20% and 45% martensite [31].

The size effect has been investigated by Uthaisangsuk *et al.* [31], they found that the stress-strain behavior of the 3D RVE is closer to the experimental flow curves than the one of the 2D RVE for both microstructures. Usually, the stress-strain curves were considerably underestimated by the 2D RVE simulations, in Fig. 2.3.

Moreover, the influence of the RVE model using plane-strain and plane-stress assumptions on the stress–strain behavior was studied. The plane-strain model exhibited lower flow stress compared to the plane-stress model, since in the plane-strain model the martensite particles are geometrically assumed to be long cylinders in a ferrite matrix, rather than a spherical particle in a cylindrical matrix. This effect increases with the martensite volume fraction [31].

### **2.2.2 RVEs based on artificial microstructure**

Real microstructure based models are constructed using experimental data to investigate the influence of grain morphology or size changes on effective properties of DP steel. However, highly heterogeneous materials are produced during industrial processing like welding, forging or heat treatments. They have special localized microstructures: microstructure at one material point could be different from another. For example, the welding zone formed during spot welding process can be divided into 3 regions: base material, heat affected zone (HAZ) and nugget [32]. In the HAZ, the microstructure is also dissimilar point-by-point, which is difficult to obtain experimentally. It is comparatively easier to use a computed artificial microstructure based on local phase proportions and chemical compositions to predict the flow stress of each material point. Accordingly, the local phase proportions and chemical compositions can be obtained from the phase transformation model incorporating concerned diffusion mechanisms [33–37]. Therefore, this method particularly requires the development of an artificial microstructure with similar statistical properties to replace the real one.

Based on statistical descriptions of DP steel, artificial microstructures are often generated using geometry primitives (e.g., spheres, polygons or polyhedra). Al-Abbasi and Nemes [38] developed a micromechanical model for DP steel, which consists of spherical martensitic particles with two different sizes in a ferrite matrix.



However, this model has disadvantages such as inexact geometric representation and no reliable data close to the interface between different phases.

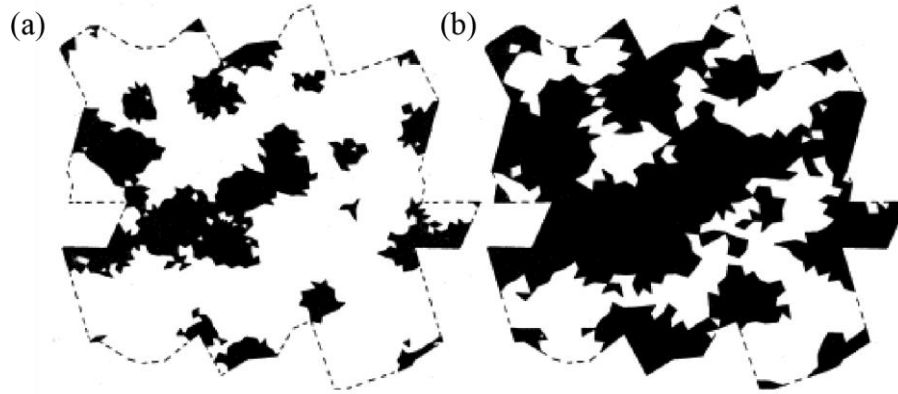


Figure 2.4: 2D periodic cells generated using Voronoi algorithm containing: (a) 25% and (b) 58% pearlite. The white and black areas represent the ferrite and pearlite phases, respectively [40].

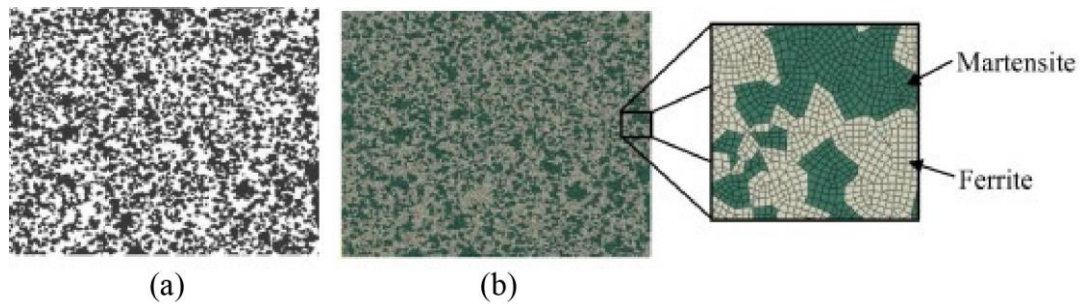


Figure 2.5: (a) 2D artificial RVE containing 40% martensite (black color) and (b) corresponding FE mesh with 980,000 nodes and 1,000,000 elements [42].

Alternatively, Voronoi tessellation [39] is considered as an efficient tool for approximating the microstructure in DP steel. Nygård *et al.* [40-41] modeled dual-phase microstructures using 2D (Fig. 2.4) and 3D periodic Voronoi tessellations with limited grain number to predict the effective mechanical properties. Due to the lack of an automate phase assignment algorithm, the second phase was just determined in a random grain growth way. Abid *et al.* [42] developed a random 2D RVE using Voronoi tessellation followed by an optimization and filtering algorithm to obtain tailored microstructures, as shown in Fig. 2.5. However, the used Voronoi seeds were sowed in a pseudo-random way, which underestimates the variability of the grain size, while overestimates the number of nearest neighboring cells. Moreover, their model is not suitable for RVEs with less than 100  $\mu\text{m}$  side length, since no periodicity exists in it. Fillafer *et al.* [43] simulated 3D microstructures

using periodic Voronoi tessellation and subsequent phase coloring to investigate the macroscopic stress-strain behavior of DP steel with different martensite fractions. In their work, the martensite contiguity was well considered and “soft” optimization criteria were used to reach the microstructure with predefined controlling parameters, as illustrated in Fig. 2.6. However, the randomness of the generating seeds was neglected and no more details of the “soft” criteria were given.

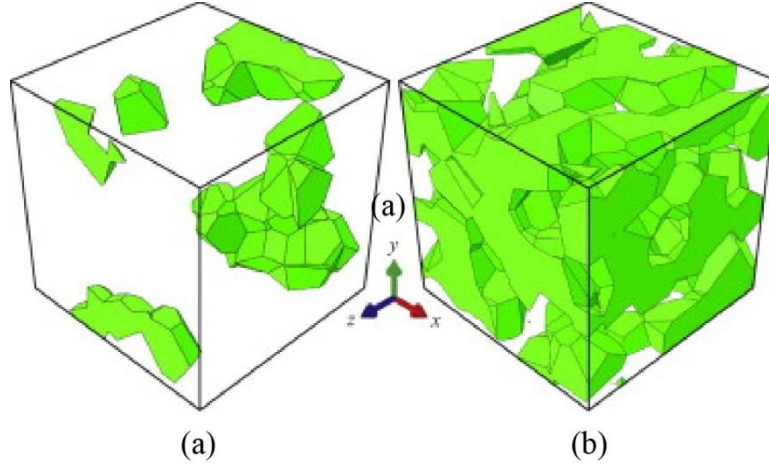


Figure 2.6: 3D periodic artificial RVEs generated using Voronoi algorithm and phase coloring process containing (a) 10% and (b) 50% martensite within 150 grains. Martensite and ferrite cells are shaded and transparent, respectively [43].

Although Voronoi tessellation is an adequate approximation for DP microstructure, the variability of grain size, shape and neighboring grains' correlation are affected by the design of generator seeds [44-45]. Moreover, typical existing phase assignment processes do not allow well capturing the complete features of DP microstructure and obtaining a convergent phase distribution. Therefore, in this work, a modified Voronoi tessellation is periodically generated from Halton (quasi-random) sequence [46], which statistically exhibits low discrepancy, to provide adequate grain morphology. A phase assignment algorithm based on material topology optimization has been proposed to solve the phase distribution problem.

Over the past few decades, a dramatic development of topology optimization has been performed in both scientific research [47-56] and industrial applications [57]. Various approaches including density-based methods [58,59], evolutionary procedures [60] and level-set methods [61,62], have been proposed to enhance the topology optimization design of multiscale nonlinear heterogeneous structures and topological design of microstructures of multi-phase materials. Originally, the



density-based topology optimization design technique can be regarded as a method that seeks the optimal structure to satisfy the given constraints, while minimizing the objective function, by defining a so-called “pseudo-density” within a fixed grid, as shown in Fig. 2.7. This is quite similar to the phase assignment procedure in artificial DP microstructure generation. Therefore, an algorithm related to density-based methods in topology optimization is introduced in our generator.

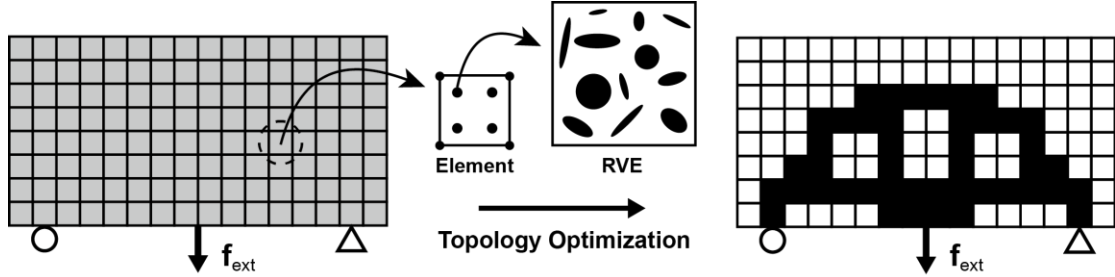


Figure 2.7: Illustration of the application of material topology optimization in multi-scale structure design [53].

Based on the combination of the modified Voronoi tessellation and enhanced phase assignment algorithm inspired by topology optimization, a novel artificial microstructure generator has been developed to build artificial RVEs with targeted parameters. This method also includes a proper orthogonal decomposition (POD) reduction [63, 64] of flow curves (snapshots) to identify the optimal controlling parameters for DP steel. This numerical method significantly improves the representativity of the generated RVE with low computational cost. The proposed method is verified using a DP590 steel which indicates a good agreement between the measurements and the predictions from RVE based on real microstructures [65-66].

### 2.2.3 RVE size and element size convergence

As this micromechanical simulation by using RVE can provide a good description of the deformation of the material at the micro level giving insight into the stress and strain evolution and distribution in the phases, it is very advantageous. However, a good RVE should be constructed based on a way that the shape, morphology, size and randomness of constituent phases can be involved to be representative of the microstructure under consideration. Hence, the size of a well-quality RVE has to be sufficiently large to consist of the microstructural characteristics but also small enough for the stress-strain relation to be considered as homogeneous. The material

on the macro scale can be statistically homogeneous, and the FE model size must be at least as large as the RVE.

From the study by Ramazani *et al.* [21,30], the acceptable size of RVE was considered as minimum as 24  $\mu\text{m}$  while it can include at least 19 martensite islands [30]. Therefore, 2D RVEs with dimensions of  $25 \times 25 \mu\text{m}$  and 3D RVEs with dimensions of  $25 \times 25 \times 25 \mu\text{m}$  as respectively shown in Figs. 2.1 and 2.2, are considered. Additionally, the effect of mesh size is studied by some researchers with element size ranging from 0.1 to 2 mm, and no deviation is obtained for the meshes finer than 0.25 mm.

### 2.3. Prediction of flow curve of each single phase

In the finite element analyses of dual-phase steel, the stress-strain relation of each single phase is an important issue. Nowadays, there are two main methods to predict the flow curve of each single phase in the DP steel: (i) Empirical models and (ii) Physically based models. These two approaches are discussed in the following subsections.

#### 2.3.1 Empirical models

The implementation of RVE models for multiphase steels requires the mechanical behavior (stress-strain curve) for each phase to be determined as accurately as possible. The first experimental approach is to prepare several specimens which are individual phase (ferrite and martensite), and to perform tensile tests on these specimens. With the recorded stress-strain relation, it is possible to fit these flow curves by using empirical equations.

The most popular formulation based on empirical equations is Swift equation:

$$\sigma = K \left( \varepsilon_0 + \bar{\varepsilon}^p \right)^n \quad (2.1)$$

where  $K$ ,  $n$  and  $\varepsilon_0$  are material parameters.

The limitation of these models is the reduced applicability, as they are based on fitted parameters that cannot easily be extrapolated to other conditions. For ferrite this has been overcome to a certain level relating the exponent  $n$  to the grain size and to composition. However, when the degree of complexity of the steel

microstructure increases, the applicability of these empirical equations is reduced. In some cases, the use of different  $n$  values is required in order to fit the flow curve over the entire deformation range.

### 2.3.2 Physically based models

An alternative to the empirical equations is the use of physically based models that link to both the micro and the macro scales and are expected to give more accurate prediction. Different dislocation based models can be found that have some differences in the formulation but all of them relate the strain hardening to the balance between the dislocation storage and recovery [67].

The macroscopic flow stress  $\sigma$  and the plastic strain  $\varepsilon$  are related to the critical resolved shear stress for current microstructure state  $\xi$  and the amount of crystallographic slip  $\gamma$  via an orientation factor,  $M$  as:

$$\sigma = M\xi \text{ and } Md\varepsilon = d\gamma \quad (2.2)$$

Assuming an average behavior, the microscopic hardening rate of the crystalline element,  $\theta$  can be related to the macroscopic hardening as:

$$\theta = \frac{d\xi}{d\gamma} = M^{-2} \frac{d\sigma}{d\varepsilon} \quad (2.3)$$

The classical relation between the flow stress and the total dislocation density can be expressed as:

$$\sigma = \sigma_0 + \Delta\sigma + \Delta\sigma_\varepsilon = \sigma_0 + \Delta\sigma + \alpha M \mu b \sqrt{\rho} \quad (2.4)$$

The first term  $\sigma_0$  reflects the Peierls stress and the effects of alloying elements in the solid solution. The second term  $\Delta\sigma$  provides strengthening by precipitation or the carbon in solution. The third term  $\Delta\sigma_\varepsilon$  consists of the effects of dislocation strengthening as well as work softening due to recovery, with  $\alpha$  a constant,  $M$  the Taylor factor,  $\mu$  the shear modulus,  $b$  the Burgers vector and  $\rho$  the dislocation density.

During deformation, the evolution of the dislocation density with strain is generally split into two parts:

$$\frac{d\rho}{d\gamma} = \left( \frac{d\rho}{d\gamma} \right)_{\text{stored}} + \left( \frac{d\rho}{d\gamma} \right)_{\text{recovery}} \quad (2.5)$$

The substitution  $Md\varepsilon = d\gamma$  in Eq. (2.5) allows expressing the change in dislocation density as a function of the macroscopic equivalent strain. Different expressions have been proposed for each term. Usually, it can be considered that:

$$\frac{d\rho}{d\varepsilon} = M \left( \frac{1}{bL} - k_r \rho \right) \quad (2.6)$$

where  $k_r$  is the recovery rate and  $L$  is the dislocation mean free path which can be considered proportional to the average spacing of the homogeneously distributed dislocation.  $\rho$  can alternatively be defined by some microstructural parameter like the subgrain size, the interparticle spacing or the grain size. The resulting equations and the results of the integration, considering  $\rho_0$  as being initial dislocation density in the deformation free material give different results, depending on the chosen option. After integration and substitution into Eq. (2.4), it will have results:

$$\rho = \frac{1}{bLk_r} [1 - \exp(-k_r M \varepsilon)] + \rho_0 \exp(-k_r M \varepsilon) \quad (2.7)$$

$$\Delta\sigma_\varepsilon = \alpha M \mu \sqrt{b} \sqrt{\frac{1}{bLk_r} [1 - \exp(-k_r M \varepsilon)] + \rho_0 \exp(-k_r M \varepsilon)} \quad (2.8)$$

The above formulation has been applied in order to predict the flow stress for different steel micro-constituents. The application of these equations to the experimentally determined tensile curves requires some fitting exercise to determine the involved parameters. The practical result is that, regardless of the approach being used, it is possible to predict with enough precision the tensile curve, by the correct selection of the parameters involved in the equations to the main characteristics of each particular microstructure. Generally, since the initial dislocation density before deformation is pretty low, the following equation can be used:

$$\sigma = \sigma_0 + \Delta\sigma + \alpha M \mu \sqrt{b} \sqrt{\frac{1 - \exp(-Mk_r \varepsilon)}{k_r L}} \quad (2.9)$$

It is a simplified form of Eq. (2.4) and Eq. (2.8). In this equation, there is some uncertainty concerning the value of  $\alpha M$ . This term can strongly affect the strain hardening contribution to the overall result of the modelling. For the case of ferrite, factors of variation can be found as high as 1.8. In recent research [21,68,69],  $\alpha=0.3$  and  $M=3$  have been adopted for the different microstructures and consequently remain out of the required fitting exercise to the experimental tensile curves.

## **2.4. Boundary conditions in micromechanics**

In general, computational homogenization procedures are needed with the adequate construction and solution of a boundary value problem, since the derivation of the local macroscopic constitutive response from an underlying microstructure. And for now, most of the homogenization approaches make an assumption on the global periodicity of the microstructure, which considers that the whole macroscopic specimen consists of spatially repeated unit cells. To study the effect of the boundary condition, RVEs have been studied under uniaxial tensile straining with conventional boundary conditions (i.e. linear displacement or constant traction boundary conditions) and periodic boundary condition (PBC). This section will describe these different types of boundary conditions.

### **2.4.1 Conventional boundary conditions**

There are two main kinds of conventional boundary conditions, which are widely used in micromechanical modelling with RVEs: (i) linear displacement boundary condition (Dirichlet condition); (ii) constant traction boundary condition (Neumann condition). From the study of Terada *et al.* [70], it was reported that, as the RVE size decreases, estimation of the homogenized mechanical properties becomes worse. Therefore, it is necessary to build RVEs with relatively large dimensions. This will dramatically increase the computational time and decreases its efficiency. In the following section, description of periodic boundary condition will be presented in details.

### 2.4.2 Periodic boundary condition

Periodic boundary conditions (PBC) are a set of boundary conditions which can be chosen for approximating a very large even an infinite system or part by using a small and representative part or element. This kind of boundary conditions is usually used in numerical simulations and mathematical models. The large systems approximated by PBC only consist of infinite number of volume elements, and these elements must have the capability to describe the general characters of the large systems. For example, the topology of two-dimensional PBC can be considered as a global map of polycrystalline or multiphase steels, the geometry of these volume elements satisfies perfectly two-dimensional tiling, and when a physical field (e.g. Strain or Stress) passes through one side of the element, it re-appears on the opposite side with the same magnitude.

Two-dimensional PBC are often applied to simulate planar surfaces, and it could be called slab boundary conditions; in this case, PBC are used under the coordinate frame with two Cartesian coordinates (e.g.  $x$  and  $y$ ), and the third coordinate ( $z$ ) could remain zero to infinity. And in simulation of solid systems, the strain field arising from any inhomogeneity in the system will be artificially truncated and modified by the periodic boundary. The dimension of RVE used as the simulation box must be large enough to prevent periodic boundary artifacts from occurring due to the unphysical topology of the simulation.

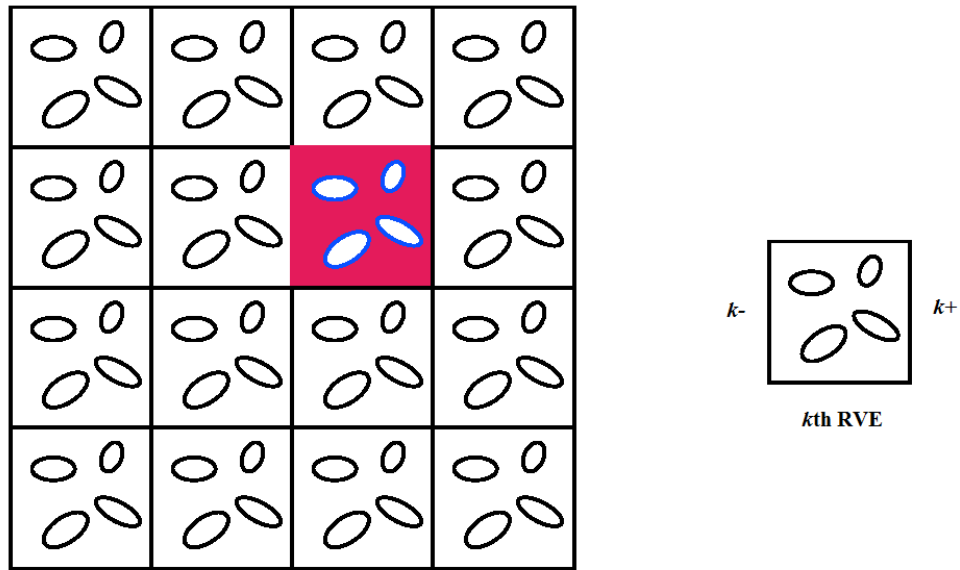


Figure 2.8: A 2D periodic structure and the  $k$ -th RVE.

One kind of unified displacement-difference periodic boundary conditions has been proposed by Xia *et al.* [71]. The displacement field for the global level structure can be expressed as in the following equation:

$$u_i(x_1, x_2, x_3) = \bar{\varepsilon}_{ij} \cdot x_j + u_i^*(x_1, x_2, x_3) \quad (2.10)$$

where  $x_i$  is a position vector from a reference point to a point on the boundary, and  $\bar{\varepsilon}_{ij}$  is the global average strain tensor of the periodic structure. The first term on the right side is a linear distributed displacement field, and the second term,  $u_i^*(x_1, x_2, x_3)$  represents a periodic function from one RVE to another nearby. It means a modification to the linear displacement field due to the heterogeneous structure.

Since the periodic array of the RVEs (in Fig. 2.8) represents a continuous physical body, the continuity of displacement and stress must be satisfied. For the displacement continuity, in the  $k$ -th RVE (in Fig. 2.8), the displacement on a pair of parallel opposite edges could be written as:

$$u_i^{k-} = \bar{\varepsilon}_{ij} x_j^{k-} + u_i^* \quad (2.11)$$

$$u_i^{k+} = \bar{\varepsilon}_{ij} x_j^{k+} + u_i^* \quad (2.12)$$

where indices “ $k+$ ” and “ $k-$ ” represent the  $k$ -th pair of two opposite parallel edges of an RVE (in Fig. 2.8). Since both the parallel edges are in the same RVE, then difference between the two displacements could be expressed as:

$$u_i^{k+} - u_i^{k-} = \bar{\varepsilon}_{ij} (x_j^{k+} - x_j^{k-}) = \bar{\varepsilon}_{ij} \Delta_j^k \quad (2.13)$$

where  $\Delta_j^k$  are constants for each pair of the parallel edges, with specified value of  $\bar{\varepsilon}_{ij}$ ,

then, the right side becomes constants and such equations can be easily applied in the finite element (FE) analysis as a series of nodal displacement constraint equations. Eq. (2.13) is a special type of displacement boundary conditions. It doesn't give known values of boundary displacement, but specifies the constraint of the displacement difference between two opposite edges. Obviously, the application of PBCs can guarantee the continuity of global displacement field. But, this equation

may not be complete or may not guarantee the traction continuity conditions. The traction continuity conditions can be expressed as:

$$\sigma_N^{k+} - \sigma_N^{k-} = 0, \quad \sigma_T^{k+} - \sigma_T^{k-} = 0 \quad (2.14)$$

where  $\sigma_N$  and  $\sigma_T$  are normal and shear stresses at the corresponding parallel edges, respectively. For general boundary value problems, the Eq. (2.13) and Eq. (2.14) constitute a complete set of boundary conditions.

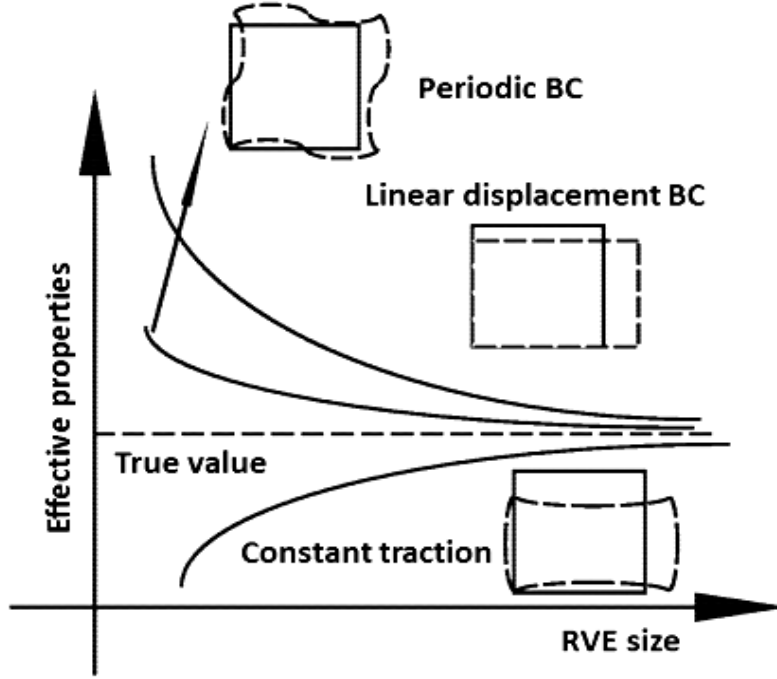


Figure 2.9: Comparison of different boundary conditions [70].

Fig. 2.9 clearly shows that, for all these three boundary conditions, the increase of the RVE size leads to a better estimation of the effective properties [70]. But for a given RVE size, the periodic boundary condition provides a better estimation than the two other boundary conditions. In other words, PBC is the most efficient one in terms of convergence rate as the RVE size increases. Therefore, the boundary condition applied to this micromechanical model is PBC.

## 2.5. Homogenization scheme

In order to describe material behavior of the DP steel, different models on micro- and macro-scale need to be created. At the micro level, micromechanical models, such as RVE models, have considered multiphase materials as heterogeneous. At the macro level, models with the same geometry and size of work piece can be easily



constructed, and these models should be defined with the global homogeneous material properties, which are obtained from the local micro-scale simulation. Therefore, a homogenization process is necessary to represent the macroscopic material behavior from the results of the RVEs' numerical predictions. In the work of former researchers, two major types of homogenization methods have been described, the crystal plasticity based models [72-75] and the asymptotic expansion homogenization (AEH) method [76,77].

### ***2.5.1 Homogenization method based on crystal plasticity***

The first homogenization method belongs to the analytical methods of continuum micromechanics. Among the analytical methods, the mean-field homogenization models [73,74] and the variational bounding models are the most widely used. In the mean field methods, the stress field in each phase is considered as approximately their mean values. Moreover, they use the information of the microstructure topology, geometry, and orientation of the inclusions and, possibly, statistical information of the phases distribution. And the variational bounding methods are used to obtain upper and lower bounds to the elastic tensor and other mechanical properties of heterogeneous materials.

Many mean-field methods used in the micromechanical modelling of materials are built on the work of Eshelby [78]. A better approach to determine the strain localization tensor is to use Eshelby's analytical solution to handle the inhomogeneity problem. He introduced the equivalent inclusion theory in order to solve the strain localization problem for a single inhomogeneity embedded in an infinitely large matrix (in the DP steel, ferrite phase could be the majority phase). Hence, his solution can be used only for dual-phase metallic materials. And in his theory, when the matrix properties are isotropic and the inclusion has an ellipsoidal shape, the localized stress and strain fields in the inclusion are uniform. In the work of Tanaka and Mori [73], a simpler approach, has been proposed based on the Eshelby theory, for metal matrix composite (MMC) materials. In this homogenization scheme, it is assumed that the inclusions in the RVE, experience the matrix strain as the far-field strain in the Eshelby theory.

### ***2.5.2 Asymptotic expansion homogenization method***

From a mathematical view, this theory of homogenization is a limit theory that uses the asymptotic expansion and the assumption of periodicity to substitute the differential equations with rapidly oscillating coefficients, with differential equations whose coefficients are constant or slowly varying in such a way that the solutions are close to the initial equations [79].

The AEH method is based on the multiscale perturbation theory, and it is usually used in the global/local and periodical problems. The advantage of this method is that it can solve micro-stress field problems for general loading conditions. Moreover, the local FE analysis is relatively independent of global analysis and only periodic boundary conditions are necessary during FEM analysis.

The use of this approach requires specific boundary conditions prescribed to assure the perfect tiling between adjacent RVEs. Then, the above-mentioned PBCs can make the use of the translator symmetries of geometry to handle any physically valid deformation state of RVEs. Based on the AEH approach, the homogenized stress and strain are given by a computational first-order homogenization by volume fraction averaging. In the general FEM codes, this homogenization process can be implemented easily and directly.

## Chapter 3

### Micromechanical model based on real microstructure

In this chapter, the complete process of micromechanical modelling of DP steels will be presented in details. 2D RVEs are generated based on real microstructures. With an in-house image analysis program that works on the color difference of martensitic and ferritic cell, corresponding finite element model can be constructed. The flow stress of each single phase can be computed by using the dislocation based theory as described in section 2.3.2. Then, the micromechanical simulation can be done with the prescription of PBC. And, the homogenized macroscopic flow stress of DP steels can be obtained.

In addition, the whole micromechanical modelling will be validated on tensile tests of two DP steels: (i) DP590 steel (from ESI-Group) and (ii) DP600 steel (from literature [30]). Results and comparisons will be presented in the last section.

#### 3.1. Generation of RVEs

As described in section 2.2.1, 2D RVEs are selected to construct a finite element model of the DP590 steel with real microstructure using metallographic images. This kind of images is fragmented into dissimilar parts with black and blue colors indicating the martensite islands and ferrite matrix respectively as shown in Fig. 1.7. As mentioned above, the size of RVEs has a significant influence on the simulation results. From the work of Ramazani *et al.* [21], the acceptable size of the RVE is considered as a minimum of 24  $\mu\text{m}$  while it can include at least 19 martensite particles. Therefore, in this study, 2D RVE models with a size of 25  $\times$  25  $\mu\text{m}$  have been used.

##### 3.1.1 Acquisition process of microstructure

The microstructures of DP steels provided by metallography are shown in Figs. 3.1 and 3.2. These metallographical pictures can be acquired by SEM (in Fig. 3.1) or LOM (in Fig. 3.2) after samples' etching with 3% Nital solution. The patterns of the microstructure show martensite islands dispersed evenly in the ferrite matrix.

Fig. 3.1 shows the details of SEM microstructure for the investigated DP590 steel. It was taken by using a SEM machine FEI-Quanta FEG250. In this figure, two different parts can be distinguished: (i) ferrite phase (black and gray colors) and (ii) martensite phase (white color). And, the volume fraction of martensite can be calculated from this image. It was found that the investigated material contains about 22% martensite and 78% ferrite. The LOM microstructure of cold-rolled DP600 steel and its rolling direction is illustrated in Fig. 3.2. In contrary, the white part indicates ferrite phase and the black indicates martensite phase. The volume fraction of martensite in this DP600 steel is 20%. Here, it is worth noting that the grain boundaries between ferrite and martensite should be distinguished to achieve an accurate model along the ferrite and martensite interface. The coordinate of grain boundary points can be obtained from an image analysis, which will be presented in the following section.

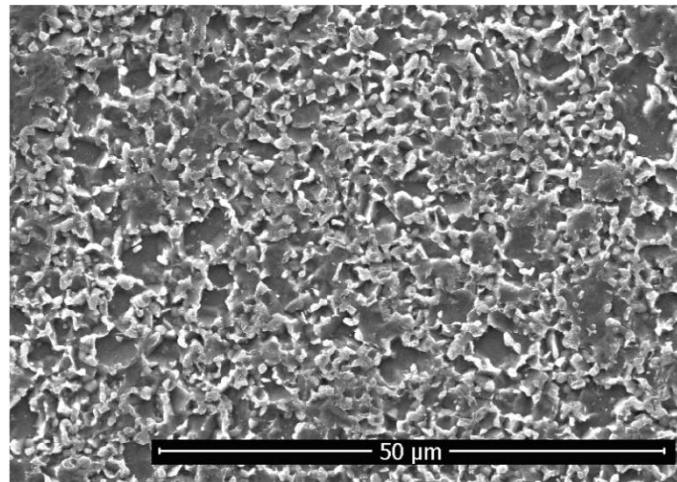


Figure 3.1: SEM microstructure of the investigated DP590 steel.

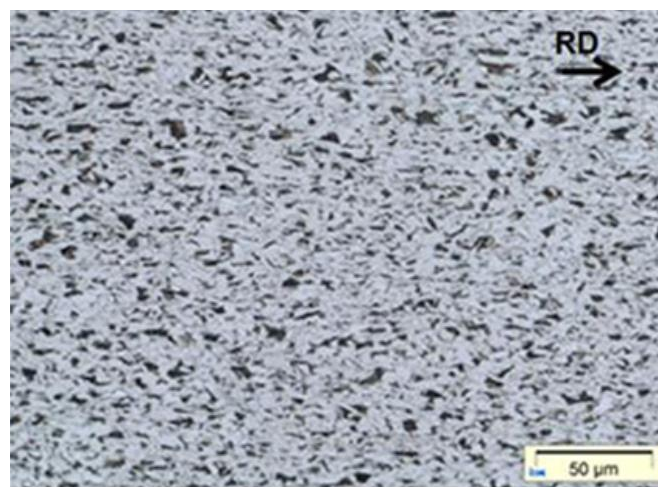


Figure 3.2: LOM microstructure of cold-rolled DP600 steel and its rolling direction [30].

### 3.1.2 Image analysis process

With the micrographs of experimental observation, some 2D RVE models with a size of  $25 \times 25 \mu\text{m}$  can be selected. Figs. 3.3 and 3.4 show the selection of 2D RVE based on real microstructure of DP590 and DP600 steels, respectively. And, in these two RVEs, the volume fraction of martensite is approximately equal to the available volume fraction of martensite from experimental data. It means that the dimensions can be acceptable for finite element modelling.

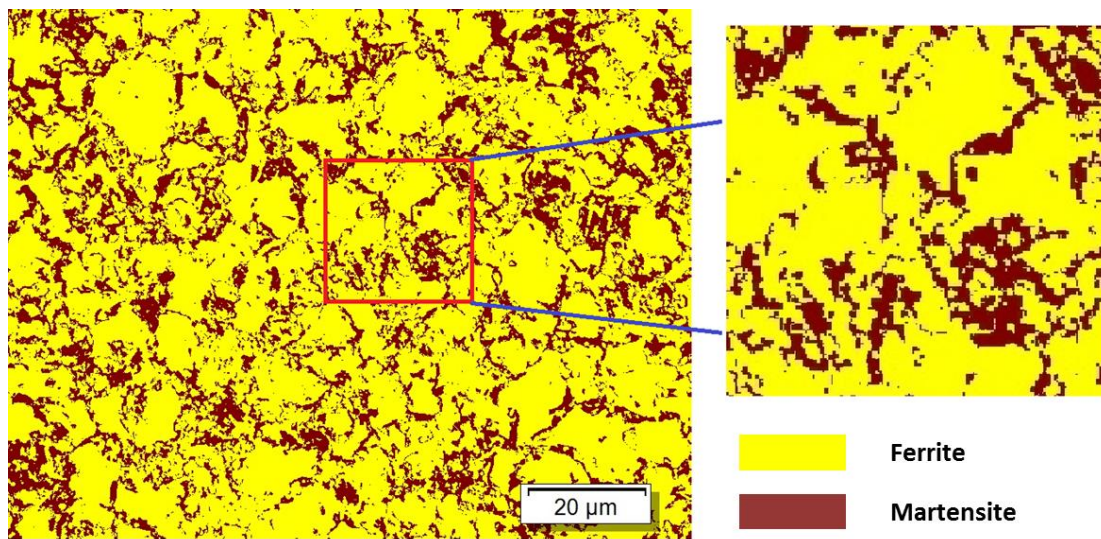


Figure 3.3: Selection of 2D RVE for micromechanical modelling of DP590 steel.

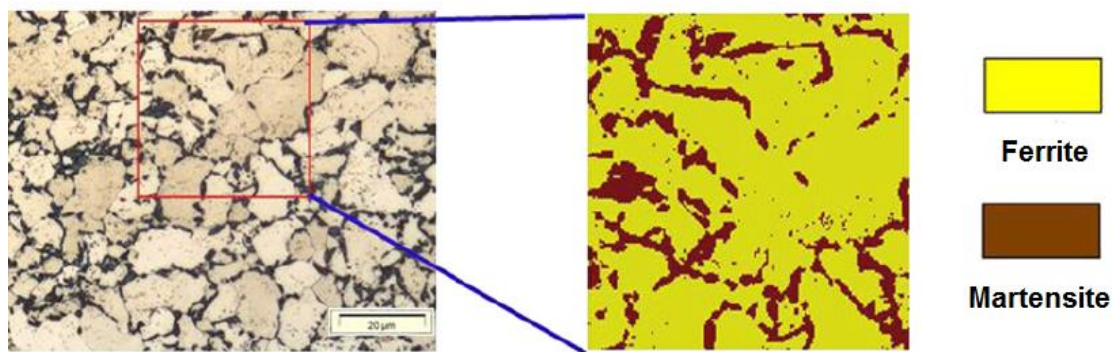


Figure 3.4: Selection of 2D RVE for micromechanical modelling of DP600 steel [30].

When the selection process of RVEs based on real microstructures of DP steels was done, an in-house image analysis program has been used to distinguish the phase interface between ferrite and martensite and to build the final finite element model. The image analysis process includes three main steps:



- (i) convert the selected metallographic image (Fig. 3.5a) into grayscale image by using Matlab [80] Toolbox, which is shown in Fig. 3.5b;
- (ii) extract geometry information of every martensite island by defining a threshold to distinguish the grain boundaries shown in Fig. 3.5c;
- (iii) mesh the RVE model and determine the material property of every element. Fig. 3.5d illustrates the final finite element model of RVE.

From the study of Ramazani *et al.* [21], the convergent element length is about 0.25  $\mu\text{m}$ . Therefore, in the 2D case, linear element with 0.25  $\mu\text{m}$  element size and RVE with 25  $\mu\text{m}$  edge length are used. Also, in this study, plan strain assumption is used in the micromechanical simulation.

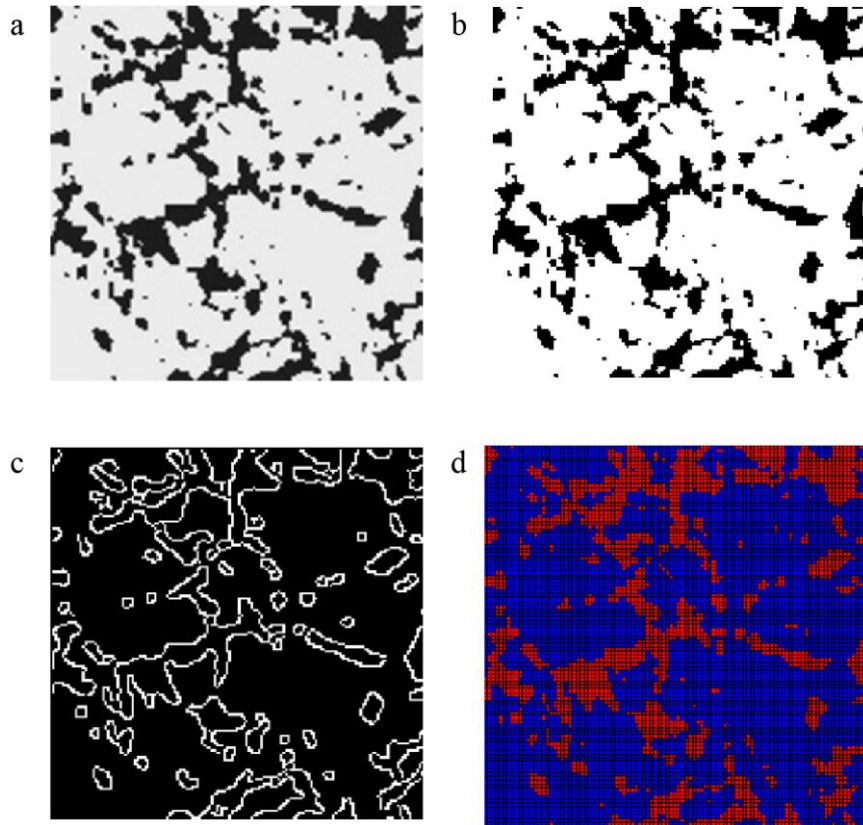


Figure 3.5: Image analysis procedure for RVE generation: (a) original metallographic image (black color: martensite phase; gray color: ferrite phase), (b) grayscale image, (c) grain boundaries and (d) final finite element model.

### 3.2. Calculation of flow curve of each single phase

In the paragraph 2.3, different methods to predict the flow stress of each single phase in the DP steel have been presented. It can be concluded that, the use of the dislocation based theory which links to both the micro and the macro scales, are expected to give more accurate prediction. Therefore, the flow stress of ferrite and martensite phase in the investigated steels is calculated from this dislocation based model. Since the only requirement of this model is the local chemical composition, section 3.2.1 will describe the experimental measurement and section 3.2.2 is about the calculation process.

#### 3.2.1 Chemical composition measurement

Due to the requirement of local chemical composition to compute the flow stress of the DP steel, we have done the energy dispersive X-ray spectroscopy analysis (EDX) for the DP590 and the DP600 steels. The model of the EDX analysis machine is FEI-Quanta FEG250, as shown in Fig. 3.6. The obtained chemical compositions are listed in Table 3.1.

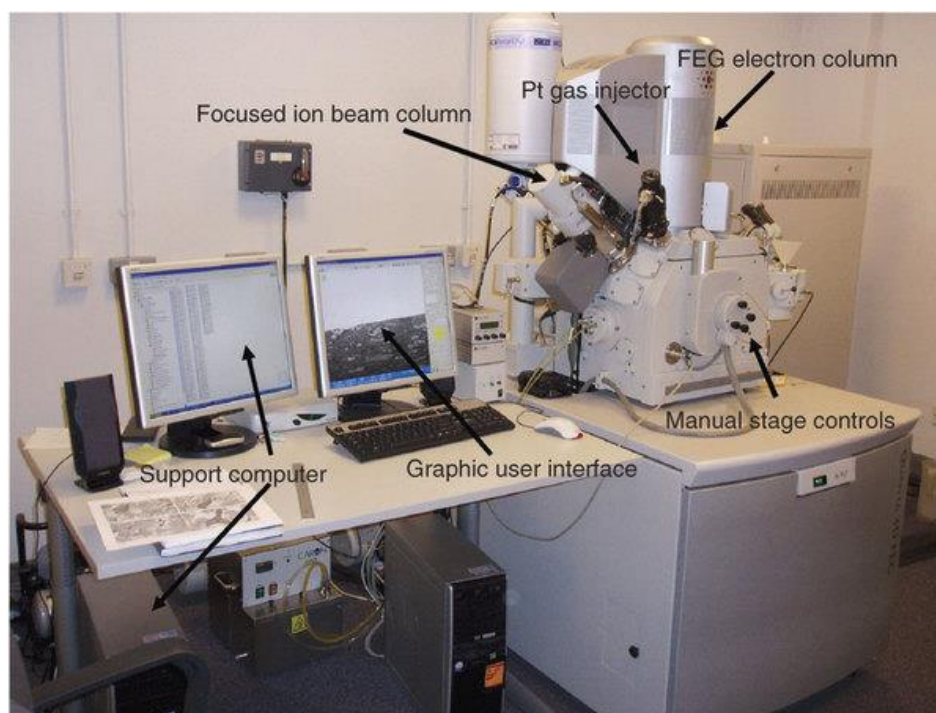


Figure 3.6: EDX analysis machine in UTC: FEI-Quanta FEG250.

Steel	C	Si	Mn	Ni	P	Cu	Cr	Mo
DP590	0.05	0.44	1.04	0.48	0.005	0.18	0.04	0.05
DP600	0.072	0.25	1.58	0.024	0.015	0.01	0.055	0.09

Table 3.1: Chemical composition of the DP590 and DP600 steels (in wt%).

### 3.2.2 Single phase flow stress

The flow stress of ferrite and martensite in the DP590 steel are calculated from the dislocation based theory presented in section 2.3.2, developed by Gutierrez [67]. In this method, material parameters are computed according to the local chemical composition, which can be expressed as in Eq. (2.9). In this expression,  $\alpha$  is a material constant ( $\alpha = 0.33$ ),  $M$  is the Taylor factor ( $M = 3$ ),  $\mu$  is the shear modulus ( $\mu = 80 \text{ GPa}$ ),  $b$  is the Burger's vector,  $L$  is the average dislocation free path (for ferrite  $L = 5.0 \times 10^{-6}$  and for martensite  $L = 3.8 \times 10^{-8}$ ),  $k_r$  is the dislocation recovery rate ( $k_r = 2$  and  $41$  for ferrite and martensite [68,69], respectively). The first term in Eq. (2.9) is the Peierls stress for dislocation movement. It can be calculated with Eq. (3.1). In this expression,  $N_{ss}$  denotes the carbon content (in wt. %) in dual-phase steel:

$$\sigma_0 = 77 + 750\%P + 60\%Si + 80\%Cu + 45\%Ni + 60\%Cr + 80\%Mn + 11\%Mo + 5000N_{ss} \quad (3.1)$$

The second term is the additional strengthening due to the precipitation and carbon in solid solution. In the case of ferrite, it can be given as:

$$\Delta\sigma = 5000(C_{ss}^F) \quad (3.2)$$

While for martensite, it should be:

$$\Delta\sigma = 3065(C_{ss}^M) - 161 \quad (3.3)$$

where  $C_{ss}^F$  and  $C_{ss}^M$  denote the carbon content (in wt.%) in ferrite and martensite, respectively.



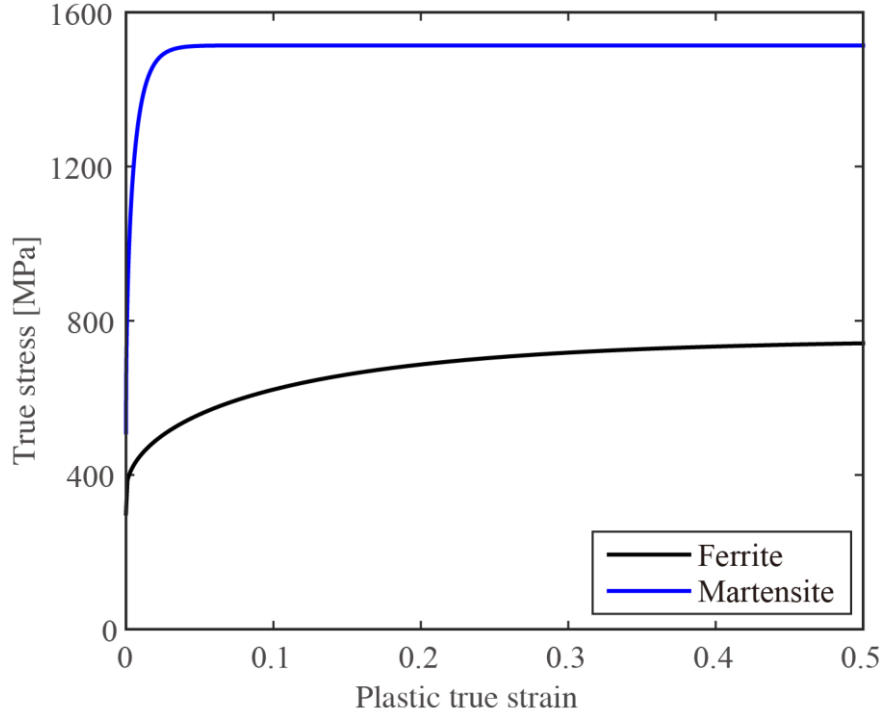


Figure 3.7: Flow curves of ferrite and martensite for DP590 steel.

For example, the flow stress of martensite and ferrite for the DP590 steel are shown in Fig. 3.7. They are computed based on the chemical composition listed in Table 3.1. Additionally, in the simulation isotropic hardening and von Mises yielding function are adopted for each phase.

### 3.3. Prescription of PBC

Since periodic boundary conditions have been defined in section 2.4.2, their implementation will be presented in this section. In order to apply PBC by using constraint equations according to Eq. (2.13), a concept of “dummy node” [71,81] should be introduced with degrees of freedom corresponding to the average strains FE codes. The nodal degrees of freedom, which belong to the boundaries of RVE, are then coupled to the degrees of freedom of the dummy nodes. Therefore, a set of constraint equations for the finite element model should be defined as:

$$N_1 u_i^A + N_2 u_j^B + \dots = \tilde{u} \quad (3.4)$$

where  $\tilde{u}$  is a prescribed value, such as displacement or strain, related to a dummy node. This dummy node is not attached to any part in RVE model. It is just a node with arbitrary coordinates. The dummy node is used to prescribe the displacement  $\tilde{u}$  at a certain direction. Users have to define a load step in order to apply this value

as a boundary condition. By doing so, the average stresses may then simply be extracted from the information about reaction forces at the dummy nodes. With this operation, it is hence not necessary to perform explicit integration over the RVE for determination of average strains and stresses.

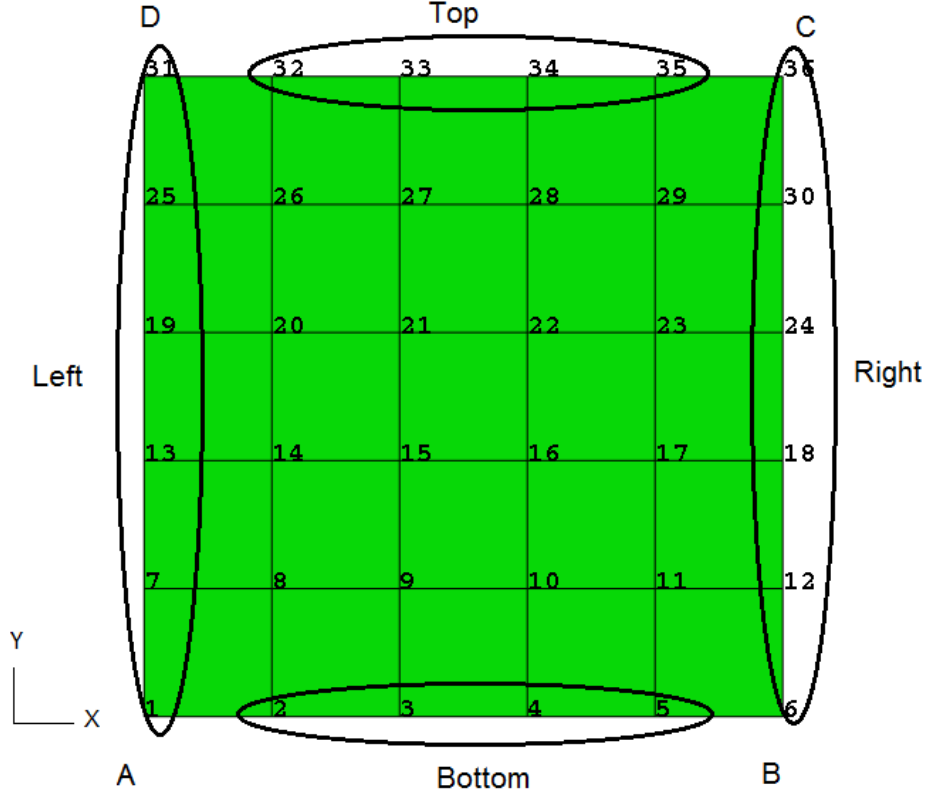


Figure 3.8: An example RVE discretized into  $5 \times 5$  elements.

For example, a base RVE (ABCD, dimension:  $1 \times 1$  mm) shown in Fig. 3.8 is discretized into  $5 \times 5$  elements for the sake of illustration. In this example, quadrilateral element with size of 0.2 mm and edge length 1 mm are used for 2D RVE. AB/DC is a pair of opposite parallel horizontal boundary edges of this RVE, and AD/BC is a pair of vertical boundary edges. In this case, Eq. (2.13) can be applied with  $\bar{\varepsilon}_{11} = 0.1$  and  $\bar{\varepsilon}_{22} = \bar{\varepsilon}_{12} = 0$  in the plane stress FE analysis. By this way, Eq. (2.13) can be rewritten as:

$$u_1^{AD} - u_1^{BC} = 0.1, \quad u_2^{AD} - u_2^{BC} = 0 \quad (3.5)$$

$$u_1^{DC} - u_1^{AB} = 0, \quad u_2^{DC} - u_2^{AB} = 0 \quad (3.6)$$

Here, boundary edge AD includes a set of nodes: 1, 7, 13, 19, 25, 31; BC is the node set which has nodes: 6, 12, 18, 24, 30; AB is the node set which has nodes: 2, 3, 4, 5

(nodes 1 and 6 are not included in this set since they will lead to excessive constraints of degrees of freedom); DC is the node set which has nodes: 32, 33, 34, 35. To apply the Eq. (3.5) in FE code, two constraint equations can be expressed as:

$$u_1^{AD} - u_1^{BC} + u_1^Y = 0, \quad u_2^{AD} - u_2^{BC} + u_2^Y = 0 \quad (3.7)$$

where  $u_1^Y = -0.1$  means to constrain degree of freedom 1 at node Y (a dummy node, 1000 for this example, it is necessary to make sure that the dummy node number should be big enough not to conflict with any other node numbers in FE model) to 0.1, and  $u_2^Y = 0$  to constrain degree of freedom 2 at node Y to zero.

### 3.4. Homogenization process

Following the asymptotic homogenization, the macroscopic displacement field of the DP steel depending on the aspect ratio  $\kappa$  between the macro and micro scales is expanded as:

$$u^\kappa = u_0(x, y) + \kappa u_1(x, y) + \kappa^2 u_2(x, y) + \dots, \quad y = \frac{x}{\kappa} \quad (3.8)$$

where the involved functions are dependent on the global macroscopic variable  $x$  and the local microscopic variable  $y$ . The dependence on  $y = x / \kappa$  implies that a quantity varies within a very small neighborhood of a macroscopic point  $x$ , which can be considered as “stretching” the microscale, so it becomes comparable to the macroscale. When  $\kappa \ll 1$ , the dependence on  $y$  can be viewed periodic for a fixed macroscopic point  $x$ . As mentioned in section 2.5.2, the use of this approach requires PBC to assure the perfect tiling between adjacent RVEs. Then, the above-mentioned PBCs can make the use of the translator symmetries of geometry to handle any physically valid deformation state of RVEs. Based on the AEH approach, the homogenized stress and strain are given by:

$$\bar{\sigma}_{ij} = \frac{1}{V_{\text{RVE}}} \int_{V_{\text{RVE}}} \sigma_{ij} dV \quad (3.9)$$

$$\bar{\varepsilon}_{ij} = \frac{1}{V_{\text{RVE}}} \int_{V_{\text{RVE}}} \varepsilon_{ij} dV \quad (3.10)$$

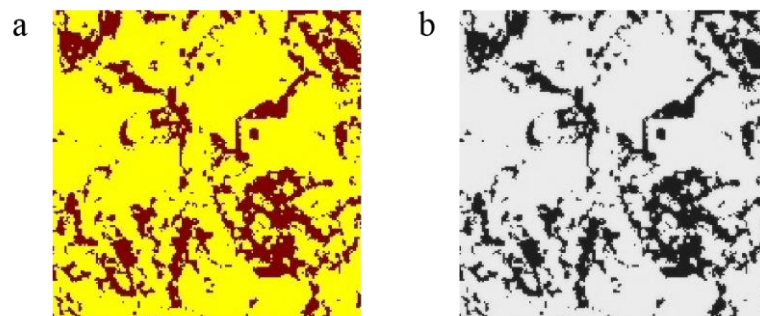
These two equations are computational first-order homogenization by volume averaging. In the general FE codes, this homogenization process can be implemented easily and directly.

### **3.5. Validation on tensile test analysis**

Numerical tensile tests can be carried out on the 2D RVEs generated from the microstructures of DP590 (from ESI-Group) and DP600 steel (from literature [30]). The evolution of stress-strain relation in the RVEs can be obtained from these numerical tensile tests. With the PBC prescription and the homogenization scheme presented in last sections, the homogenized flow stress can be obtained to compare with the experimental results. Therefore, the micromechanical modelling process will be described in the following sections. Also, results and comparisons will be discussed in the final section.

#### ***3.5.1 Micromechanical modelling of DP 590 steel***

As presented in previous sections, the first operation to build the micromechanical models of the DP590 steel is to select the proper RVE with acceptable size. As shown in Fig. 3.3, a 2D RVE has been selected to construct a finite element model of the DP590 steel with real microstructure using metallographic image. Through the image analysis process (as shown in Fig. 3.9), a finite element model (in Fig. 3.9d) can finally be constructed.



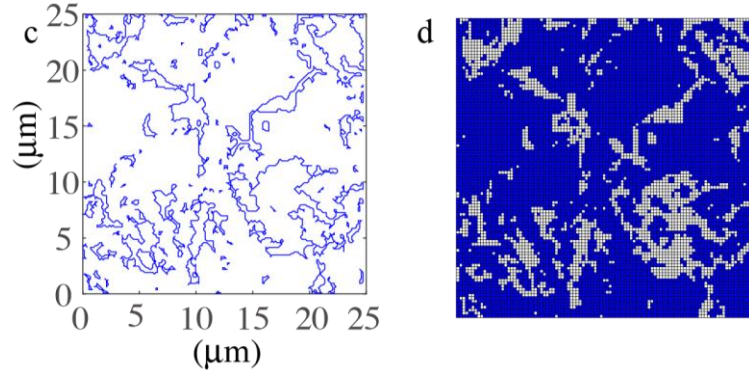


Figure 3.9: Image analysis procedure for RVE generation: (a) original metallographic image (brown color: martensite phase; yellow color: ferrite phase), (b) grayscale image, (c) grain boundaries and (d) final finite element model.

Also, with the chemical compositions in Table 3.1, the flow curves of martensite and ferrite are shown in Fig. 3.7. Then, numerical tensile tests have been performed on this generated 2D RVEs based on real microstructure and prescribed PBC. The predicted stress-strain behavior of DP590 steel using the homogenization scheme in section 3.4 is compared with the experimental result in Fig. 3.10.

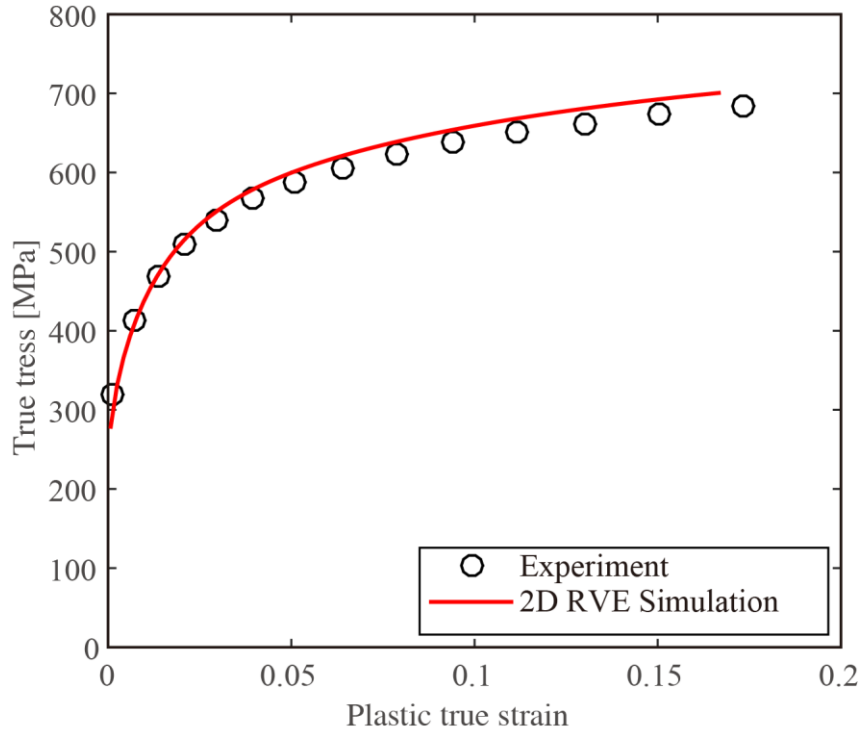


Figure 3.10: Measured and predicted flow curve of DP590 steel.

From this figure, it can be observed that there are small dissimilarities the measurements and the predictions from micromechanical modelling. The main

reason that can explain this difference is that, no fracture model and material softening mechanism have been assigned to both of ferrite and martensite phases. In addition, plan strain assumption is adopted for the simulation, while in the real tensile test, the specimen is subjected to three dimensional stress state. Therefore, this phenomenon appears, and we can expect that it will increase with the volume fraction of martensite.

Fig. 3.11 shows the calculated equivalent plastic strain distribution in 2D RVE at various global strain levels of: (a) 0.24%, (b) 2.41%, (c) 8.02%, and (d) 16.54%. In both of the contour plots, shear bands can be observed in the ferrite matrix near martensite islands.

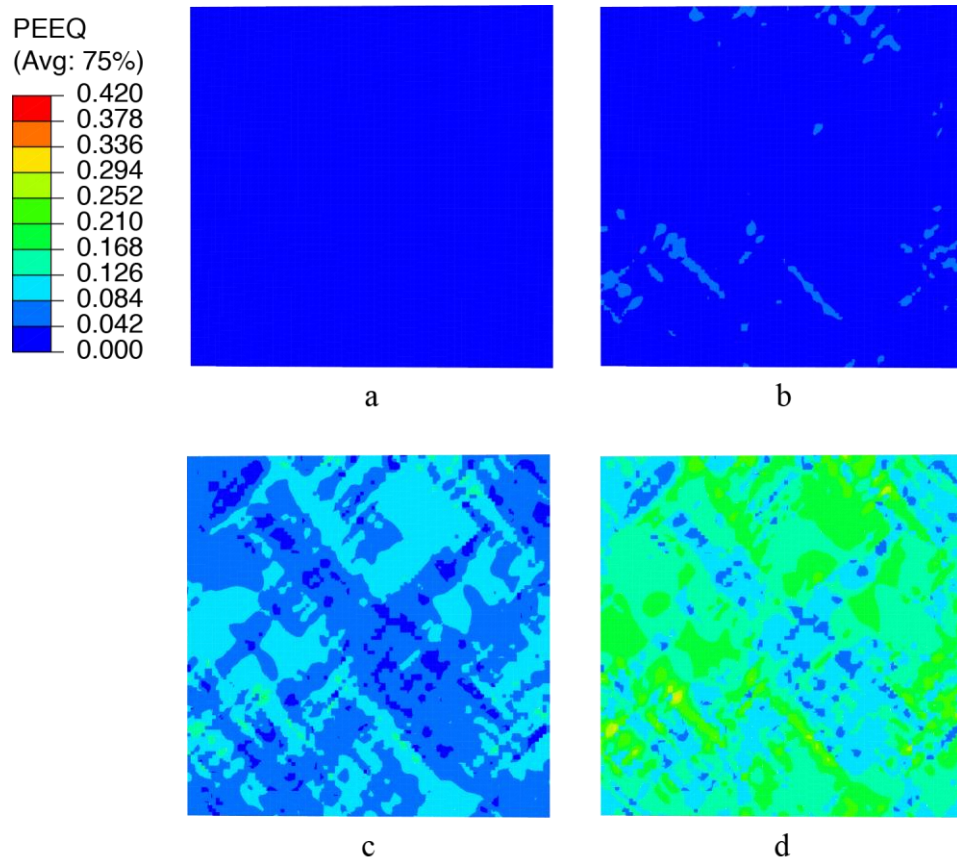


Figure 3.11: Equivalent plastic strain distribution in 2D RVE at various global strain levels of: (a) 0.24%, (b) 2.41%, (c) 8.02%, and (d) 16.54%.

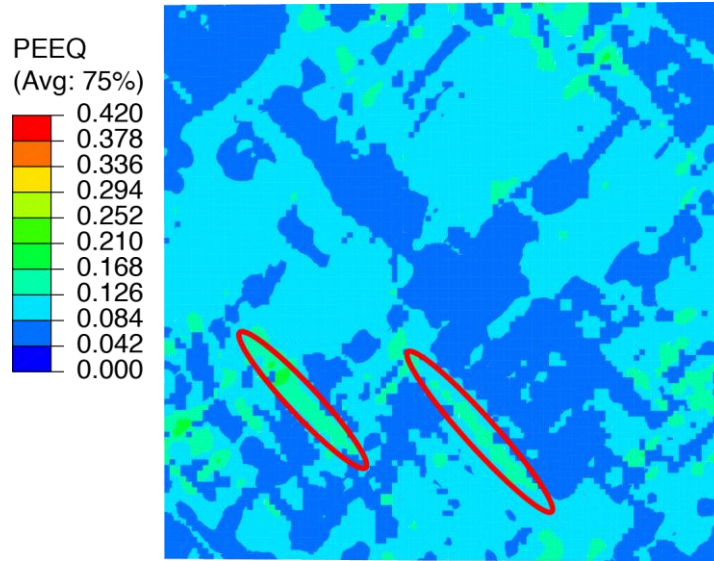


Figure 3.12: Equivalent plastic strain distribution in 2D RVE at global strain of 10%, shear bands in the red ellipses.

The shear bands of the localized plastic strain are due to the microstructure inhomogeneity of dual-phase steel. The details of shear bands are shown in Fig. 3.12. And the direction of the localized plastic deformation is on average  $45^\circ$  to the tensile direction. As the plastic flow accumulating, material failure can be predicted as the result of plastic strain localization in RVE during the deformation process. At the same time, shear dominant failure mode continues and leads to final failure of the 2D RVE model.

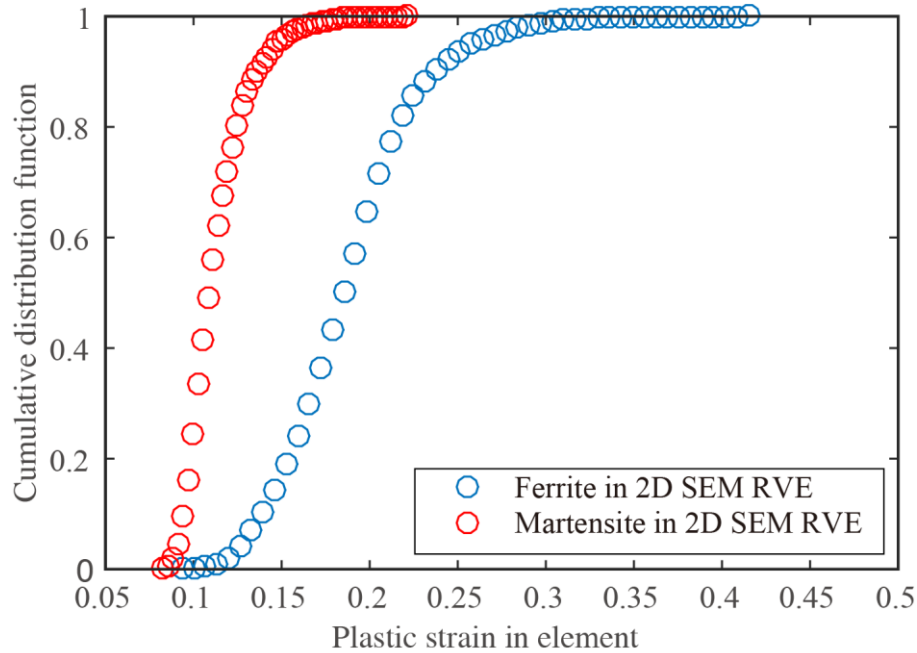


Figure 3.13: Cumulative distribution function of plastic strain in martensite and ferrite phases of 2D RVE at global strain of 15%.



The cumulative distribution of plastic equivalent strain in martensite and ferrite resulting from the 2D RVE simulation at global strain of 15% is illustrated in Fig. 3.13. In future work, the result can be considered as the standard to evaluate and to validate 2D RVEs generated from artificial microstructures.

Actually, SEM microstructure of deformed dual-phase has been reported by Hosseini-Toudeshky *et al.* [20], the ferrite matrix near the martensite islands is deformed severely and shear localization caused the void initiation along the grains interface. As the volume fraction of void reaches a critical value, micro-cracks initiated due to interface debonding that occurs and propagates. Their experimental observation validates our simulation results. Therefore, the computed flow stress can be used in the macroscopic simulation with fracture models.

### 3.5.2 Micromechanical modelling of DP 600 steel

By the same way, 2D RVE of the DP600 steel from literature [30] can be built as shown in Fig. 3.14. And, the flow curves, shown in Figs. 3.15 and 3.16, of martensite and ferrite phases are calculated with the chemical compositions listed in Table 3.1.

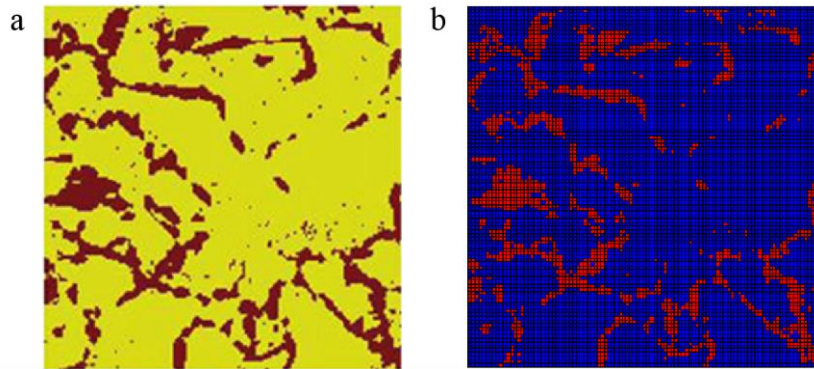


Figure 3.14: 2D RVE based on real microstructure of DP600 steel: (a) original metallographic image (brown color: martensite; yellow color: ferrite) [30], (b) final finite element model.



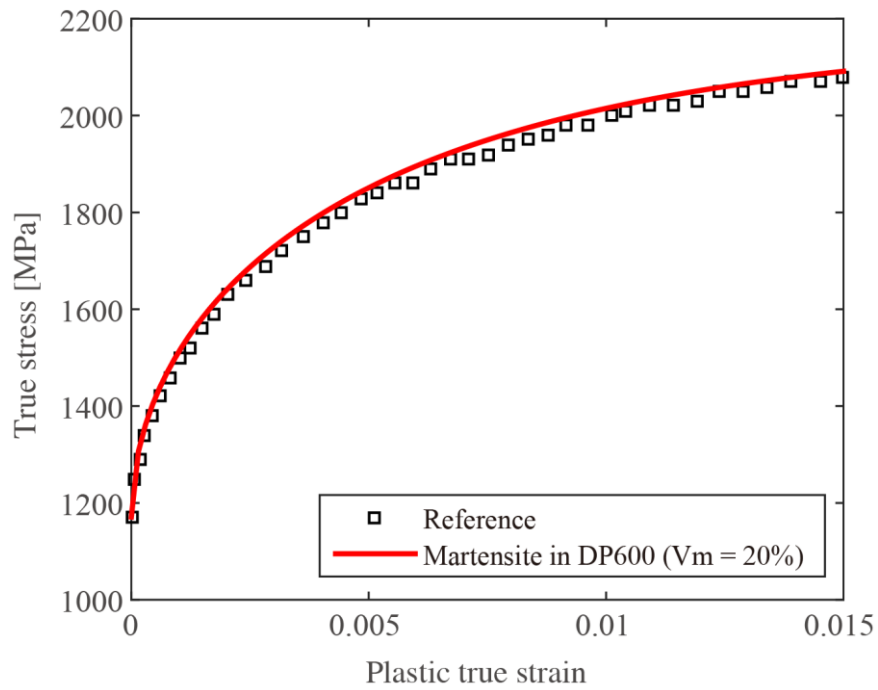


Figure 3.15: Predicted and reference flow curves of martensite phase for DP600 steel with 20% of martensite [30].

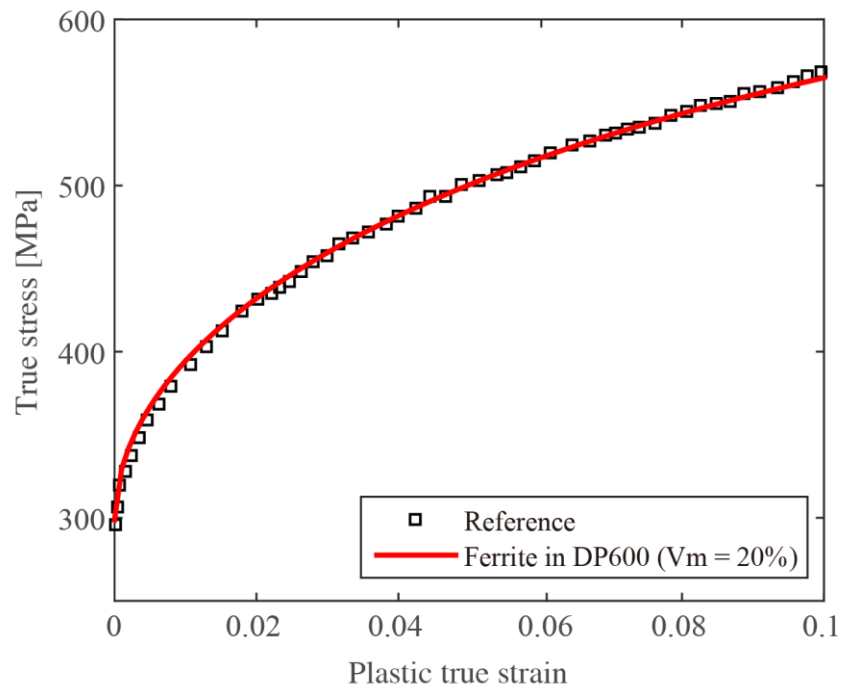


Figure 3.16: Predicted and reference flow curves of ferrite phase for DP600 steel with 20% of martensite [30].

Figs. 3.15 and 3.16 show the predicted and reference flow curves of martensite and ferrite phase for the DP600 steel with 20% of martensite. For the DP600 steel, the difference between the flow curves of ferritic phase and the reference one is almost zero. However, for martensitic phase, slight discrepancy is observed between our predictions and the reference result.

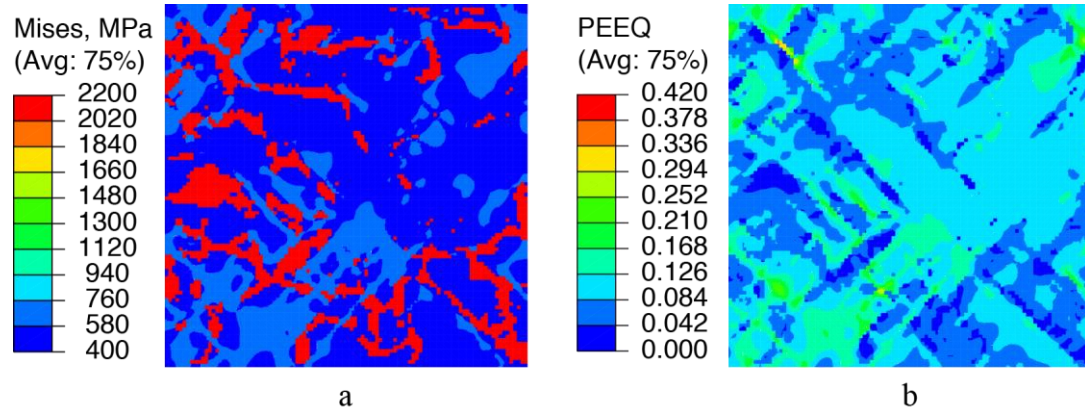


Figure 3.17: Von Mises stress and equivalent plastic strain distribution in 2D RVE at global strain of 10%.

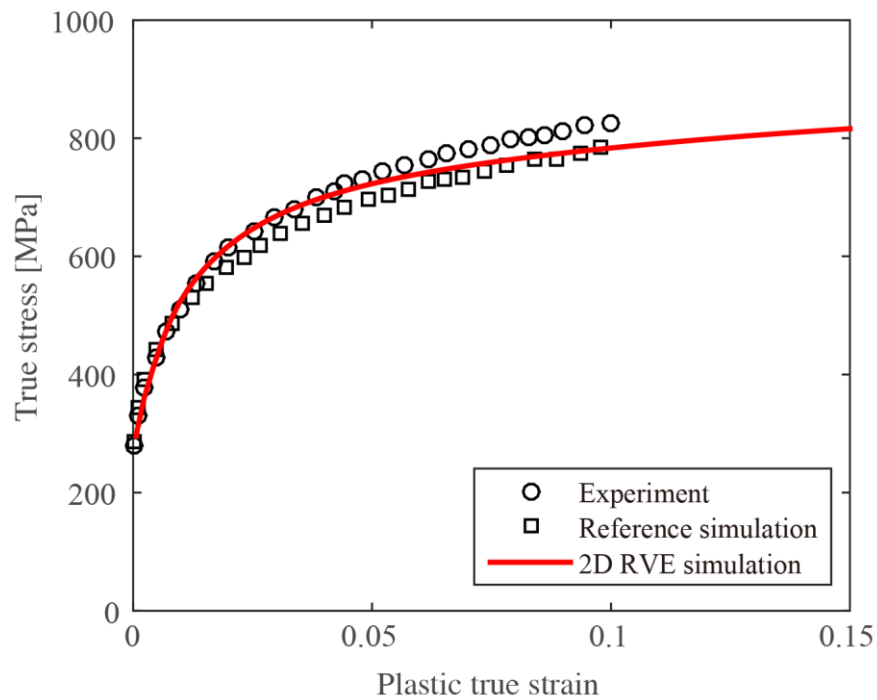


Figure 3.18: Reference data, measured and predicted flow curves of DP600 steel with 20% martensite.

The evolution of stress and strain in the RVEs can be obtained from these numerical tensile tests. Fig. 3.17 shows the contour plot of von Mises stress and the equivalent plastic strain on microscale at global strain equaled to 10% for the DP600 steel. In both of the contour plots, shear bands can also be noticed in 2D RVE. And the direction of the localized plastic deformation is on average  $45^{\circ}$  to the tensile direction. High stresses up to 2100 MPa can be noticed in the martensite islands.

A comparison between the data from reference and the predicted flow curves of the investigated DP600 steel is shown in Fig. 3.18. The results of finite element simulations using 2D approach have been compared with reference data, it can be found that there are small dissimilarities. The main reason is that, the flow curves of each phase are obtained by using inverse analyses, so the used material properties are almost the same with the reference data. Additionally, our results are compared with experimental results, it can be noticed that, as the volume fraction of martensite increases, the effect of dimensionality will become more significant. However, from the literature [30], it is stated that, the flow curves of 3D simulation are much closer to those of the experimental flow curves compared to those of the 2D simulation in all investigated DP microstructures. The most plausible reason of this phenomenon is that, in the 2D simulation, planar strain state is adopting during the calculation, but in the real tensile test, the specimen deforms three dimensionally. So the difference appears, and it increases with the volume fraction of martensite.

### **3.6. Conclusions**

Advanced high strength steels, such as the DP steels, exhibit complex ductile fracture behavior. In this study, the flow stress of the DP590 and DP600 steels is predicted by using 2D RVE models generated from real microstructures. From comparisons with experimental results, only pretty small dissimilarities are observed. And, these dissimilarities may result from several reasons as discussed above. Therefore, it can be concluded that micromechanical modelling can predict the flow stress of DP steels.

Due to the microstructure inhomogeneity of DP steels, material failure can be predicted as the result of plastic strain localization in RVE during the deformation process. Shear bands can be observed on average  $45^{\circ}$  to the tensile direction. Therefore, as the plastic flow accumulating, shear dominant failure mode continues and leads to final failure of the 2D RVE model. This phenomenon has been verified

by the observation of Hosseini-Toudeshky *et al.* [20]. So, further RVE models with fracture models can be developed in future work.

However, it is relatively difficult to get the real microstructure of DP steel. During the acquisition of the real microstructure, it is necessary to cut specimens, to polish samples, to take micrographs. This whole procedure may take one week to generate a proper RVE model. Therefore, there is a necessity to generate artificial 2D or 3D microstructures using automated procedures for grain generation and coloring algorithms for phase assignment to replace RVEs based on real microstructure. Moreover, a good RVE should be constructed based on such a way that the shape, morphology, size and randomness of constituent phases involved are representative of the microstructure under consideration. Therefore, micromechanical volume elements, which are generated from artificial microstructures with different parameters, are considered in next chapter.

## Chapter 4

### Micromechanical model based on artificial microstructure

In this chapter, an artificial microstructure generator with an enhanced novel phase assignment algorithm based on material topology optimization is proposed to investigate the mechanical properties of DP steel. With this algorithm, phase assignment process is performed on a modified Voronoï tessellation to achieve the targeted representative volume element (RVE) with a good convergence. This method also includes a proper orthogonal decomposition (POD) reduction of flow curves (snapshots) to identify the optimal controlling parameters for DP steel. This numerical method significantly improves the representation of the generated RVE with low computational cost. The proposed method is verified using a DP590 steel which indicates a good agreement with experimental material behavior and the prediction from RVE based on real microstructure. Predictions of plastic strain patterns including shear bands using the artificial microstructure closely resemble the actual material behavior under similar loading conditions. Robustness of this approach provides a new dimension for RVE development based on artificial microstructure which can effectively be implemented in material characterization.

#### 4.1. Artificial microstructure generator

##### 4.1.1 Modified Voronoï tessellation

Voronoï tessellation allows the generation of artificial microstructures with randomly distributed and orientated grains for metallic or ceramic materials. This kind of tessellation is a nearest neighbor diagram determined from a set of generating seeds. Since the resulting diagram is mainly affected by the choice of Voronoï generating seeds, a modified point set has been used to overcome the shortcomings (e.g., the inexact estimation of grain size and nearest neighboring grain number) exhibited by in the standard tessellation generated from a pseudo-random sequence [40,42,43]. The modified point set is generated using Halton (quasi-random) sequence [46], which statistically exhibits low discrepancy.

Halton sequence is constructed using a deterministic method that uses coprime numbers as its bases. An integer  $n$  in decimal notation can be written in base  $\nu$  as:

$$n = \sum_{i=1}^m w_i \nu^i \quad (4.1)$$

where  $w$  denotes the coordinate of each basis. Therefore, the  $n$ -th number in Halton sequence of base  $\nu$  can be given by:

$$h(n, \nu) = \sum_{i=1}^m w_i \nu^{-(i+1)} \quad (4.2)$$

Throughout the construction of Halton sequence, the distribution of the sampling points which are considered as the Voronoï seeds, is more uniform than that of pseudorandom sequence.

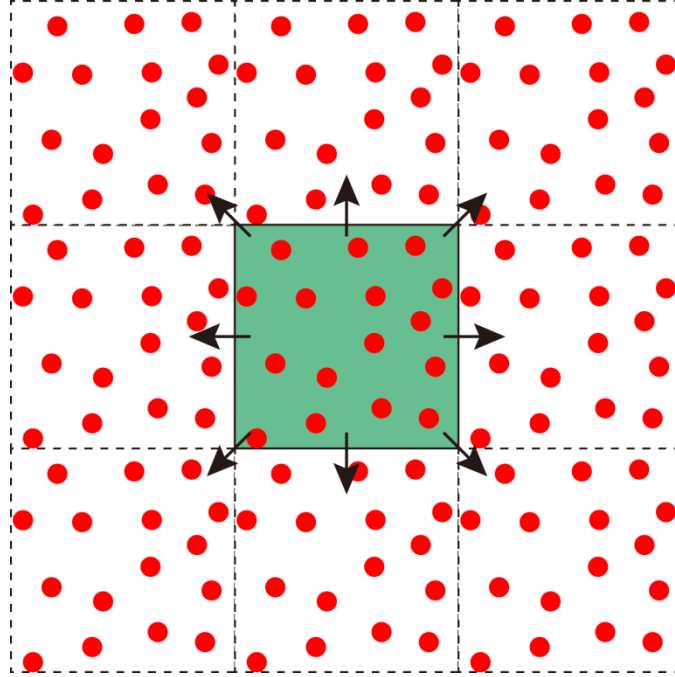


Figure 4.1: Construction of a periodic set of Voronoï generating seeds.

Since periodic microstructures have favorable numerical properties in the context of computational homogenization [45], these seeds are repeated three times in each direction to ensure the periodicity of the modified Voronoï tessellation, as shown in Fig. 4.1. In order to demonstrate the advantages of the modified Voronoï tessellation, an example has been compared with the standard one, as shown in Fig 4.2. Two sets of seeds are generated from Halton (quasi-random) and pseudo-random sequences, respectively. The pairwise distance of each seed set follows the same normal

distribution, in which the average value and standard deviation are  $0.52 \mu\text{m}$  and  $0.25$ . According to the generation mechanism of Voronoï tessellation, the distribution of pairwise distance can directly represent the size of resulting cells. For example, if the average distance between a seed and its surrounding neighbors is longer, the size of the corresponding Voronoï cell will be larger. Therefore, these two parameters that are the average value and the standard deviation of the pairwise distance distribution, can be utilized to control the size distribution of the generated Voronoï cells.

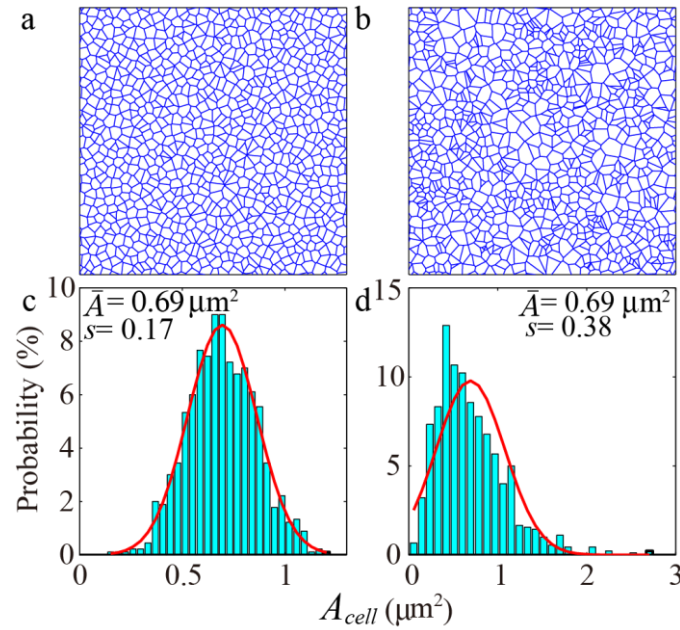


Figure 4.2: Square periodic Voronoï tessellations including 900 cells generated for: (a) modified one using Halton (quasi-random) sequence and (b) standard one using pseudo-random sequence. Distribution of cell area in each case: (c) modified and (d) standard tessellations.

In general, RVE size has a significant influence on the simulation results. The size of a remarkable RVE has to be sufficiently large to represent all microstructural features while that should also remain small enough to be treated as statistically homogeneous during the calculation of effective properties. In the studies of Ramazani *et al.* [21,30], it has been concluded that the acceptable size of RVE for DP steel can be considered as minimum of  $24 \mu\text{m}$  while it contains at least 19 martensite islands, since periodic boundary conditions was imposed. Likewise, we consider 2D RVE models with a size of  $25 \mu\text{m} \times 25 \mu\text{m}$ . Fig. 4.2a and b show the modified and standard Voronoï tessellations including 900 cells generated based on

these two seed sets. Fig. 4.2c and d also illustrate the area distribution of Voronoï cells for the modified and standard tessellations, respectively.

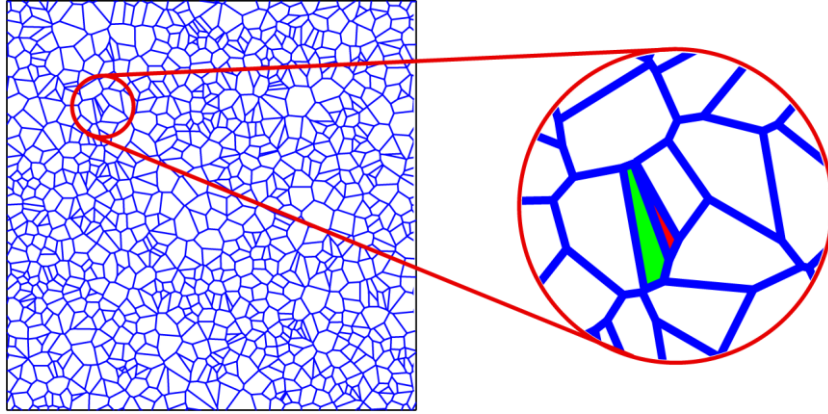


Figure 4.3: Voronoï cells with bad aspect ratio (green) and extremely small cell (red) in the standard Voronoï tessellation.

From this comparison, both of the two generated Voronoï tessellations have the average cell area of  $\bar{A}_{cell} = 0.69 \mu\text{m}^2$ . However, the modified tessellation shows a standard deviation of 0.17 which is less than half of the standard one (0.38). It clearly indicates that the modified Voronoï cells generated from Halton sequence are more regular than the other. This can effectively avoid the appearance of bad aspect ratio and extremely small cells in the artificial microstructure, as shown in Fig. 4.3. Moreover, the modified Voronoï tessellation is generated directly from Halton sequence, no additional computational cost on iteration to control the grain size distribution and grain morphology. Further details are included in Section 4.3 to show other advantages of the modified Voronoï tessellation on prediction of flow stress of DP590 steel.

#### **4.1.2 Phase assignment algorithm based on topology optimization**

In the previous section, a modified Voronoï tessellation is generated to represent the polycrystalline aggregate in DP microstructure. With the modified Voronoï tessellation, an automated process needs to be developed to assign the appropriated phases (martensite and ferrite) to each cell. In order to perform the automated phase assignment process, two controlling parameters proposed by Fillafer *et al.* [43], are utilized in this study to confine the solution space. These two parameters, the martensite phase fraction  $P_M$  and the neighboring coefficient of martensite grains  $C_M$ ,



which consider not only the martensite phase fraction but also the dispersion of different martensite islands. The expressions of these two parameters are given as:

$$P_M = \frac{A_M}{A_T}, C_M = \frac{2L_{MM}}{2L_{MM} + L_{FM}} \quad (4.3)$$

where  $A_M$  and  $A_T$  denote martensite phase and total area, while  $L_{MM}$  and  $L_{FM}$  are length of specific martensite-martensite and ferrite-martensite grain boundaries, respectively. An illustrative example is given in Fig. 4.4, to show the computation of the neighboring coefficient. Fig. 4.4a shows several local Voronoï cells, in which the central cell is a martensite grain surrounded by 6 different cells. The length of the shared boundaries that can be classified as two sets:  $L_{MM}$  and  $L_{FM}$ , are listed in Fig. 4.4b. The corresponding  $C_M$  is computed as 0.27 using Eq. (4.3). Accordingly, it is identified that, the value of  $P_M$  can vary between 0 and 1. But, for a given martensite phase fraction,  $C_M$  cannot satisfy the whole range of  $[0, 1]$ . In other words, these two controlling parameters are not mutually independent.

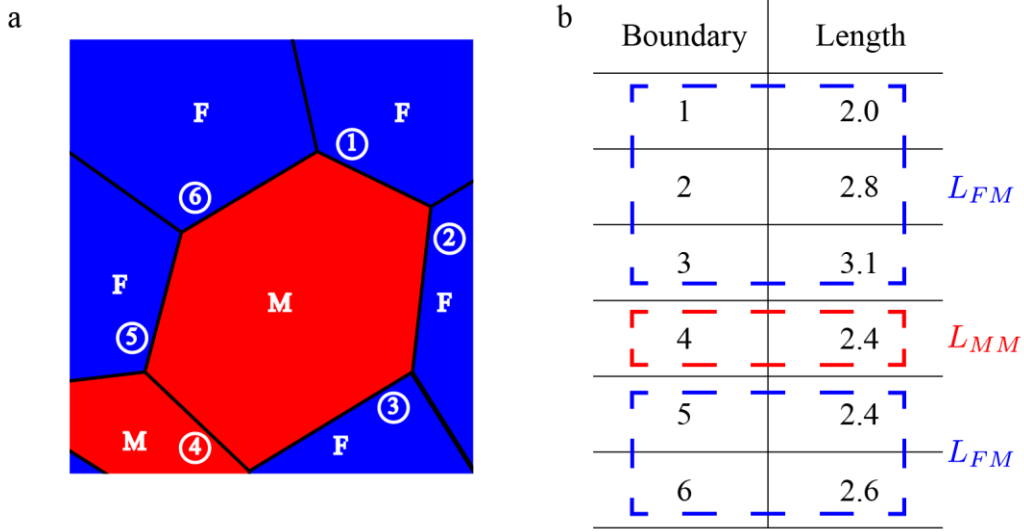


Figure 4.4: Illustrative example of the neighboring coefficient of martensite grains  $C_M$ : (a) local Voronoï cells (blue: ferrite cells, red: martensite cells) and (b) boundary length shared by the central martensite and surrounding cells.

Within the automated phase assignment process, the modified Voronoï tessellation can be considered as the fixed grid, which is similar in material topology optimization design. In each modified Voronoï cell, a material density function is proposed to determine its phase property: martensite grains with density  $\rho = 1$ , the red layer in Fig. 4.5, while ferrite ones with density  $\rho = 0$ , the blue layer in Fig. 4.5.

By defining constraints and an objective function, this process is deduced to a 0-1 discrete value optimization problem, also known as “black-and-white” design. Therefore, the material interpolation algorithms in topology optimization can be referred to achieve artificial microstructures with proper phase distribution, as shown in Fig. 4.5.

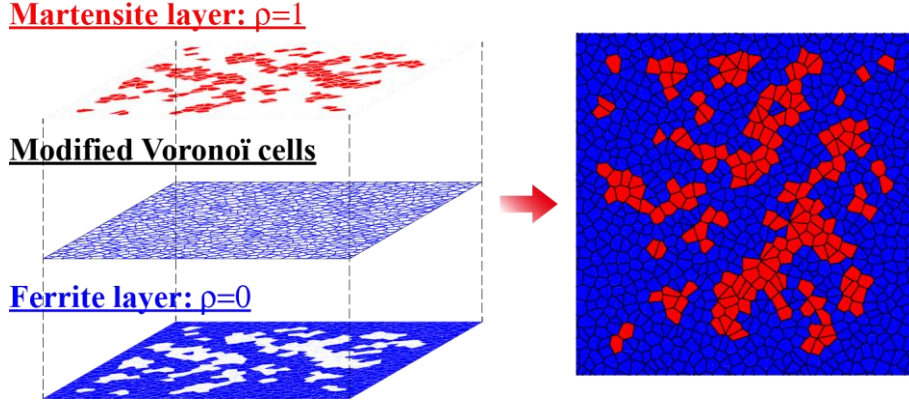


Figure 4.5: Artificial phase assignment process and final DP microstructure.

According to the algorithm related to density-based topology optimization method, the controlling parameters in Eq. (4.3), can be rewritten in matrix form:

$$P_M = \frac{\mathbf{a}^T \boldsymbol{\rho}}{\mathbf{a}^T \mathbf{I}}, \quad C_M = \frac{\boldsymbol{\rho}^T \mathbf{E} \boldsymbol{\rho}}{\mathbf{I}^T \mathbf{E} \boldsymbol{\rho}} \quad (4.4)$$

where  $\mathbf{a}$  is the grain area vector,  $\mathbf{I}$  is uniform vector,  $\mathbf{E}$  is a correlation matrix of martensite islands' neighboring coefficient. The components of the matrix  $\mathbf{E}$  are obtained by:

$$E_{mn} = \frac{L_{mn}}{\sum_{n=1}^N L_{mn}} \quad (4.5)$$

Here,  $L_{mn}$  is the boundary length shared by  $m$ -th and  $n$ -th cells,  $N$  is the total amount of neighbor cells. By introducing  $\mathbf{E}$ , the length of grain boundaries can be replaced by the material density vector, which only consists of 0 or 1:

$$\rho_e(\mathbf{x}) = \begin{cases} 0 & \text{if } \mathbf{x} \in \Omega \setminus \Omega_M \\ 1 & \text{if } \mathbf{x} \in \Omega_M \end{cases} \quad (4.6)$$

where  $\mathbf{x}$  is the geometry information of each cell. Noting from the definition of  $\boldsymbol{\rho}$ , a distributed and discrete value problem is formulated in a matrix form. To solve this

problem, the most commonly used approach in topology optimization is to replace the integer density (0 or 1) by continuous variables [0, 1]. And then, a penalty factor  $p$  is introduced to easily obtain a convergent martensite density distribution, as the so-called “black-and-white” solution [48,51,55]. Therefore, a power form of the material density in each cell, also named “pseudo-density”, can be rewritten as:

$$Q_e = Q_F + \rho_e^p (Q_M - Q_F) \quad (4.7)$$

where  $Q_F$  and  $Q_M$  are the material density of ferrite and martensite, respectively. Therefore, the structural optimization problem can be formulated as:

$$\begin{aligned} \text{Argmin } J &= \|C_M - C_M^{target}\| \\ \text{s.t. } : \quad &\int_{\Omega} Q_e(x) \cdot a_e d\Omega \leq P_M^{target} \cdot A_T \\ &Q_e \in [Q_F, Q_M] \end{aligned} \quad (4.8)$$

where the target controlling parameters  $P_M^{target}$  and  $C_M^{target}$  are predefined based on statistical descriptions of DP steel,  $a_e$  is the area of a Vorono cell. Here, a heuristic updating scheme is introduced to solve this optimization problem:

$$Q_e^{new}(\mathbf{x}) = \begin{cases} \max(0, Q_e - \delta) & \text{if } Q_e B^{\zeta} \leq \max(0, Q_e - \delta) \\ \min(1, Q_e + \delta) & \text{if } Q_e B^{\zeta} \geq \min(1, Q_e + \delta) \\ Q_e B^{\zeta} & \text{otherwise} \end{cases} \quad (4.9)$$

where  $\delta$  is a positive moving limit and  $\zeta$  is a numerical damping coefficient to reach the convergent martensite phase distribution. And, the term  $B$  is calculated using the optimality condition [48,51,55]:

$$B = \frac{\frac{\partial J}{\partial Q_e}}{\lambda \frac{\partial P_M}{\partial Q_e}} \quad (4.10)$$

In Eq. (4.10), the Lagrangian multiplier  $\lambda$  is calculated using bisection algorithm to ensure the satisfaction of phase fraction constraint. The other two terms,  $\partial J / \partial Q_e$  and  $\partial P_M / \partial Q_e$  can be obtained in matrix form.

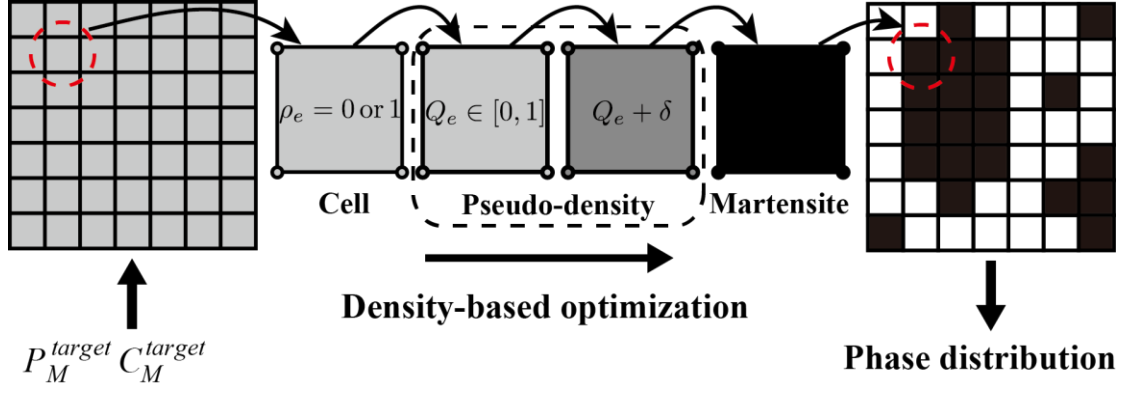


Figure 4.6: Illustration of the phase assignment algorithm based on topology optimization.

A schematic illustration of this phase assignment algorithm is shown in Fig. 4.6. In summary, the algorithm consists of the following steps:

- (i) the initial material density of each Vorono ĩcell is given with the value of the targeted martensite phase fraction  $P_M^{target}$ , the initial grayscale grids in Fig. 4.6 (left);
- (ii) the discrete material density is deduced to the continuous “pseudo-density”, after the integration of the penalization factor in Eq. (4.7). Meanwhile, this discrete value problem also becomes a continuous one;
- (iii) iterations of the updating scheme in Eq. (4.9) are performed to achieve a convergent material density in each cell. The intermediate grayscale color in Fig. 4.6 (middle) shows the simultaneous material density after the first iteration;
- (iv) a convergent solution is reached to present the optimal phase distribution. It is shown as the final grids in Fig.4.6 (right), white and black fill colors indicate ferrite and martensite phases, respectively.

Following the aforementioned steps, artificial DP microstructures are constructed rapidly with a good convergence. That is, if the controlling parameters and Vorono ĩ tessellation are fixed, our generator will find only one unique optimal phase distribution.

### 4.1.3 Numerical examples

The basic methodology of the novel DP microstructure generator has been presented; this section provides several numerical examples and the applied values of other design parameters (e.g., penalty factor). With the modified Voronoï tessellation described in Section 4.1.1 and predefined sets of controlling parameters, two artificial microstructures are constructed using the proposed phase assignment algorithm, as shown in Fig 4.7.

Figure 4.7: Example artificial microstructures with 900 grains.

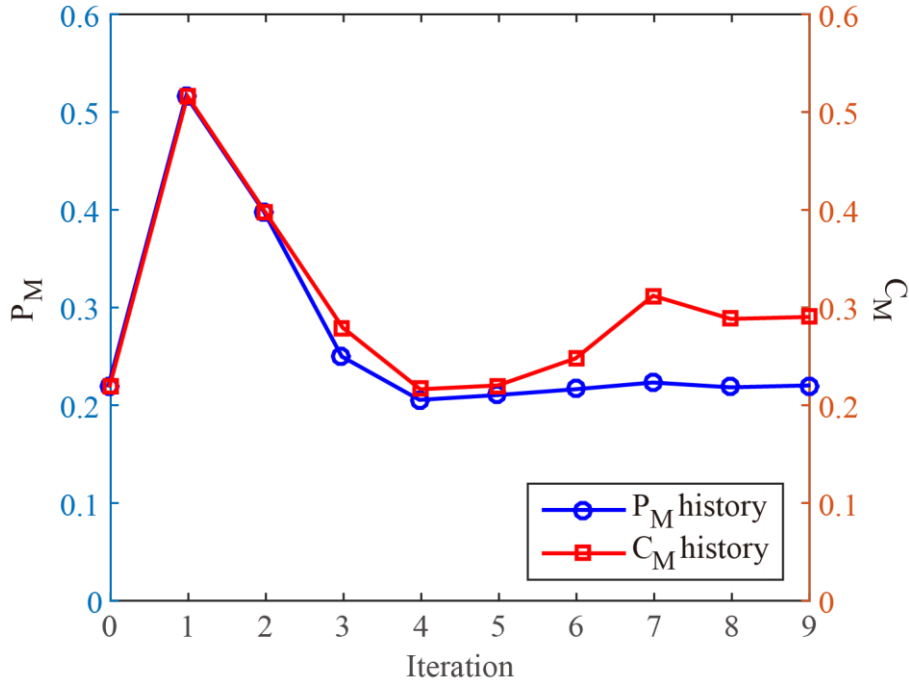


Figure 4.8: History curves of the controlling parameters for the artificial microstructure with  $P_M^{target} = 0.22$ ,  $C_M^{target} = 0.3$ .

In these two examples, the penalty factor  $p$  and the move limit  $\delta$  are fixed as 3 and 0.3, respectively. The first example, in which the target controlling parameters are set to  $P_M^{target} = 0.22$  and  $C_M^{target} = 0.3$ , is illustrated in Fig. 4.7a. A fast and stable convergence is achieved in 9 iterations, the resulting microstructure is obtained with  $P_M = 0.22$  and  $C_M = 0.29$ . As discussed previously, due to the interdependence of the two parameters, there exists a slight dissimilarity between the target and resulting

parameters. While, an exact microstructure is constructed with target controlling parameters  $P_M^{target} = 0.5$  and  $C_M^{target} = 0.55$ , as shown in Fig. 4.7b. It only takes 12 iterations to reach the convergence. This illustrates the flexibility of the proposed phase assignment algorithm in handling additional parametric variables of phase distribution.

Fig. 4.8 shows the history of the controlling parameters for the first numerical example (Fig. 4.7a). The result clearly indicates that, the initial “pseudo-density” of each cell is set as the target value of parameter  $P_M$ . The corresponding  $C_M$  equals to 0.22, which is lower than the target value and leads to a positive move in each cell. After 9 iterations, the phase distribution comes into a convergence. Therefore, a good-quality RVE is constructed with the targeted controlling parameters.

## 4.2. Identification of controlling parameters using POD approach

In this part, numerical tensile test is performed on artificial RVEs generated with various predefined controlling parameters. Using the AEH method, each artificial RVE can provide a prediction of flow stress. Here, a POD reduction approach [63, 64] is proposed to identify the optimal controlling parameters for a DP steel. Therefore, an inverse procedure is performed by interpolation to obtain the optimal values of  $P_M$  and  $C_M$ . We can consider a set of predicted flow curves of dimensionality  $N$ , which are resulted from discrete RVEs with various values of  $\mathbf{P} = \{(P_M^1, C_M^1), (P_M^2, C_M^2), \dots, (P_M^K, C_M^K)\}$ , as snapshots  $\mathbf{S}_k$ .

By assembling the snapshot matrix  $\mathbf{S}$ , the deviation and covariance matrices,  $\mathbf{D}$  and  $\mathbf{C}$  can be calculated as:

$$\mathbf{D} = [\mathbf{S}_1 - \bar{\mathbf{S}}, \mathbf{S}_2 - \bar{\mathbf{S}}, \dots, \mathbf{S}_K - \bar{\mathbf{S}}], \quad \mathbf{C} = \mathbf{D} \cdot \mathbf{D}^T \quad (4.11)$$

where  $\bar{\mathbf{S}} = \sum_{k=1}^K \mathbf{S}_k / K$  is the average snapshot. Making a reasonable assumption that the snapshot number  $K$  is much smaller than the dimension of one single snapshot  $N$ , each snapshot  $\mathbf{S}_k$  can be expressed as a linear combination of eigenvector  $\phi_i$  of matrix  $\mathbf{C}$ :

$$\mathbf{S}_k = \bar{\mathbf{S}} + \sum_{i=1}^K \alpha_{ik} \boldsymbol{\phi}_i \quad (4.12)$$

where  $\alpha_{ik} = \boldsymbol{\phi}_i^T (\mathbf{S}_k - \bar{\mathbf{S}})$  is the projection coefficient of the  $k$ -th snapshot on the  $i$ -th eigenmode. Accordingly, a projection space can be built using the POD modes as the orthogonal basis, where its origin is the mean snapshot. Therefore, each flow curve can be presented by its coordinates in the projection space.

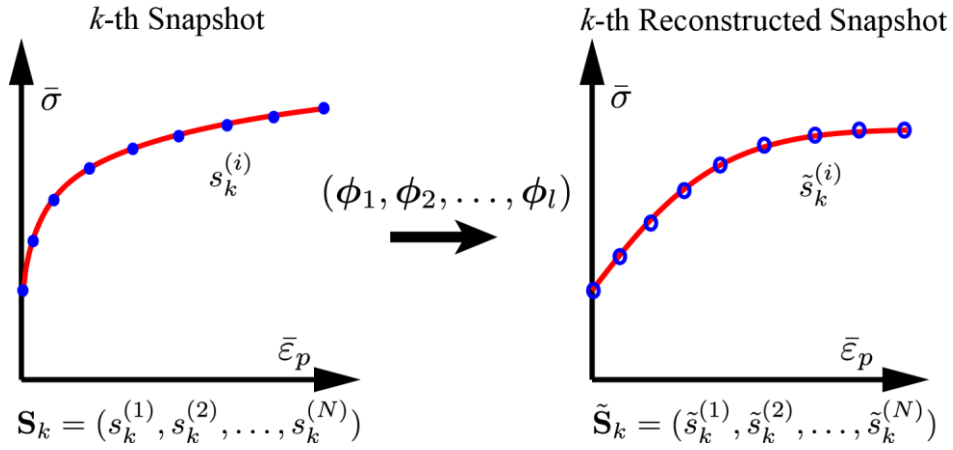


Figure 4.9: Reconstruction of the  $k$ -th snapshot using the retained POD modes.

In the conventional POD approach, the first  $l \ll K$  significant modes corresponding to the largest eigenvalues of the covariance matrix  $\mathbf{C}$ , can be utilized as a projection basis (also called as the retained POD modes) to reconstruct each snapshot:

$$\tilde{\mathbf{S}}_k = \bar{\mathbf{S}} + \sum_{i=1}^l \alpha_{ik} \boldsymbol{\phi}_i \quad (4.13)$$

where  $\tilde{\mathbf{S}}_k$  denotes the reconstructed snapshot. Fig. 4.9 gives an illustration of the snapshot reconstruction approach using finite number of POD modes. It clearly indicates that errors are introduced during the reconstruction process. Moreover, the reconstruction error  $\varepsilon$  between the flow curves  $\mathbf{S}_k$  and  $\tilde{\mathbf{S}}_k$  is given in terms of the number of retained modes  $l$ :

$$\varepsilon(l) = \frac{\sum_{i=1}^K (\mathbf{S}_k - \tilde{\mathbf{S}}_k)(\mathbf{S}_k - \tilde{\mathbf{S}}_k)^T}{\sum_{i=1}^K (\mathbf{S}_k - \bar{\mathbf{S}})(\mathbf{S}_k - \bar{\mathbf{S}})^T} \quad (4.14)$$

The error decreases as the number of retained modes increases. When it comes to an acceptable value, corresponding “energetic” modes are utilized to reconstruct each snapshot in the projection space.

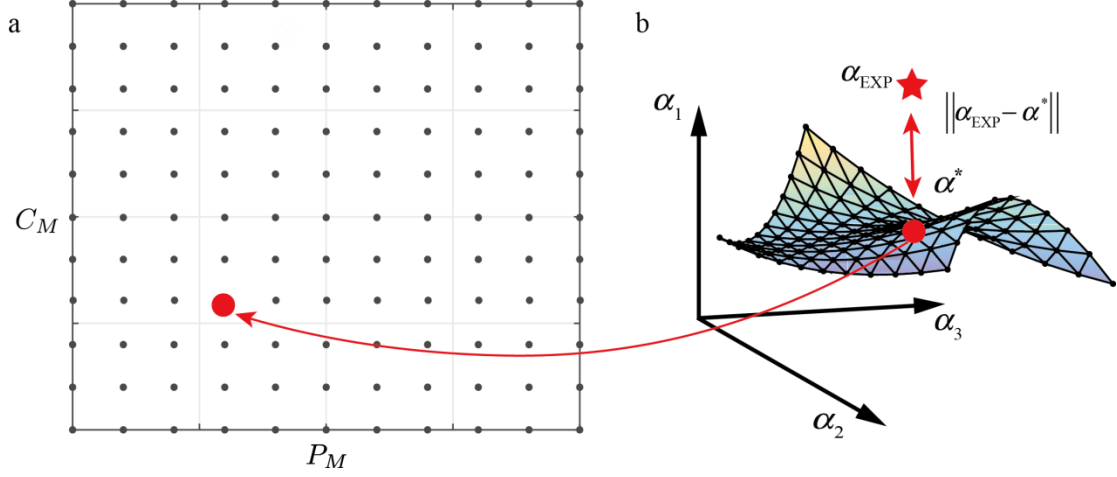


Figure 4.10: Illustration of: (a) the design space of controlling parameters and (b) the corresponding projection space.

Fig. 4.10a shows an example design space of the controlling parameters  $P_M$  and  $C_M$ , in which each point provides a flow curve snapshot. After analyzing the relationship of the reconstruction error versus the retained POD mode number, the first  $l$  modes are selected as the new proper orthogonal basis to construct the projection space ( $\alpha$  space). Each snapshot and the measurement are projected in this space, as shown in Fig. 4.10b. The difference between the predicted flow curve  $\alpha^*$  and the measured one  $\alpha_{\text{EXP}}$  is evaluated using the projected distance  $\|\alpha_{\text{EXP}} - \alpha^*\|$ . Therefore, for a given DP steel, an optimal design point of the controlling parameters can be identified using the POD approach. The integration of the POD method makes our generator suitable for comprehensive applications.

### 4.3. Parametric study of artificial microstructure generator

#### 4.3.1 Identification of optimal controlling parameter for DP590 steel

As discussed in Section 4.2, a POD approach is proposed to identify the optimal controlling parameters for a DP steel. In our case, the measured martensite fraction



$P_M$  of the DP590 steel is equal to 0.22. And, the martensite neighboring coefficient is assumed to vary in the range of [0.05, 0.5] to generate a set of artificial RVEs using the same modified Voronoi tessellation. The POD approach is applied to deal with the resulting flow curves and the reconstruction error is calculated using Eq. (4.14), as shown in Fig. 4.11a. Hence, this identification process becomes a 1D problem since the controlling parameter  $C_M$  is only varied to generate these discrete RVEs. It can also be seen that, the first most “energetic” mode already decreases the error to 0.04%. Consequently, only one mode is enough to reconstruct these flow curve snapshots.

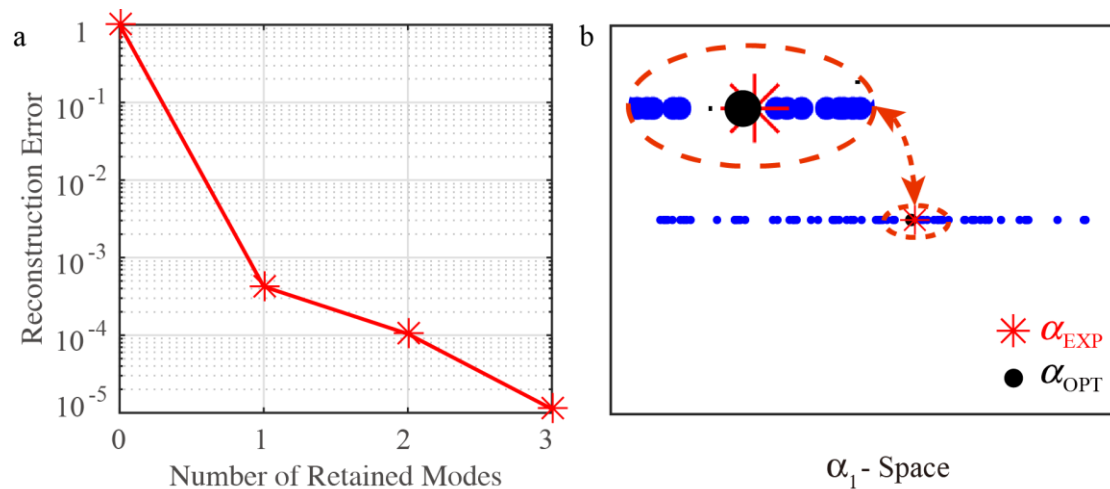


Figure 4.11: POD reduction: (a) reconstruction error and (b) snapshot projection in  $\alpha_1$ -space; red star: the projection of measurement, black dot: flow curve of RVE with optimal controlling parameters.

Fig. 4.11b shows the projection coefficient of each snapshots in  $\alpha_1$ -space that is reconstructed using the first most “energetic” mode. The measured flow curve of the DP590 steel is also projected in the space ( $\alpha_{EXP}$  in Fig. 4.11b), as *a priori*. In the projection space, if a point is nearer to the experimental star, the predicted flow curve of this RVE is closer to the measurement. We can observe that the RVE generated with  $C_M = 0.3$  ( $\alpha_{OPT}$  in Fig. 4.11b) provides the best fit with the measurements.

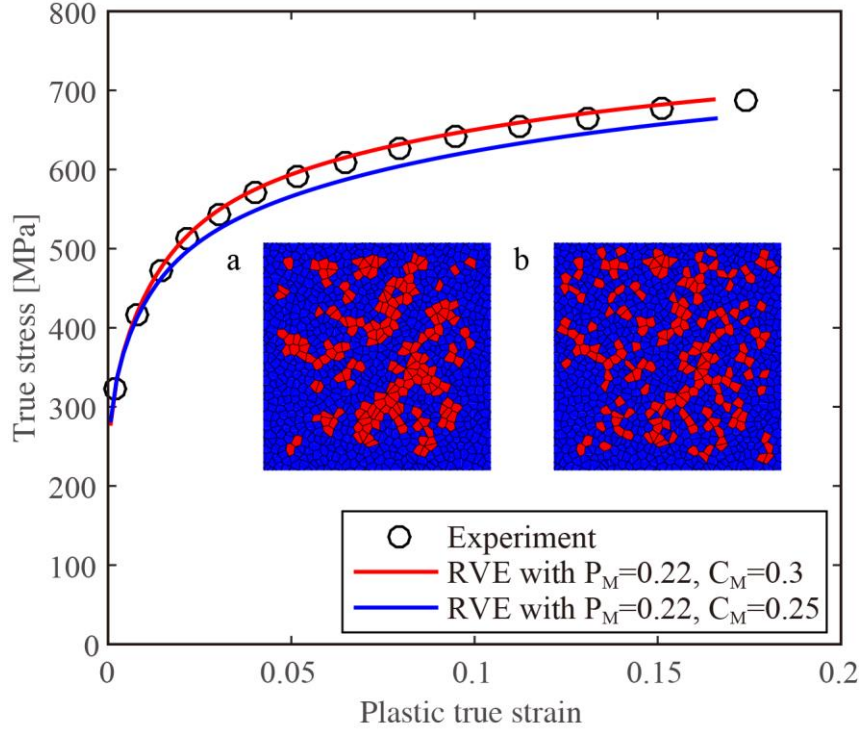


Figure 4.12: Comparison between the measurements and predicted flow curves of artificial RVEs using the modified Voronoï tessellation with controlling parameters: (a)  $P_M = 0.22, C_M = 0.3$  and (b)  $P_M = 0.22, C_M = 0.25$ .

The flow curves from artificial RVEs with different martensite neighboring coefficients are compared with the measurements, as show in Fig.4.12. The prediction of the artificial RVE with optimal controlling parameters is in good agreement with the experimental results. It indicates that the proposed POD approach is efficient to identify the optimal controlling parameter for a DP steel.

The artificial microstructures with  $C_M$  of 0.3 and 0.25 are also shown in Fig. 4.12a and b. By comparing these two microstructures, the martensite phase distribution in the first one (Fig. 4.12a) is more aggregative than the second one (Fig. 4.12b). Moreover, it is evident that the RVE with smaller  $C_M$  underestimates the flow stress of DP590 steel. The main reason of this phenomenon is that, the phase interface between ferrite and martensite in Fig. 4.12b is longer than in Fig. 4.12a. Since the existing heterogeneity at grain level tends to cause strain localization, the microstructure with longer ferrite-martensite interface boundary is prone to require less energy to develop the same plastic deformation. This confirms that the choice of the controlling parameters is proper to manipulate the phase assignment in artificial

microstructure. Therefore, the phase assignment algorithm based on topology optimization is able to cover a relatively comprehensive design space.

#### 4.3.2 Benefits of RVE generation within the modified Vorono tessellation

Since a modified Vorono tessellation is proposed in this study, this section focuses on investigating the influence of the tessellation used to generate the artificial RVE.

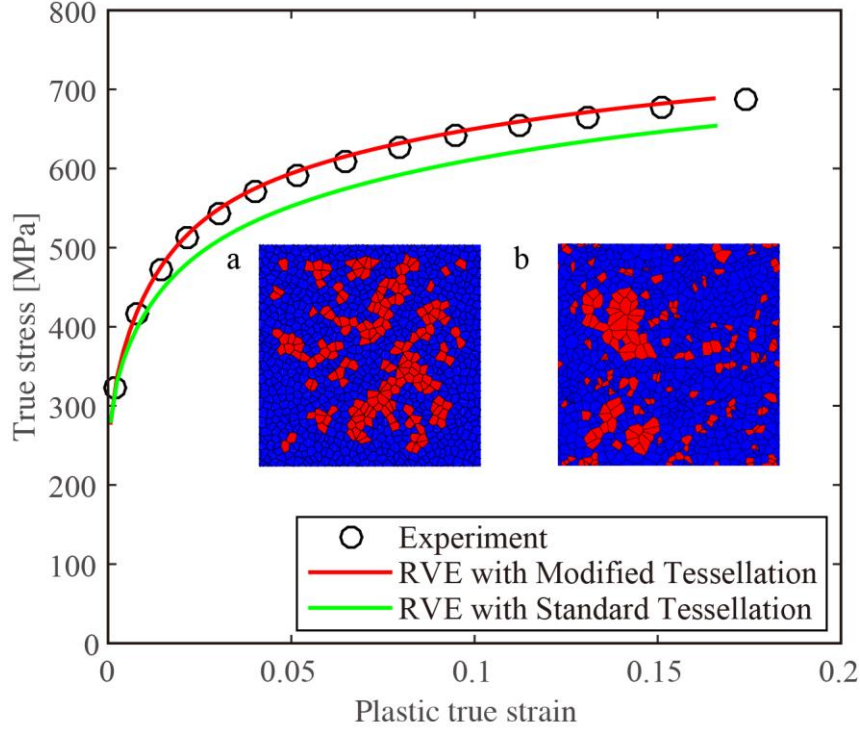


Figure 4.13: Comparison between the measurements and predicted flow curves of artificial RVEs generated from: (a) modified and (b) standard Vorono tessellations, with same controlling parameters:  $P_M = 0.22$ ,  $C_M = 0.3$ .

In Section 4.1.1, periodic Vorono tessellations are generated, in which Halton and pseudo-random sequences are utilized as generating seeds, as shown in Fig. 4.2. Moreover, optimal controlling parameter  $C_M$  is identified in the previous section. Using the phase assignment algorithm in Section 4.1.2 with the same controlling parameters, corresponding DP microstructures are constructed based on the modified Vorono tessellation and standard one, as shown in Fig. 4.13a and b. It can be clearly seen that, in the RVE generated from standard tessellation, there exists martensite grains with extremely large or small size and bad aspect ratio (Fig. 4.13b); these kinds of martensite grains have a significant influence on the martensite

neighboring coefficient  $C_M$ , while contribute limitedly to the martensite phase fraction  $P_M$ . Moreover, big martensite clusters are found in the RVE from standard tessellation, which affect the formation of shear bands along the ferritic-martensitic interface.

Fig. 4.13 also illustrates the comparison between the measurements and predicted flow curves from artificial RVEs. The RVE generated from the standard Voronoï tessellation grossly underestimates flow stress of DP590 steel. As discussed before, the existence of martensite grains with extreme size or bad aspect ratio causes that the variability of grain size is underestimated, while the number of nearest neighboring grains is overestimated. In addition, the grain morphology of the modified Voronoï tessellation is more regular than the standard one. It can reflect accurate martensite contiguity and morphology, which confirms the suitability of the proposed microstructure generator.

The results in Fig. 4.12 and 4.13 indicate the influence of controlling parameter  $C_M$  and Voronoï tessellation on the generated RVE and its flow curve prediction, respectively. Therefore, the RVE generated by predefining the optimal controlling parameters within the modified Voronoï tessellation, is called as the optimal artificial RVE in the following content.

#### 4.4. Validation of the optimal artificial RVE

As presented in Section 4.3.1, optimal controlling parameters are identified using the proposed POD reduction approach. Although the prediction of effective flow stress concurs the measurements, the local plastic deformation of the optimal artificial RVE must be validated by comparing with the SEM-based RVE. Meshed FE models of SEM-based and optimal artificial RVEs of DP590 steel are shown in Fig. 4.14a and b.

Tensile test simulation is performed on RVE models by prescribing a periodic boundary condition. In the periodic boundary condition, a global plastic strain of 17% is imposed to deform the RVEs, which guarantees that the stress level is below the material UTS (the uniform elongation is 18.5%). The results are compared with the measurements, as shown in Fig. 4.15. A small discrepancy is observed that, the simulated curves are slightly higher than the experimental result. This can be attributed to the utilization of plane strain assumption in the numerical simulations,

while the real specimen is subjected to 3D stress conditions. The similar difference has also been reported by Ramazani [30], and it increases with the volume fraction of martensite. Nevertheless, the SEM-based and optimal artificial RVEs provide accurate predictions of flow stress for DP590 steel.

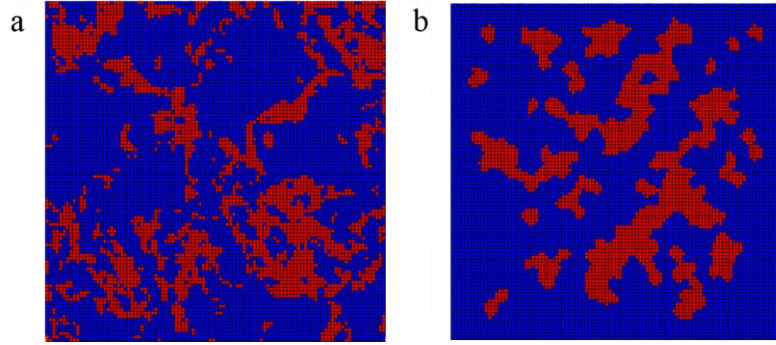


Figure 4.14: FE models with 0.25  $\mu\text{m}$  element size and 25  $\mu\text{m}$  edge length corresponding to: (a) SEM-based and (b) optimal artificial RVEs.

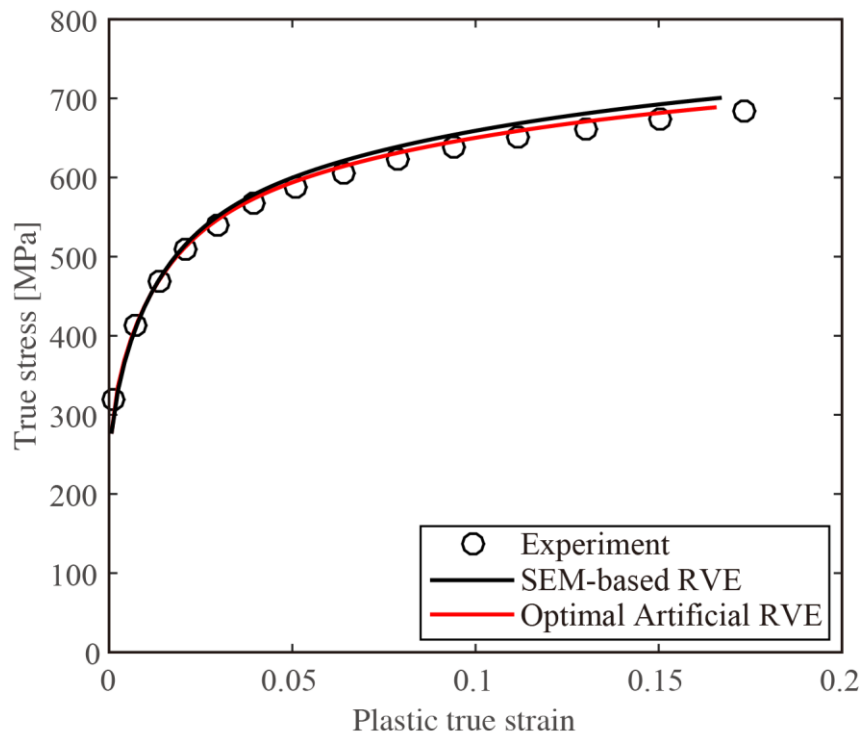


Figure 4.15: Comparison of between the measurement and the predicted flow curves of SEM-based and optimal artificial RVEs.

Fig. 4.16 and 4.17 show the equivalent plastic strain distribution in the SEM-based and optimal artificial RVEs at various global plastic strains. Although no material fracture or damage model is introduced, it is clearly found that shear bands are

formed in the ferrite matrix near martensite grains (Fig. 4.16c and Fig. 4.17c). Shear bands and localized plastic strain are caused by the heterogeneous microstructure of DP steel. Further details are shown in Fig. 4.18, which indicates the equivalent plastic strain distribution at global strain of 15.8% in the SEM-based and optimal artificial RVEs, and shear bands are located in the red ellipses. The direction of these shear bands is around  $45^\circ$  to the tensile loading direction. It can make a reasonable assumption that, if a ductile fracture model (e.g., GTN model) is adopted in ferrite matrix, as plastic flow accumulating, voids or microcracks are nucleated and formed in the strain localization zone. Moreover, it is notable that, the validation of the optimal artificial microstructure is performed with the uniaxial tensile test. Due to the heterogeneity of the DP microstructure, additional investigations can be implemented in the case of biaxial or shear tests.

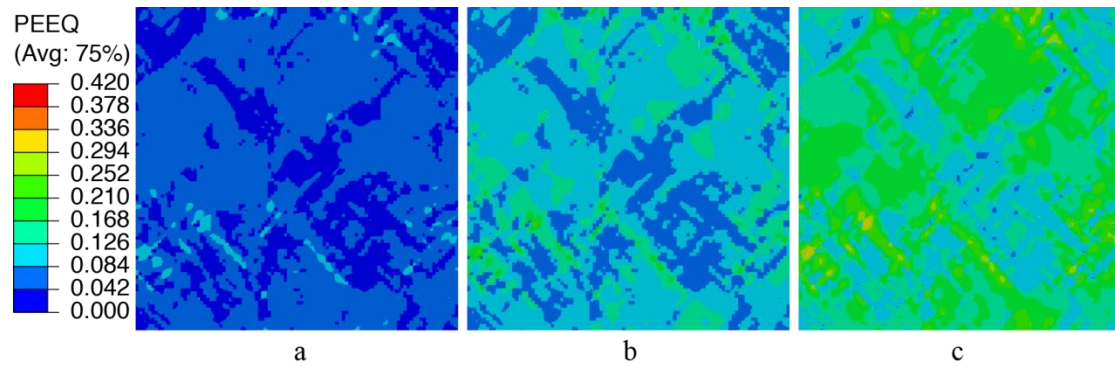


Figure 4.16: Equivalent plastic strain distribution in SEM-based RVE at various global plastic strain levels of: (a) 5.09%, (b) 10.01% and (c) 15.04%.

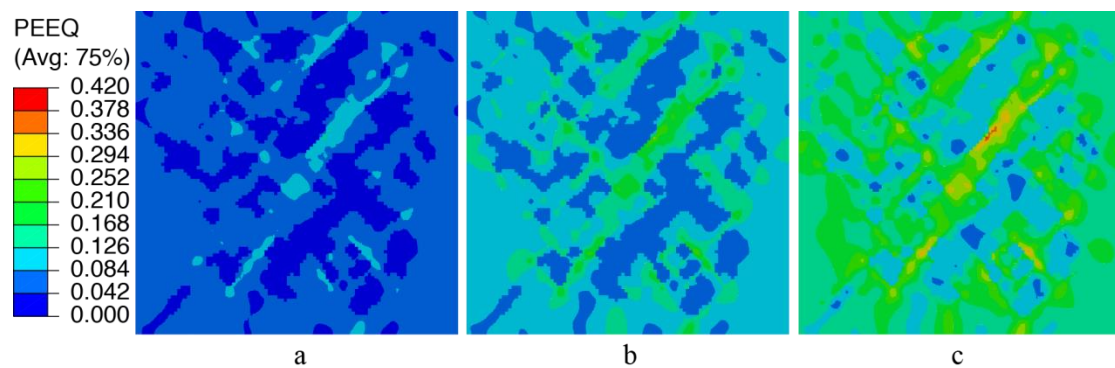


Figure 4.17: Equivalent plastic strain distribution in optimal artificial RVE at various global plastic strain levels of: (a) 5.09%, (b) 10.01% and (c) 15.03%.



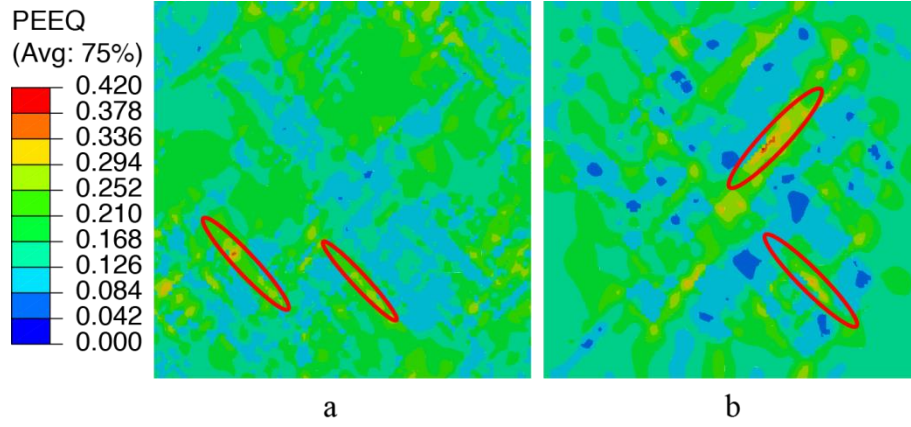


Figure 4.18: Equivalent plastic strain distribution at global plastic strain of 15.8% in (a) SEM-based and (b) optimal artificial RVEs, shear bands in red ellipses.

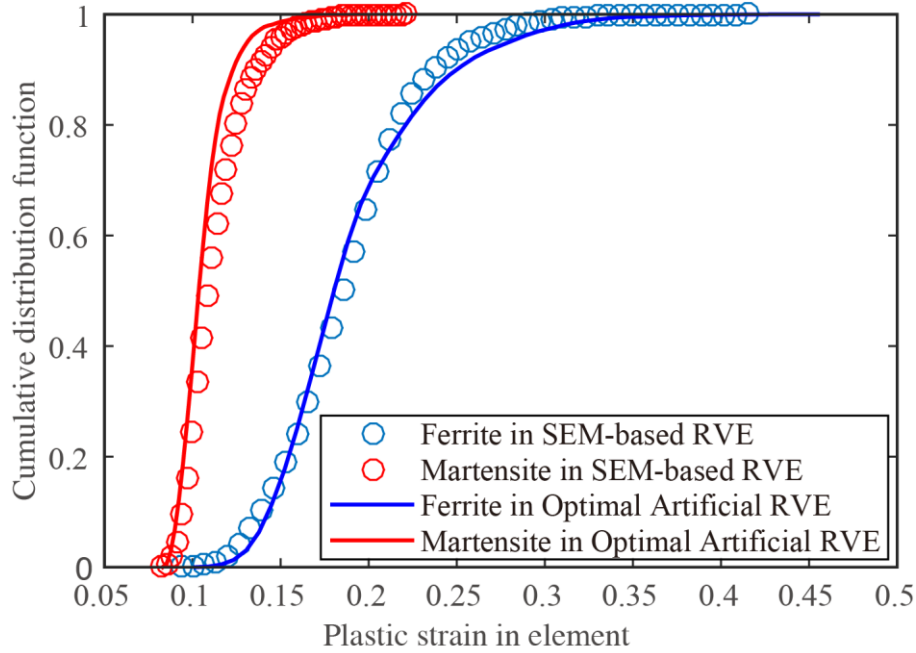


Figure 4.19: Cumulative distribution function of plastic true strain in ferritic and martensitic elements at global strain of 15.8%.

In order to validate our generator based on solid data, another comparison of the strain patterns in each RVE has been implemented. A statistical approach is adopted according to the following steps: firstly, it calculates the distribution of the equivalent plastic strain in ferritic and martensitic elements at the global strain of 15.8%. Secondly, the cumulative distribution function of element number in each strain interval is obtained to compare with the SEM-based RVE model, as shown in Fig. 4.19. A good agreement is observed from the comparison. This result confirms

that, optimal artificial RVE provides a good prediction of plastic strain patterns at the element level.

#### 4.5. Relation between controlling parameters

The optimal RVE was validated for DP590 steel in previous section. However, the identification process of the controlling parameter  $C_M$  needs to use the measured flow stress as *a priori*. That will significantly hold our protocol back to obtain the homogenized flow stress for DP steels in the practical application. Therefore, this section will focus on building interpolation between two controlling parameters ( $P_M$  and  $C_M$ ) based on limited number of trials on DP steels.

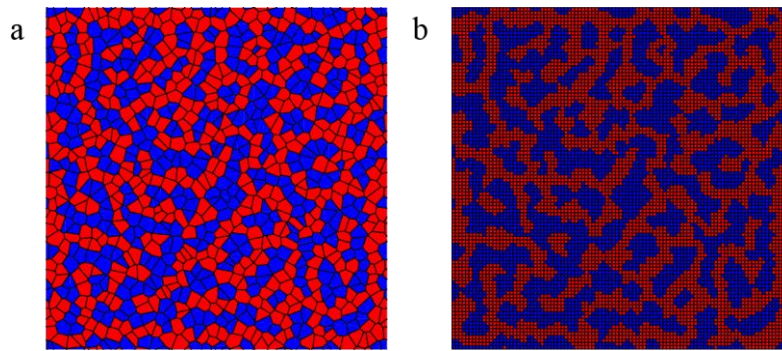


Figure 4.20: (a) Optimal artificial RVE with controlling parameters  $P_M = 0.55$ ,  $C_M = 0.56$ , and (b) the corresponding FE model for DP980 steel.

In order to construct the interpolation relationship between these two controlling parameters, another numerical application has been performed on DP980 steel by following the steps to obtain the optimal RVE. The corresponding controlling parameters are:  $P_M = 0.55$ ,  $C_M = 0.56$ . The same element of  $0.25 \mu\text{m}$  is utilized to discretize the resulted RVE. The optimal artificial RVE and FE model are shown in Fig. 4.20a and b, respectively.

By integrating the flow curve of each single constituent phase that is computed based on the dislocation theory and local chemical composition of DP980 steel, homogenized flow curve is compared with the measurement, as shown in Fig. 4.21. As presented in Section 4.4, the same discrepancy is observed from the comparison. The simulated flow curve from optimal artificial RVE is slightly higher than the experimental one.



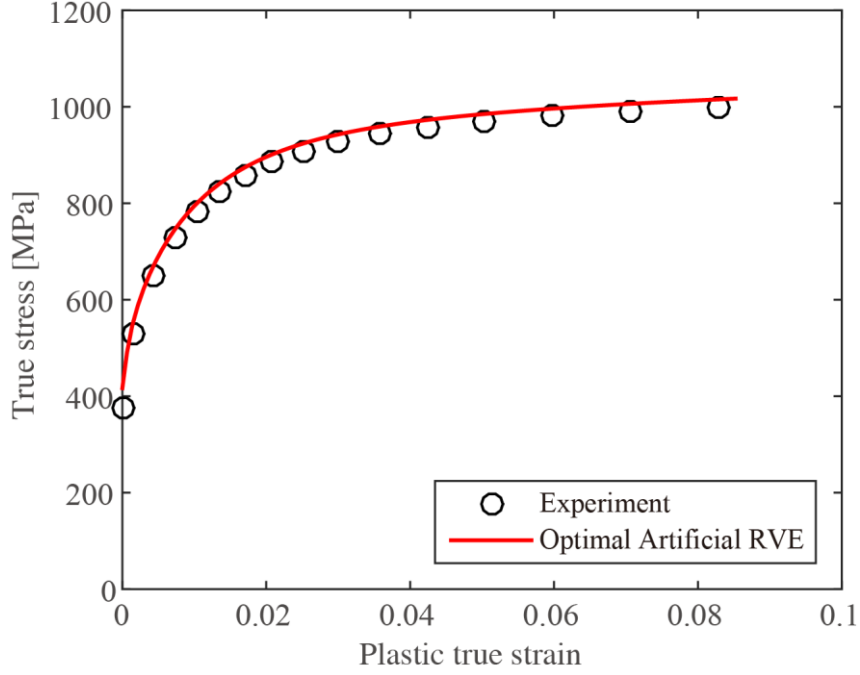


Figure 4.21: Comparison between the measurements and the predictions from the optimal artificial RVE for DP980 steel.

Steel degree	$P_M$	$C_M$
Pure Ferrite	0	0
DP590	0.2204	0.2933
DP980	0.5522	0.5605
Pure Martensite	1	1

Table 4.1: Steel degree and the corresponding optimal controlling parameters identified using the POD approach.

Therefore, the identified controlling parameters are validated for this DP980 steel. This couple of parameters is considered as the first group of trial data to obtain the interpolation relationship. Additionally, the controlling parameters related to pure ferrite and martensite are (0, 0) and (1, 1), respectively. Together with the optimal controlling parameters identified for DP590 steel, there are four couples of trial data, which are listed in Table 4.1, to construct a 3rd order polynomial interpolation relationship between the martensite phase fraction  $P_M$  and the neighboring coefficient of martensite grains  $C_M$ . The form of the aforementioned polynomial interpolation is given as:

$$C_M = -1.2850 \times 10^{-15} + 1.6838P_M - 1.8613P_M^2 + 1.1775P_M^3 \quad (4.15)$$

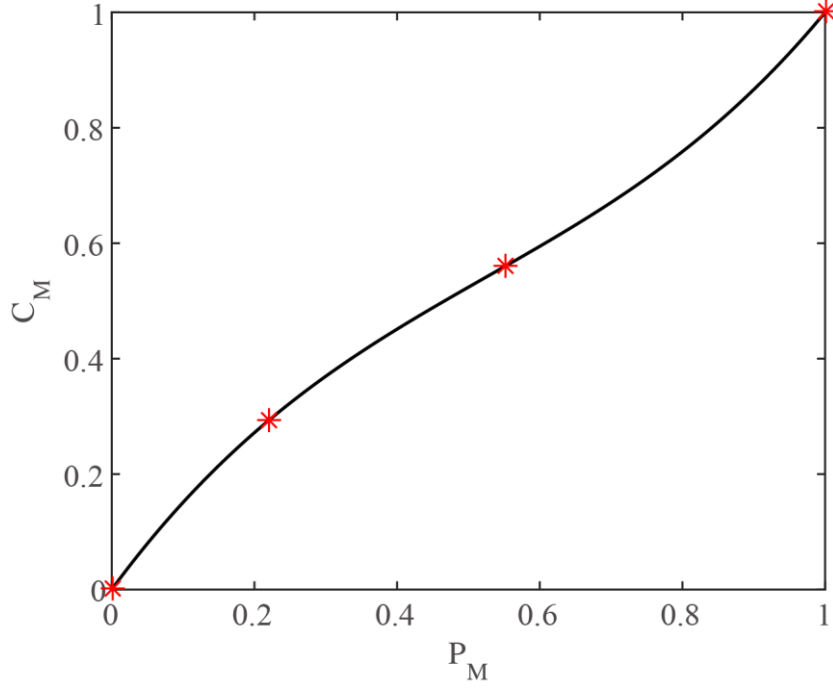


Figure 4.22: Interpolation relationship between the two controlling parameters based on limited number of trails on DP steels.

Fig. 4.22 shows the neighboring coefficient of martensite grains  $C_M$  as a function of the martensite phase fraction  $P_M$ , and the trial points are depicted by red stars. It indicates that there exists a positive correlation between these two parameters. With this correlation function and martensite phase fraction, the parameter  $C_M$  is computed. Therefore, an optimal RVE is generated based on the statistic description of microstructure from experimental measurement or phase transformation simulation. Moreover, the flow stress of target dual-phase or multi-phase material can be calculated using the asymptotic homogenization. In this way, our methodology gains dramatic advantages in industrial application.

#### 4.6. Conclusions

In this chapter, we proposed a novel artificial generator based on topology optimization to reconstruct the microstructure of DP steel. A modified Voronoi tessellation generated from Halton sequence, was utilized as the polycrystalline aggregate in the generator. Two microstructure parameters were introduced to control the phase

assignment process in the DP steel. The novel phase assignment algorithm deduced the discrete value problem to a continuous one by defining a so-called “pseudo-density” within the modified Voronoï tessellation. Artificial DP microstructures were convergently and rapidly generated with predefined controlling parameters. The optimal controlling parameter  $C_M = 0.3$  of DP590 steel has also been identified by a POD approach, which considered the experimental measurement, as *a priori*. Therefore, an optimal artificial RVE was constructed using the modified Voronoï tessellation and the optimal controlling parameters. The flow stress prediction using the optimal RVE agrees well with the measurements.

The effect of the used tessellations on the overall flow stress prediction of DP steel was investigated, in which the standard Voronoï tessellation is generated from pseudo-random sequence. The results showed that, grains with extreme size and bad aspect ratio existed in the RVE generated using the standard Voronoï tessellation. These low-quality grains caused the underestimation of the grain size variability and the overestimation of the nearest neighboring grain number variability, which further leads to a gross underrate on the overall flow stress prediction. Moreover, big martensite clusters were formed within the microstructure combining the phase assignment algorithm and the standard tessellation. This phenomenon affects the formation of shear bands along the ferritic-martensitic interface, which leads to an unreliable prediction. However, the utilization of the modified Voronoï tessellation in the RVE construction effectively prevents these drawbacks.

In order to validate the novel artificial generator, comparison of overall flow stress and plastic strain distribution was performed between SEM-based and optimal artificial RVEs for DP590 steel. It was shown that both of these RVE simulations can provide an accurate prediction. Moreover, shear bands were observed along the interface of different phase in each case. The path of shear bands is around  $45^\circ$  to the loading direction. It also concurs that, with the introduction of ductile fracture model, voids and microcracks can be formed in the strain localization zones. The statistical comparison of the equivalent plastic strain in ferritic and martensitic elements also showed that the optimal artificial RVE performed as well as the SEM based RVE at the element level.

In order to handle the high-dimension problems, such method has been extended with a polynomial interpolation approach to construct the correlation between these concerned parameters. Moreover, during the extension of the generator in 3D case,

the key difficulty is that, the computation time dramatically rose as dimension increases. Therefore, in future, further investigations will be performed to overcome these difficulties.

Overall, the promising results and the robustness of the proposed generator orient a new approach to predict the flow stress of the heterogeneous materials resulting from industrial forming processes.

## **Part II. Damage**

## **Chapter 5**

### **Introduction**

The previous part described the DP steel as the combination of hard martensite islands embedded into soft ferrite matrix, which enhances its mechanical properties. We also presented the possible ways to predict the flow stress of DP steel before the appearance of large deformation and fracture. However, the application of DP steel in the automotive industry is usually limited by its ductile fracture behavior that will finally lead to damage or failure of workpieces in car bodies after long-term utilization or traffic accident. Therefore, prediction of ductile fracture and damage of metals in engineering structure is an important but difficult topic in the automotive industries. During the last decades, a growing interest has been raised in ductile fractures modelling, which can be adopted in both sheet metal forming simulations as well as subsequent crash simulations.

#### **5.1. Background**

##### ***5.1.1 Damage problems***

Damage is usually described as complex physical phenomena concerned with the initiation, propagation and fracture of materials in engineering structures. In damage mechanics, typical engineering approaches and analysis are utilized to model the complex phenomena. According to Dusan Krajcinovic [81], “It is often argued that the ultimate task of engineering research is to provide not so much better insight into the examined phenomenon but to supply a rational predictive tool applicable in design”. The theoretical foundations and hypotheses of damage mechanics rely heavily on continuum mechanics. Most of the methods devoted to damage mechanics use state variables or indicators to represent the effects of damage on the remaining strength of material. The involved state variables can be measurable, e.g. void density, or computed based on the effect they have on macroscopic property, e.g. stiffness. Initially, the material is pristine, or intact. A fracture activation criterion is needed to predict fracture or damage initiation. It is necessary to develop a damage evolution model or method, since damage evolution does not continue

spontaneously after initiation. Combination of additional phenomenological parameters (e.g. void volume fraction) and hardening components need to be formulated in the evolution model.

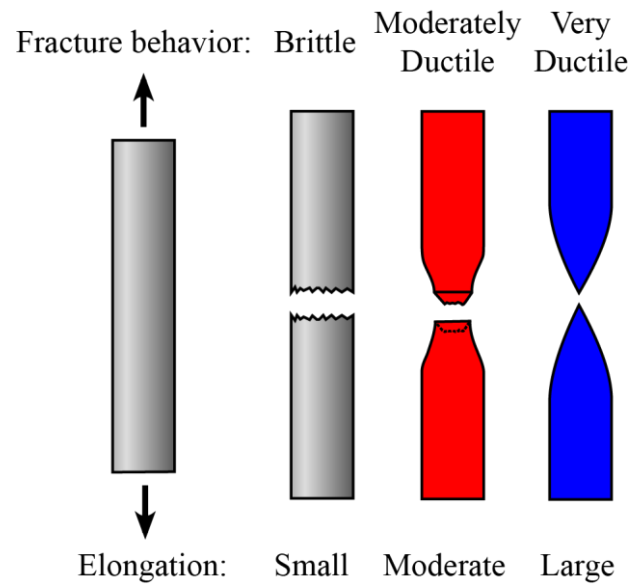


Figure 5.1: Ductile and brittle fracture behavior.

Generally, the damage mechanism can roughly be classified as brittle and ductile (Fig. 5.1). The brittle fracture occurs with little or no plastic deformation, which gives no warning of material failure or damage. In contrast, obvious warning (e.g. necking, large elongation) occurs before the onset of ductile fracture in engineering structures. The ductile fracture or damage will be our interest.

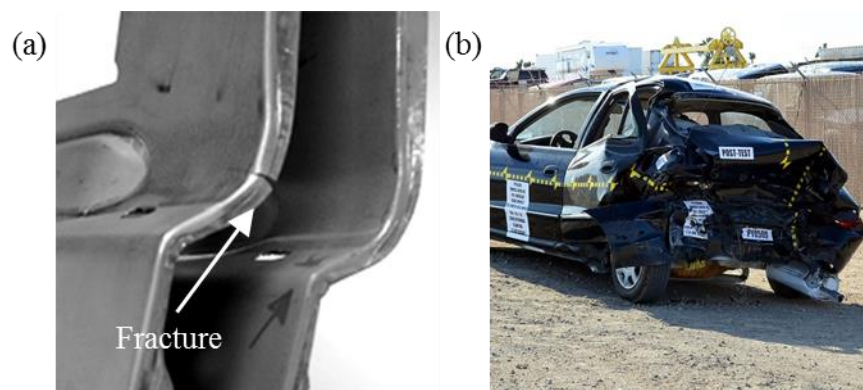


Figure 5.2: Damage problems in automotive: (a) edge fracture observed in carbody manufacturing [82] and (b) car crash test of a 2000 Hyundai Elantra [83].

The ductile fracture, which occurs with large plastic strain, is frequently observed in metal forming processes [82] (Fig. 5.2a). Moreover, another situation where the

ductile damage often happens, is in traffic collision or car crash test (Fig. 5.2b). Therefore, the accurate prediction or simulation of ductile fracture plays a significant role in the design and manufacture of lightweight vehicles. And, our interest will remain in the ductile damage of DP steel.

### 5.1.2 Damage of Dual-Phase steel

Generally, the damage of ductile materials is caused by the appearance of voids at micro scale. During more than three decades, numerous researchers have observed the ductile damage with help of microscopy, X-ray tomography, and divided it in three specific steps: nucleation, growth, and coalescence of micro voids. As shown in Fig. 5.3b, the damage of DP steel begins with micro-cavity nucleation, which often localized at weak material points, such as grain boundaries, martensite/ferrite interface. Then, as the voids grow and coalesce, local and micro cracks are formed and propagate in the material.

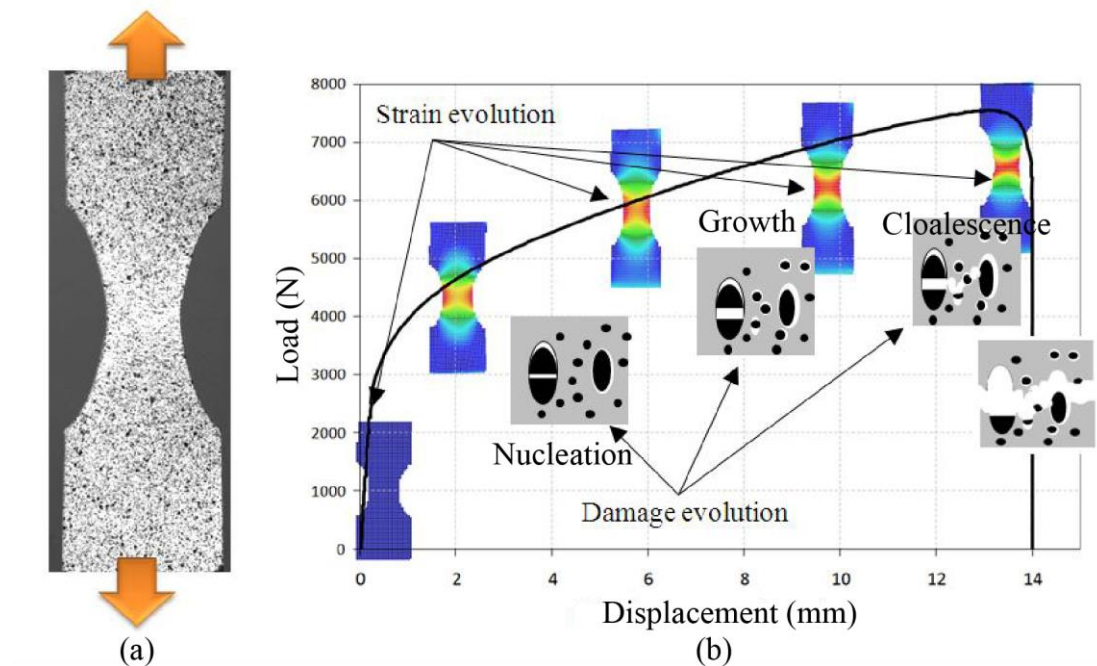


Figure 5.3: (a) Tensile test of notched plate specimen, (b) evolution of the damage process in a DP steel related to the macroscopic loading evolution [84].

According to the work of Avramovic et al. [85], the SEM observations of DP600 (Fig. 5.4) clearly reveals the sites of void nucleation, which mainly occurred by four different processes. At the strain levels of 0.5 and 1.02, a small amount of voids were nucleated by martensite particle cracking (Fig. 5.4b and c). The kind of void



nucleation mostly appears on coarse martensite particles, or particles intersected through plate-like martensite phase. And, the resulting voids usually do not seem to grow significantly, as shown in Fig. 5.4c and d. When it enters the high strain stage, the main source of void formation is along the ferrite/martensite interface by debonding. As plastic strain increases, the voids grow longitudinally along the grain boundaries (Fig. 5.4d and e). During the deformation process, these voids become efficiently large and the density increases, which contribute dramatically to the propagation of ductile cracks. Finally, the void coalescence results in shear bands (the dash line in Fig. 5.4f).

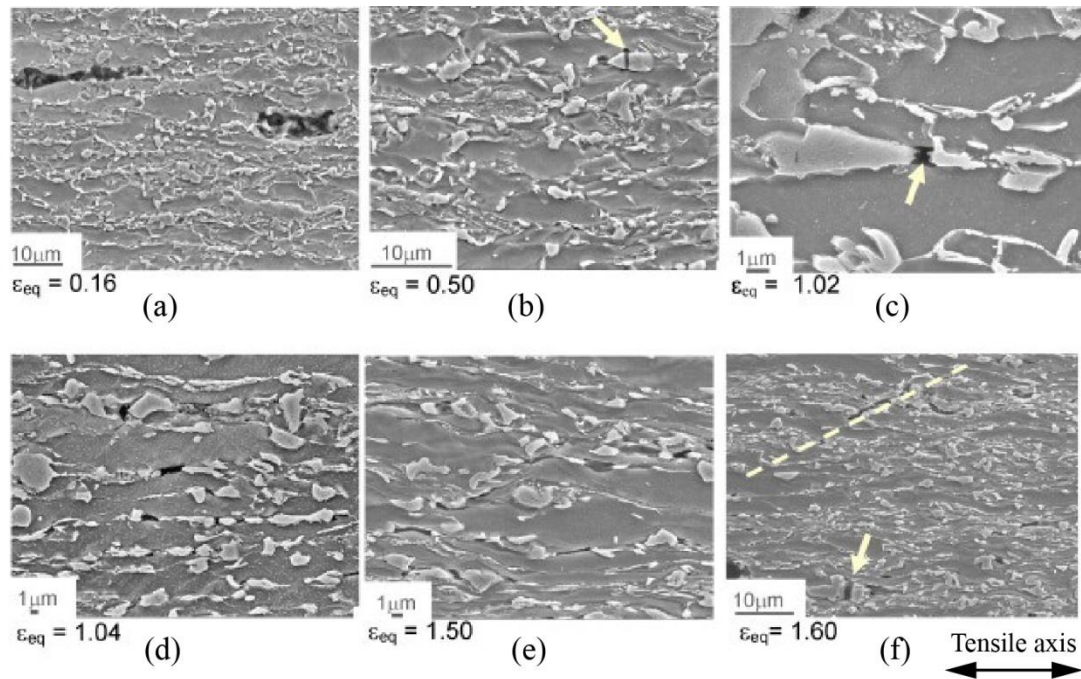


Figure 5.4: Void nucleation in the DP600 steel at various equivalent plastic strains: (a) on inclusion, (b) and (c) martensite cracking, (d) and (e) debonding at ferrite/-martensite interface and propagation along the ferrite grain boundaries, (f) coalescence of voids close to fracture surface [85].

## 5.2. Ductile fracture

As described in previous section, the ductile fracture is commonly presented by the nucleation, growth and coalescence of micro voids that ultimately results in crack formation and propagation. McClintock [86], Rice and Tracey [87] implemented their investigation on the evaluation of cylindrical and spherical inclusions in ductile matrices. Their researches have shown that void growth in ductile material is

governed by the stress triaxiality. Gurson [88] proposed a porous plasticity model that considers the void volume fraction in the ductile matrix as state variable. It describes the growth of voids and its influence on material's load carrying capacity before failure. Moreover, it makes use of a fundamental hypothesis that the ductile fracture takes place as the void volume fraction reaches critical value.

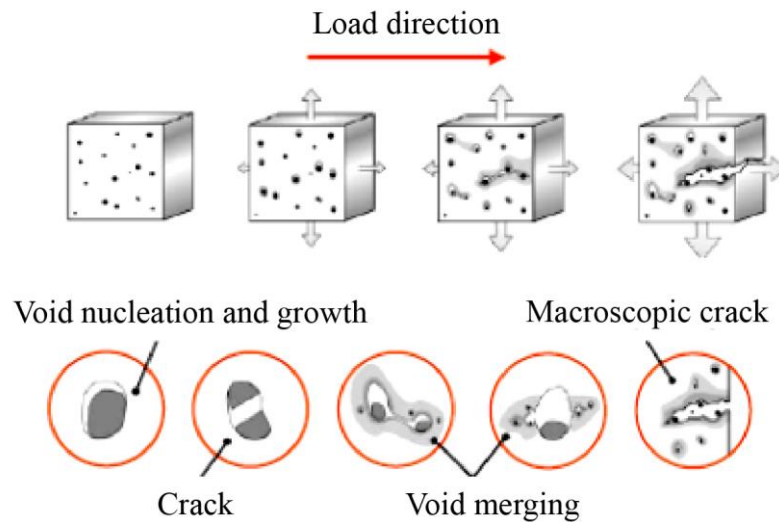


Figure 5.5: Stage of ductile failure: void nucleation, growth and coalescence according to GTN model [16].

According to these ductile fracture criteria, microstructure evolution represents a key feature to describe the softening mechanism (e.g. the reduction of the overall strength, caused by void growth and coalescence). Like the Gurson model, it assumes that voids always keep their shape while growing; when deviatoric stress state becomes dominant, alternative models have been proposed to achieve accuracy. The original Gurson model has been extended by considering the loss of load carrying capacity caused by void coalescence (e.g. Gurson-Tvergaard-Needleman model [89], shown in Fig. 5.5), by incorporating enhanced strain hardening models [90], by describing void shape effects [91] and by incorporating plastic anisotropy [92] and shear [93].

Alternatively, phenomenological models have been developed to predict ductile fracture without modelling micro voids. The development of these models is based on a reasonable assumption that ductile failure appears when a weighting indicator of the accumulated plastic strain reaches a critical threshold. According to the work of Bao and Wierzbicki [94], each of these models cannot provide an accurate prediction of fracture behavior for a given material within a large coverage of stress

triaxialities. Therefore, Bai and Wierzbicki [95,96], extended the classical Mohr-Coulomb fracture criterion to predict ductile fracture, which is also called modified Mohr-Coulomb (MMC) criterion. The weighting indicator of MMC criterion includes the equivalent plastic strain, stress triaxiality and Lode angle parameter of the stress state.

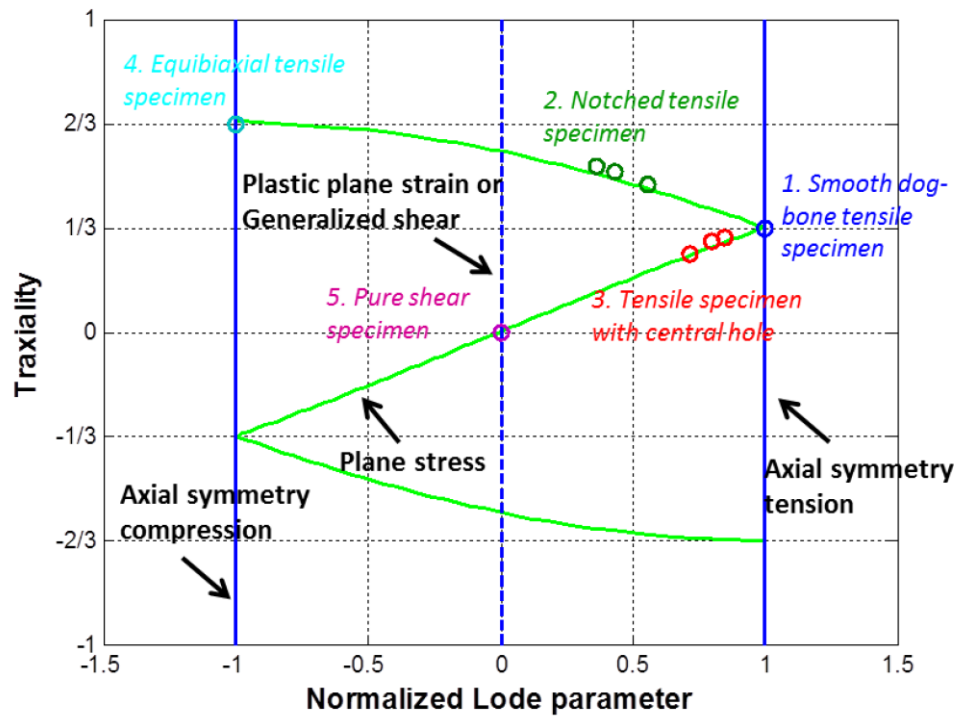


Figure 5.6: Experimental test plan on aluminum 2024-T351 covering large stress triaxiality range in the work of Bao *et al.* [94,95].

Recently, numerous experimental investigations have been performed to characterize and calibrate the material parameters prerequisite of different fracture criteria for various ductile metals. Clausen [97] performed an experimental study on axisymmetric and plane strain tensile fracture specimens of several materials and found a lower ductility for plane strain loading condition. Hancock and Mackenzie [98] studied the relationship between the ductility and the stress triaxiality for three different steels. They used smooth and U-notched axisymmetric tensile specimens and concluded that for all studied materials, the ductility is decreasing with stress triaxiality; they also found good agreement between their experimental results from notched axisymmetric specimens and flat grooved plane strain specimens and concluded that the ductility was determined by stress state, and not the strain state.

Using split Hopkinson bars, Johnson and Cook [99] performed dynamic torsion and notched tensile tests at different strain rates and temperatures. They concluded that the effect of stress triaxiality on the ductility of their tested metals was more significant than that of strain rate and temperature.

Bao [94] carried out an extensive experimental program on aluminum 2024-T351 covering stress triaxialities ranging from compression to multi-axial tension, as shown in Fig. 5.6. Bao's results proposed a transition region between shear and uniaxial tension, where ductility increases with stress triaxiality. Mohr and Henn [100] proposed a butterfly-shaped flat specimen to study the onset of fracture over a wide range of stress triaxialities. When using this specimen in conjunction with a dual actuator system [101], virtually any loading condition between pure shear and transverse plane strain tension can be imposed. In most fracture experiments on sheet materials, the localization of plastic deformation through necking cannot be avoided. After necking, the stress fields within the specimen gage section become non-uniform and three-dimensional in nature. Consequently, the stress history prior to fracture can no longer be estimated from the force history measurements using simple analytical formulations. Unless reliable in-situ neutron diffraction stress measurements [102] and three-dimensional tomography based digital image correlation measurements [103] are available, the stress and strain histories prior to fracture need to be determined in a hybrid experimental-numerical approach. In other words, a detailed finite element analysis of each experiment is required to identify the stress and strain fields. This forced marriage of experimental and computational mechanics involves the risk of adding up the errors from both the experiment and the numerical simulation [104].

### **5.3. Research objectives**

The second of this PhD thesis is the investigation of ductile fracture models and ductile damage mechanism of DP steel and a new calibration procedure with limited experimental tests, including smooth and notched specimens under uniaxial loading condition. The loading environment is room temperature and quasi-static loading; the used DP steel is assumed to be isotropic.

Commonly, the approaches include experimental investigation, finite element (FE) simulation and analytical solutions. In the experimental work, the uniaxial tests have been performed on both smooth and notched specimens. These tests could provide

the load-displacement response, the location and position of fracture initiation, as well as the fracture propagation mode. FE simulations are used to calculate all the stress states and strain components at the point of fracture initiation. Thus, this part proposes a bi-level reduced surrogate model to calibrate the material parameters in ductile fracture criteria. The method assembles local critical elements associated with global models. The surrogate model of fracture strain constructed using diffuse approximation [105,106] and the local element, reduces the computational effort for calibrating material parameters. Global fracture simulations are performed to update the target fracture strain and to compute the corresponding failure onset displacement. Convincing results are obtained via successive applications of design of experiments (DOE) [64,107] and enhanced design space transformation algorithms. The proposed identification protocol is validated for specific DP steel. Robustness of the method needs to be confirmed with different initial parameter values.

In order to achieve the above research goals, our work can be divided into the following parts:

- Study different types of ductile fracture and damage model, select the proper one to describe and predict damage of the investigated material;
- Design and carry out the experimental test plan, record the response of load-displacement curve;
- Perform numerical simulations without fracture model of same tested specimens to record stress states of the local critical elements;
- Develop a bi-level reduced surrogate model to calibrate the material parameters in the chosen fracture criterion, verify its reliability;
- Perform and demonstrate the new identification protocol by application on specific DP steel.

Therefore, the structure of this part is organized in the following manner: Chapter 6 presents the review of popular ductile fracture and damage models; Chapter 7 gives details of the experimental work and the bi-level reduced surrogate model for identification of material parameters in MMC criterion that is constructed using DOE and diffuse approximation approaches.

## Chapter 6

### Literature review

The previous chapter gives a brief review of the ductile damage problems of DP steel in automotive industry. Although the special microstructure of DP steel makes it possess several advanced mechanical properties, these ductile damage problems limit its application in engineering structures. Therefore, this chapter will describe the review, which is focused on the ductile fracture and damage modelling approach. Moreover, it presents several methods including experimental and numerical techniques, to calibrate the material parameters for fracture criteria.

#### 6.1. Ductile fracture criteria

Recently, prediction of ductile fractures of DP steels in engineering structures is becoming a topic of great importance in the automotive industry. For example, research investigations have been performed by industrial engineers to reduce the weight of car bodies while maintaining their performance and safety features. As the massive application of DP steel in car manufacturing, the strength has been significantly increased, the ductility has been decreased. Therefore, ductile fracture becomes a major challenge in the design of vehicles with DP steel. There are various types of fracture, such as, forming fracture, edge crack, crushing fracture. Over several decades, different micro-/macroscopic models have been proposed to describe the ductile fracture of metals. Classical cylindrical inclusion growth model [86], spherical hole growth model [87], GTN porous plasticity model [88,89], damage mechanics [108], phenomenological fracture models (e.g. Cockcroft-Latham damage model [109], Wilkins model [110], Johnson-Cook model [99], cohesive element approach [111], and MMC model [95,96]). This section is concerned with the aspects of GTN and MMC fracture criteria.

##### *6.1.1 Gurson-Tvergaard-Needleman (GTN) fracture criterion*

Gurson [88] proposed a damage mechanics material model based on the observation that available plasticity models, such as the von Mises model, were predicting

incompressibility, although ductile rupture could involve significant porosity. Tvergaard and Needleman [89] modified the basic model through replacing the void volume fraction  $f$  by the modified damage parameter  $f^*$  in the GTN model to reflect the void coalescence process after the void volume fraction reaches a critical value. Today, the Gurson damage model [88] with this modification is the model of choice for crash simulations. The basic yield potential function for a ductile matrix material containing a spherical inclusion can be expressed as:

$$\Phi_{GTN} = \left[ \frac{\bar{\sigma}}{\sigma_Y(\bar{\varepsilon}_p)} \right]^2 + 2q_1 f^* \cosh \left[ q_2 \frac{3\sigma_m}{2\sigma_Y(\bar{\varepsilon}_p)} \right] - (1 + q_3 f^{*2}) = 0 \quad (6.1)$$

where  $\bar{\sigma}$  is the von Mises stress,

$$\bar{\sigma} = \sqrt{\frac{3}{2} \mathbf{s} : \mathbf{s}}, \quad \mathbf{s} = -\sigma_m \mathbf{I} + \boldsymbol{\sigma}, \quad \sigma_m = \frac{1}{3} \text{tr}(\boldsymbol{\sigma}) \quad (6.2)$$

$\sigma_Y$  is the yield stress of the principal phase material, which is a function of the equivalent plastic strain  $\bar{\varepsilon}_p$  in the ductile matrix,  $\sigma_m$  is the hydrostatic stress and  $\mathbf{I}$  is the second-order identity tensor. In the temperature and strain rate independent GTN model [89], it exists 9 free parameters.  $q_1$ ,  $q_2$  and  $q_3$  are phenomenological fitting parameters;  $q_1$  affects the yielding by modifying the void volume fraction,  $q_2$  can be considered as a corrective factor for the hydrostatic stress, and  $q_3$  is related to  $q_1$  with  $q_3 = q_1^2$ . Consequently, these three parameters have an influence on the form of the yielding surface. Moreover, the modified damage parameter  $f^*$  that takes account of void nucleation and coalescence is defined by:

$$f^* = \begin{cases} f & \text{if } f \leq f_C \\ f_C + \frac{\bar{f}_F - f_C}{f_F - f_C} (f - f_C) & \text{if } f_C \leq f \leq f_F \\ \bar{f}_F & \text{if } f \geq f_F \end{cases} \quad \text{where } \bar{f}_F = \frac{q_1 + \sqrt{q_1^2 - q_3}}{q_3} \quad (6.3)$$

where  $f_C$  is the critical void volume fraction,  $f_F$  is the void volume fraction at which material completely loses stress carrying capability (also called void volume fraction at fracture). Together with the initial void volume fraction  $f_0$ , they are another three specific parameters. The parameters  $\varepsilon_N$ ,  $s_N$  and  $f_N$ , which define the strain controlled void nucleation under loading, will be explained as follows.

In metal plasticity, isotropy assumption is used in the yield surface. A plastic flow rule is adopted:

$$\dot{\boldsymbol{\varepsilon}}_p = \dot{\lambda} \frac{\partial \Phi_{GTN}}{\partial \boldsymbol{\sigma}} \quad (6.4)$$

where  $\dot{\lambda}$  is the plastic multiplier. Since the plastic hardening of the ductile matrix is described using the function  $\sigma_Y(\bar{\varepsilon}_p)$ . The evolution of the equivalent plastic strain in the matrix material  $\varepsilon_M$  can be obtained from the plastic work expression:

$$(1-f)\sigma_M \dot{\varepsilon}_M = \boldsymbol{\sigma} : \dot{\boldsymbol{\varepsilon}}_p \quad (6.5)$$

And, the total change of the void volume fraction  $f$  is given as:

$$\dot{f} = \dot{f}_G + \dot{f}_N = (1-f)\dot{\varepsilon}^p : \mathbf{I} + A\dot{\varepsilon}_M \quad (6.6)$$

where  $\dot{f}_G$  is the change due to the growth of existing voids and  $\dot{f}_N$  is the change due to the nucleation of new voids. Growth of existing voids is based on the law of conservation of mass and the assumption that the matrix material is plastically incompressible. In other words, the total volume of the main phase material is unchanged. Nucleation of the new void occurs principally along the interface between ferrite matrix and martensite islands. Different kinds of nucleation criteria have been formulated within this general phenomenological framework. In the GTN fracture model, it only can be controlled by the plastic strain of matrix material. The multiplier  $A$  describes the dependence of the void nucleation rate on the main effective plastic strain increment. The function  $A$  is given as:

$$A = \frac{f_N}{s_N \sqrt{2\pi}} \exp \left[ -\frac{1}{2} \left( \frac{\varepsilon_M - \varepsilon_N}{s_N} \right)^2 \right] \quad (6.7)$$

where  $f_N$  denotes the total void volume fraction to be nucleated,  $\varepsilon_N$  is the average nucleation strain and  $s_N$  represents the standard deviation of the Gaussian void nucleation strain distribution.

### 6.1.2 Modified Mohr-Coulomb (MMC) fracture criterion

The original M-C fracture model [112] has been widely used in rock and soil engineering. It could provide a good mechanical behavior prediction for materials



which fail in the elastic range or under small plastic strain, like rock, soil, concrete and so on.

A modified version of the M-C model is proposed as an adequate fracture model in calibration and identification work. The original M-C model is written in stress space and assumes that the fracture occurs when the combined normal and shear stresses on any plane of normal vector  $\mathbf{n}$  meet the following condition [96]:

$$\max_{\mathbf{n}} (\tau + c_1 \sigma_n) = c_2 \quad (6.8)$$

where  $c_1$  is the coefficient of friction and  $c_2$  is the shear resistance. Bai and Wierzbicki [96] transformed Eq. (6.8) into the space of stress triaxiality ( $\eta$ ), normalized Lode angle parameter ( $\bar{\theta}$ ) and equivalent plastic strain at fracture ( $\bar{\epsilon}_f$ ) assuming proportional monotonic loading, in a spherical coordinate system. The resulting explicit expression for the fracture strain is given by [96]:

$$\begin{aligned} \bar{\epsilon}_f = & \left\{ \frac{K}{c_2} \left[ c_3 + \frac{\sqrt{3}}{2 - \sqrt{3}} (c_\theta - c_3) \left( \sec \left( \frac{\bar{\theta}\pi}{6} \right) - 1 \right) \right] \left[ \sqrt{\frac{1 + c_1^2}{3}} \cos \left( \frac{\bar{\theta}\pi}{6} \right) \right. \right. \\ & \left. \left. + c_1 \left( \eta + \frac{1}{3} \sin \left( \frac{\bar{\theta}\pi}{6} \right) \right) \right] \right\}^{-1/n} \end{aligned} \quad (6.9)$$

and

$$c_\theta = \begin{cases} 1 & \text{for } \bar{\theta} \geq 0 \\ c_\theta & \text{for } \bar{\theta} < 0 \end{cases} \quad (6.10)$$

where  $K$  and  $n$  are the fitting parameters of flow stress obtained using the classical Swift law.  $c_3$  and  $c_\theta$  describe the dependence of the underlying plasticity model on the third stress invariant. The free model parameters ( $c_1, c_2, c_3, c_\theta$ ) have to be calibrated based on fracture experiments.

In Eq. (6.10), the stress triaxiality is defined as the ratio between the hydrostatic stress ( $\sigma_m$ ) and the von Mises equivalent stress ( $\bar{\sigma}$ ):

$$\eta = \frac{\sigma_m}{\bar{\sigma}} \quad (6.11)$$

with  $-\infty \leq \eta \leq \infty$ . The Lode angle parameter is normalized as:

$$\bar{\theta} = 1 - \frac{6\theta}{\pi}, \quad 0 \leq \theta \leq \frac{\pi}{3} \quad (6.12)$$

and lies in the range of  $-1 \leq \bar{\theta} \leq 1$ . The Lode angle is computed using:

$$\cos(3\theta) = \frac{27}{2} \frac{(\sigma_I - \bar{\sigma})(\sigma_{II} - \bar{\sigma})(\sigma_{III} - \bar{\sigma})}{\bar{\sigma}^3} \quad (6.13)$$

where  $\sigma_I, \sigma_{II}$  and  $\sigma_{III}$  are the principal stresses. Further details of the space transformation are given in the work of Bai and Wierzbicki [95].

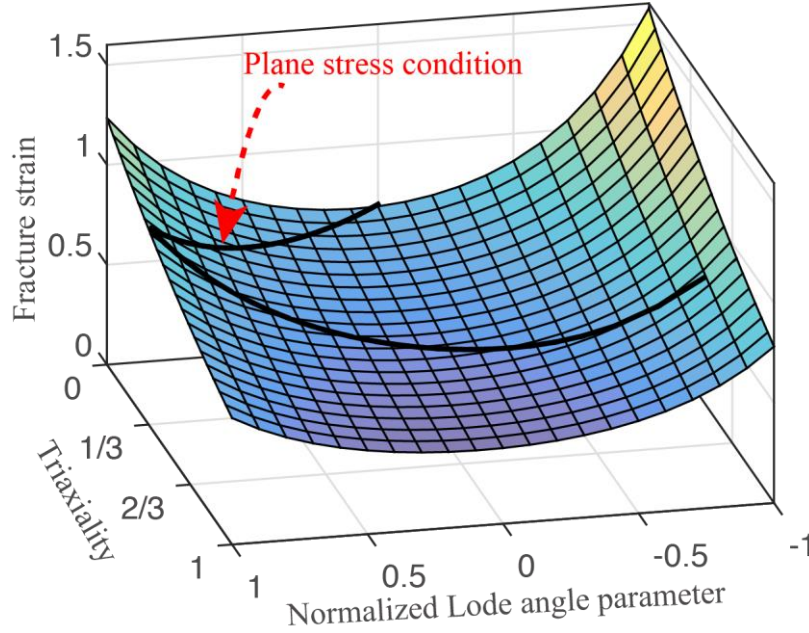


Figure 6.1: Illustration of the MMC fracture criterion in  $(\eta, \bar{\theta}, \bar{\epsilon}_f)$  space. The solid line depicts the plane stress condition.

In order to facilitate the utilization of the MMC model for sheet metal, Wierzbicki and Xue [113] proposed a plane stress formulation, in which the stress triaxiality and the normalized Lode angle parameter are related by:

$$\cos\left[\frac{\pi}{2}(1 - \bar{\theta})\right] = -\frac{27}{2}\eta\left(\eta^2 - \frac{1}{3}\right) \quad (6.14)$$

Therefore, a plane stress fracture curve (the solid line in Fig. 6.1) can be projected on the fracture surface (in Fig. 6.1) using Eq. (6.14). Fig. 6.2 depicts the fracture locus in the plane  $(\eta, \bar{\epsilon}_f)$ , which needs to be calibrated and determined based on the designed fracture tests. The analytical stress states of the smooth and notched specimens are denoted with red, green and blue dots in Fig. 6.2.

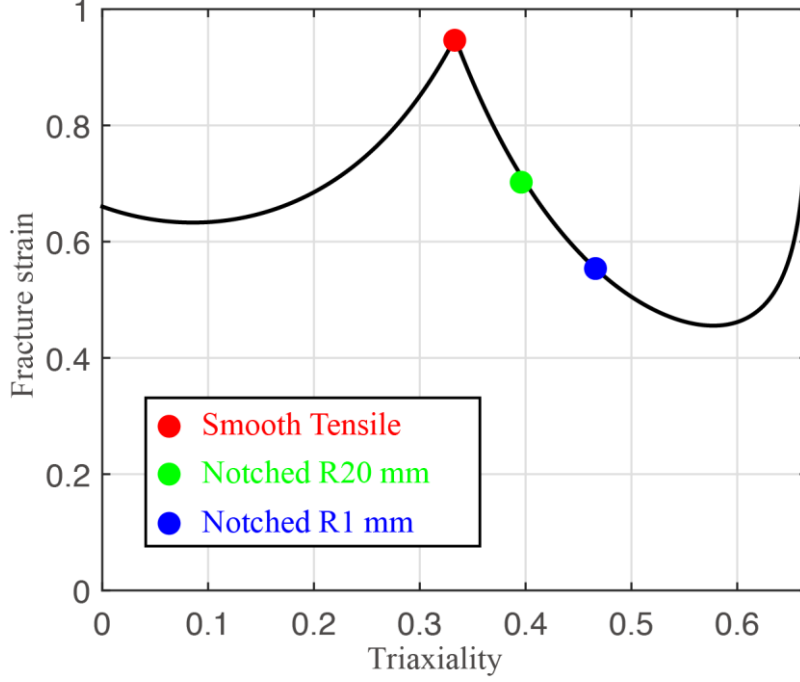


Figure 6.2: Projection of the MMC fracture surface in  $(\eta, \bar{\epsilon}_f)$  plane. Red, green and blue dots depict the stress states of the designed fracture tests.

In the case of proportional loading, the corresponding damage evolution indicator of the fracture model can be expressed using an integration form that is proposed by Bai and Wierzbicki [96]. The integral formulation is governed by a linear relation between the damage indicator and the equivalent plastic strain:

$$D(\bar{\epsilon}_p) = \int_0^{\bar{\epsilon}_p} \frac{d\bar{\epsilon}_p}{\bar{\epsilon}_f(\eta, \bar{\theta})} \quad (6.15)$$

When the limit of strength is reached, the damage indicator  $D(\bar{\epsilon}_p)$  of the critical material element reaches the threshold value of 1, and leads to element elimination from FE model. The fracture onset displacement referred to the critical element elimination, is considered as the simulated fracture onset displacement, while the exact value is identified from experiments. The calibration of the parameters in MMC fracture criterion is performed using an optimization approach to minimize the gap between the predictions and measurements.

Due to the application range and nature of the experimental testing condition, the normalized Lode angle parameter is always greater than 0. Based on Eq. (6.10), a simplified three parameter version of the modified Mohr-Coulomb fracture (MMC3) [114] model can be obtained by setting the parameter  $c_\theta$  to 1. Therefore, the remain-

ing unknown parameters become  $(c_1, c_2, c_3)$ . By this way, three groups of fracture experiments are sufficient to identify those parameters.

## 6.2. Calibration of ductile fracture criteria

In order to integrate the GTN criterion within the FE computation, nine parameters  $(q_1, q_2, q_3, f_0, f_C, f_F, \varepsilon_N, s_N, f_N)$  are needed to identify from the experimental calibration process. The values  $q_1 = 1.5, q_2 = 1.0$  and  $q_3 = 2.25$  were recommended in the investigations of Tvergaard and Needleman [89]. The initial void volume fraction  $f_0$ , standard deviation  $s_N$ , mean equivalent plastic strain  $\varepsilon_N$ , volume fraction of secondary voids  $f_N$ , critical void volume fraction  $f_C$  and the final void volume fraction  $f_F$  should be extracted from the experimental measurements. Several direct methods have been proposed to identify these 6 parameters by examining the fracture surface and analyzing the particles of the investigated material, namely fractography based on X-ray tomography. While, as discussed previously, only three groups of fracture tests are necessary to calibrate the 3 unknown parameters for the MMC3 criterion. Therefore, the next section will focus on the calibration methods to identify the material parameters for different ductile fracture criteria.

### 6.2.1 X-ray tomography techniques

The correct identification of the material parameters in GTN model is a prerequisite for successful analysis and prediction of the ductile failure with this model. Ben Bettaieb *et al.* [115,116] investigated the material parameters of a GTN porosity based plastic damage model through X-ray tomography measurements method and in-situ tensile test. In their work, the porosity evolution was predicted with a micro-mechanical model combined with 3D experiments tests. Both of damage parameters representing the void nucleation and growth need to be quantified for a smooth dog-bone specimen of DP steel [117,118].

Commonly, the X-ray micro-tomography can be utilized to image and quantify the microstructure of multi-phase materials. Various researchers have performed studies on damage in ductile materials. In the work of Landron *et al.* [119], they used the tomography setup in the ID15A beam line at the European Synchrotron Radiation Facility (ESRF) in France. By combining a high-efficiency scintillator screen, a reflecting microscope objective and a fast charge-coupled device (CCD) detector,

they acquired an unprecedented radiography with high acquisition speed. The spatial beam radiation measured is  $2\text{ }\mu\text{m}$  and the voxel size is  $1.6\times 1.6\times 1.6\text{ }\mu\text{m}^3$ .

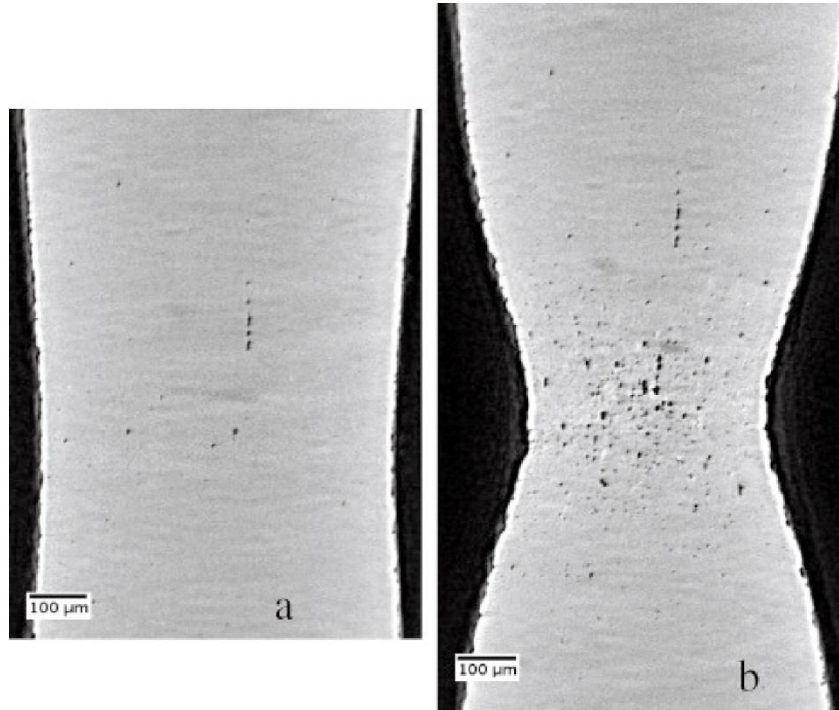


Figure 6.3: Tomographic slices parallel to the tensile direction at the steps: (a) just after necking and (b) just before fracture [118].

The central area of the dog-bone specimen was utilized to quantify the damage. The useful observation volume of the sample was  $1\times 1\times 1\text{ }\mu\text{m}^3$  parallelepiped. Only the central part, 1.4 mm in height, was imaged during their study, as shown in Figs. 6.3 and 6.4. In fact, Fig. 6.3a and b show the typical evolution of a reconstructed vertical section of the central part of the dog-bone specimen. These sections that are parallel to the tensile axis were acquired from the tomographic 3D block at tensile test stages: (a) just after necking and (b) just before fracture, respectively. A massive amount of cavities that are related to the void nucleation, growth and sometimes coalescence are clearly shown in these sections.

Additionally, in Fig. 6.4, a 3D rendering of the external shape of the specimen including the cavities for (a) the initial state and (b) the instant corresponding to the fracture onset. In this figure, the ferrite matrix is denoted with semitransparent gray color, and the cavities are denoted with black color to present their locations. These grayscale images can be directly binarized by defining a threshold to differentiate the voxels belonging to the cavities from those belonging to the matrix phase. The

perspective view makes the insertion of a scale bar inappropriate. The dimension of the reconstructed bloc is  $1 \times 1 \times 1.5$  mm. It is assumed that the central part of the specimen undergoes the highest stress triaxility and strain. However, when necking occurs, several points of the matrix material are eliminated from the analysis. These material points are far from the neck so that they are the less active zones as far as damage is concerned.

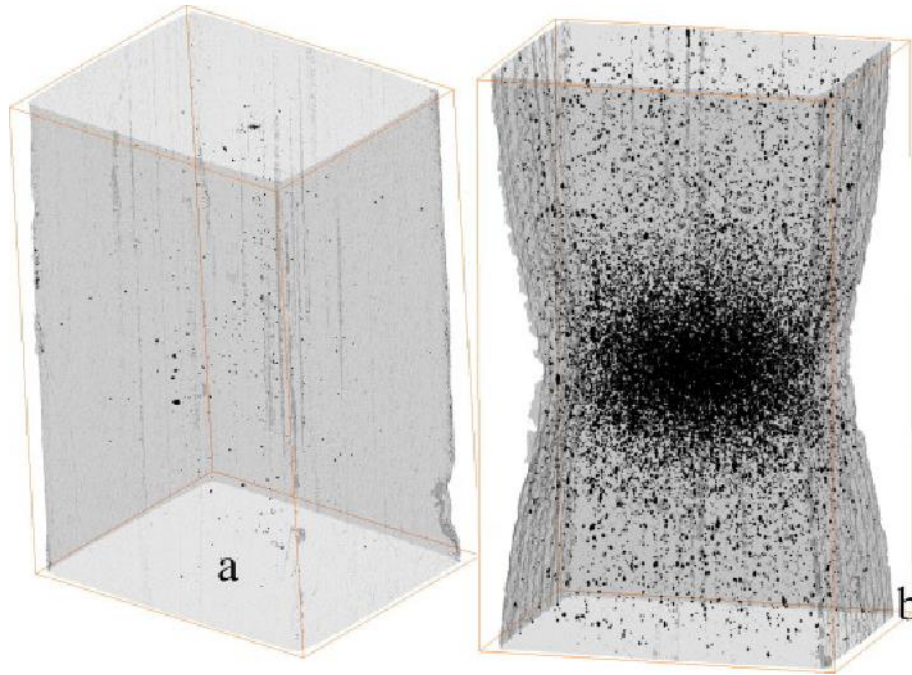


Figure 6.4: 3D representation of the population of cavities inside the deforming sample in (a) its initial state and (b) just before fracture [118].

Further details of these kinds of experimental measurements can be found in the literatures [116-119]. Although via direct methods, the accuracy of the GTN model parameters can be guaranteed, the limitations of this method, such as the experiment costs, test equipment and data analysis techniques, are also pretty significant for common researchers. Therefore, other experimental and numerical methods are proposed to calibrate the GTN and MMC fracture criteria in the following sections.

### **6.2.2 Fracture tests and inverse calibration**

As discussed in previous section, the direct methods, such as X-ray tomography technique, can be utilized to identify the GTN model parameters. However, for most fracture criteria, calibration through direct methods is a challenging task. Hence, inverse approaches based on experimental and numerical methods are proposed and

developed to identify the fracture model parameters. In these inverse analysis approaches, a specific number of fracture tests should be performed to provide necessary information. This section will focus on describing various types of fracture tests and specimens.

In the work of Dunand *et al.* [104, 114], a basic ductile fracture testing program has been implemented on specimens extracted from TRIP steel sheets with various geometries, which include smooth tensile specimens, tensile specimens with central holes and circular notches and butterfly specimens for bi-axial experiments. And, experimental measurements of the corresponding fracture tests have been utilized to identify the material parameters of MMC model and a shear modified Gurson model.

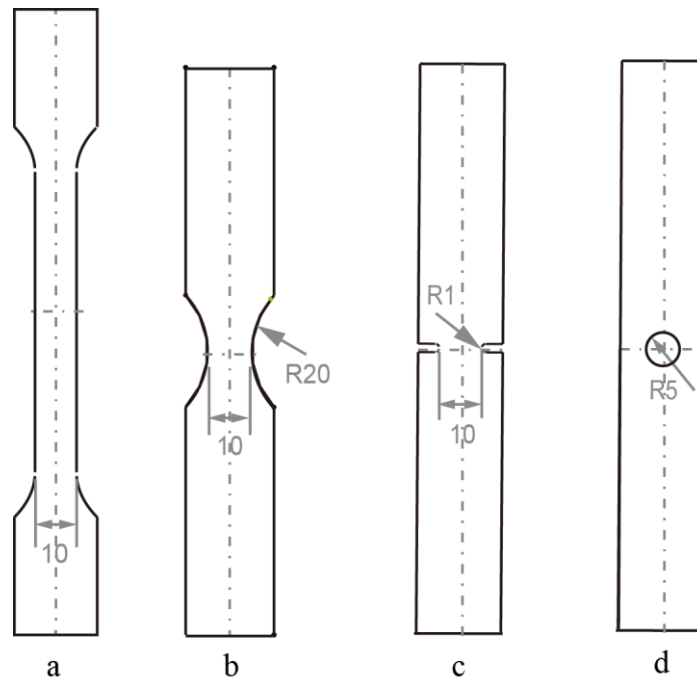


Figure 6.5: Illustrative examples of (a) smooth, notched tensile specimens with a circular cutout of (b) 20 mm and (c) 1 mm, and (d) tensile specimen with a central hole.

Illustrative examples of smooth and notched tensile specimens and tensile specimen with central hole are shown in Fig. 6.5. Tensile can be performed on these flat specimens with tensile test machine under displacement control at a constant crosshead velocity. The loading force on the tensile specimen can be recorded by the holders of the test machine. In addition, Digital Image Correlation (DIC) is used to

measure the relative displacement of specimen boundaries and the displacement field at the center of the gage section that is fixed on the specimen. If the equipment condition is limited, we can also use the extensometer to record the relative displacement. In the measured force-displacement curves, a force peak is reached before fracture occurs. It is associated with the onset of through-the-thickness necking. And, the first discontinuity or drop in the measured displacement field or loading history is defined as the instant of the onset of fracture. The corresponding relative displacement of the specimen boundaries is considered as the displacement to fracture or fracture displacement. Correspondingly, the analytic values of stress state are also given in Table 6.1. And, the fracture strain ( $\varepsilon_f$ ) is calculated using the following approximation:

$$\varepsilon_f = \ln \left( \frac{A_0}{A_f} \right) \quad (6.16)$$

where  $A_0$  and  $A_f$  are initial and fracture cross section areas of a specimen, respectively.

Additionally, bi-axial fracture tests are performed using a dual actuator system [120], which permits to apply a combination of normal and transverse loads to the boundaries of a butterfly-shaped specimen, as shown in Fig. 6.6a. The schematic illustration of the dual actuator testing system and bi-axial loading mechanism are also depicted in Fig. 6.6b. Due to the specimen geometry, the occurrence of fracture initiates at the center of the gage section, which is bounded by the shoulders of clothoid shape. Moreover, the fracture is remote from the lateral free edges. The ratio of the applied vertical load  $F_V$  and the horizontal load  $F_H$  is expressed by the bi-axial loading angle  $\beta$ :

$$\tan \beta = \frac{F_V}{F_H} \quad (6.17)$$

In the case of  $\beta = 0^\circ$  where only the horizontal load  $F_H$  is applied on the butterfly specimen, it corresponds to pure shear. While, in the case of  $\beta = 90^\circ$  where only the vertical load exists, the specimen is subjected to the transverse plane strain tension.



By varying the magnitude of the horizontal and vertical load, different loading conditions or stress states are investigated, such as  $\beta = 0^\circ$  (pure shear),  $\beta = 25^\circ$  (shear-dominated),  $\beta = 63^\circ$  (tension-dominated) and  $\beta = 90^\circ$  (transverse plane strain tension). All the bi-axial fracture experiments need to be performed under force or displacement control to enforce a constant loading angle. Displacements of the specimen boundaries or displacement field of the whole gage section are recorded by extensometer or DIC technique during the experiments. Moreover, the analytical stress states are also given in Table 6.1.

Table 6.1: Five types of classical specimens for plasticity and fracture calibration and corresponding analytical values of stress states.

No.	Specimen type	Stress triaxiality $\eta$	Normalized Lode angle parameter $\bar{\theta}$
1	Smooth dog-bone specimen	$\frac{1}{3}$	1
2	Notched tensile specimen	0.4-0.55	0.4-0.6
3	Tensile specimen with central hole	0.3	0.9-1
4	Butterfly specimen	0-0.6	0-0.5
5	Equibiaxial tensile specimen	$\frac{2}{3}$	-1

With the experimental measurements of aforementioned fracture testing program, the model parameters of the MMC and GTN models can be identified through inverse calibration [114].

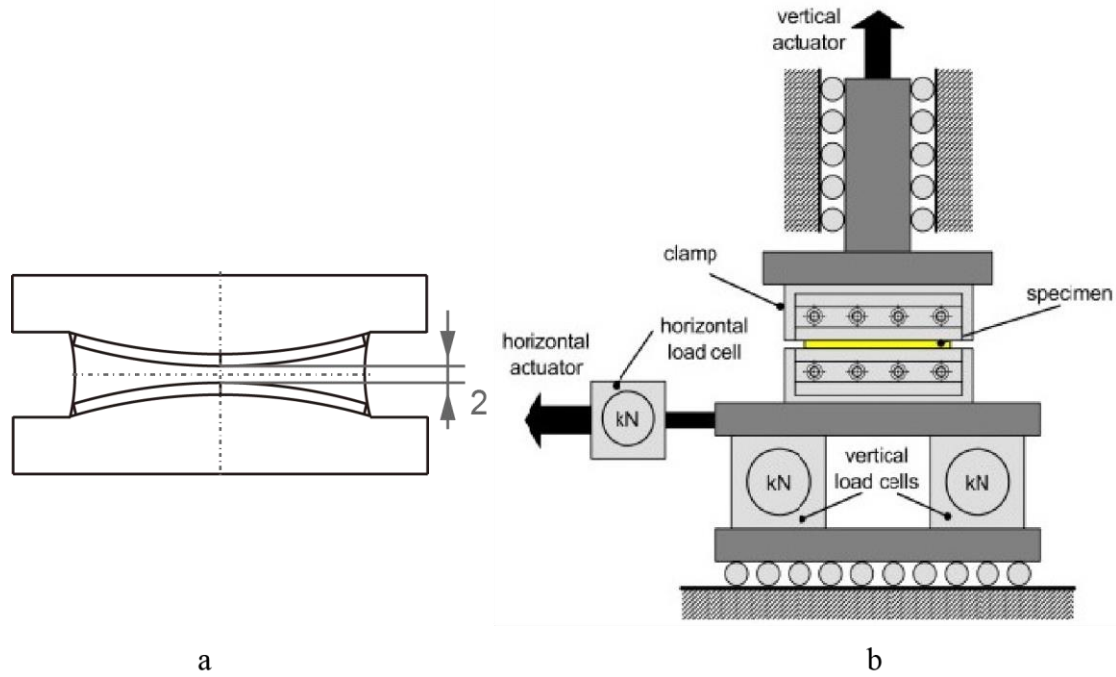


Figure 6.6: (a) Butterfly specimen for bi-axial experiments and (b) schematic of the dual actuator testing system [120].

In each experiment, two load-displacement curves: the tangential force versus horizontal displacement curve and the axial load versus vertical displacement curve, need to be measured. In experiments related to tension-dominated loading condition, the vertical load-displacement curves exhibit a peak prior to fracture, which can be considered as the onset of localized necking. In the shear-dominated experiments, the measured curves increase monotonically until fracture. The fracture displacement is defined as the relative (either horizontal or vertical) displacement of the specimen boundaries at which a sudden drop of force appears.

In the work of Eller *et al.* [121], an Erichsen-like test with hemispherical punch and die radius was performed to obtain a state of equibiaxial tension in three sets of boron steel sheets. The specimen geometry and schematic illustration of the loading mechanism are depicted in Fig. 6.7a and b, respectively. The experiment is carried out on a screw-driven universal testing machine under quasi-static loading condition. In order to reduce the effects of friction between punch and specimen, a lubrication or tribological system was put between them. The out-of-plane displacement of the specimen was measured with extensometer or DIC technique. The displacement is defined as the relative vertical displacement between punch and specimen clamp.

The applied force versus punch displacement curve increases monotonically until a drop in the force level at the instant of the onset of fracture.

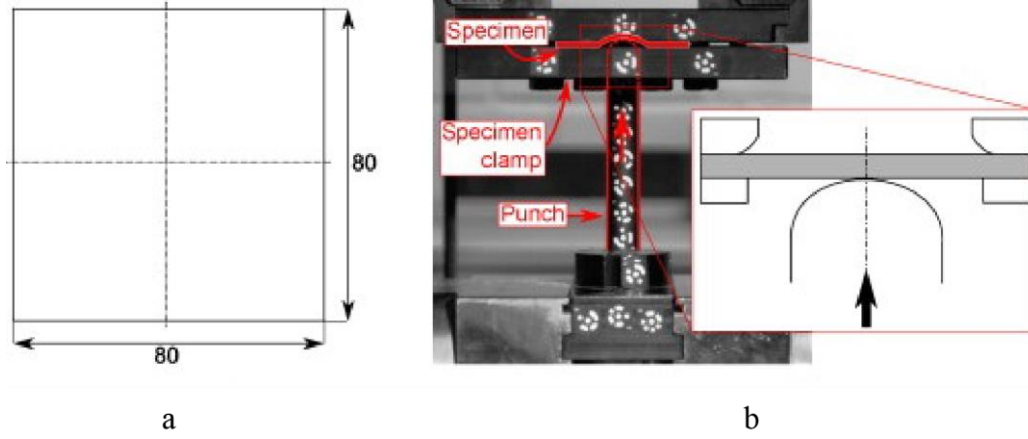


Figure 6.7: (a) Equibiaxial tension specimen geometry and (b) schematic illustration the loading process [121].

As previously presented, the stress state can be characterized in the space  $(\eta, \bar{\theta})$ . Various stress states encountered in classical specimens used for fracture testing can be uniquely characterized by the above-mentioned set of parameters  $(\eta, \bar{\theta})$ , as listed in Table 6.1. And, the analytical values of the stress triaxiality  $\eta$ , the normalized Lode parameter  $\bar{\theta}$  in terms of measurable quantities are all listed in Table 6.1.

For the MMC model, three butterfly fracture experiments with loading angle  $\beta$  of  $0^\circ$ ,  $63^\circ$  and  $90^\circ$  and the equibiaxial tensile test, which cover a wide range of positive stress triaxialities and the complete range of normalized Lode angle parameter, are enough to calibrate the four parameters of the MMC model. The calibration objective is to find a set of parameters  $(c_1, c_2, c_3, c_\theta)$  that make the model describe the onset of fracture correctly. Therefore, an objective function of least square error (*LSE*.) was proposed by Dunand *et al.* [114]; by minimizing it, a set of optimal parameters can be achieved:

$$LSE. = \frac{1}{N} \sum_N \left( \left[ D(\bar{\epsilon}_f) \right]_{exp} - 1 \right)^2 = \frac{1}{N} \sum_N \left( \left[ \int_0^{\bar{\epsilon}_p} \frac{d\bar{\epsilon}_p}{\bar{\epsilon}_f(\eta, \bar{\theta})} \right]_{exp} - 1 \right)^2 \quad (6.18)$$

where  $N$  is the number of calibration tests.  $\eta(t)$ ,  $\bar{\theta}(t)$  and  $\bar{\epsilon}_p(t)$  are the loading histories for the critical element where fracture is assumed to initiate. In the literatures, optimal parameters were obtained, confirming that the MMC criterion

has the capability to perfectly fit the results of all calibration experiments. Furthermore, the simplified version of MMC model, MMC3 model was calibrated by imposing the parameter  $c_\theta = 1$ .

For the GTN model, parameters are determined using four kinds of fracture experiments: (i) uniaxial tension, (ii) notched tension, (iii) equibiaxial experiment and (iv) pure shear experiment. An inverse method based on Monte Carlo Sampling was proposed to identify these model parameters. Further details of the calibration process can be found in the literatures [104,114].

### 6.3. Combination of damage and micromechanics

As presented previously, micromechanical modelling and ductile fracture criteria of DP steel have been discussed. At macro level, the damage, like the plasticity, is supposed to be isotropic and homogeneous. The RVE model of DP steel includes two different phases: ferritic matrix and martensitic inclusion [133,134]. Each constituent phase has its own damage variables (void volume fraction in GTN model, damage indicator in MMC model, etc.).

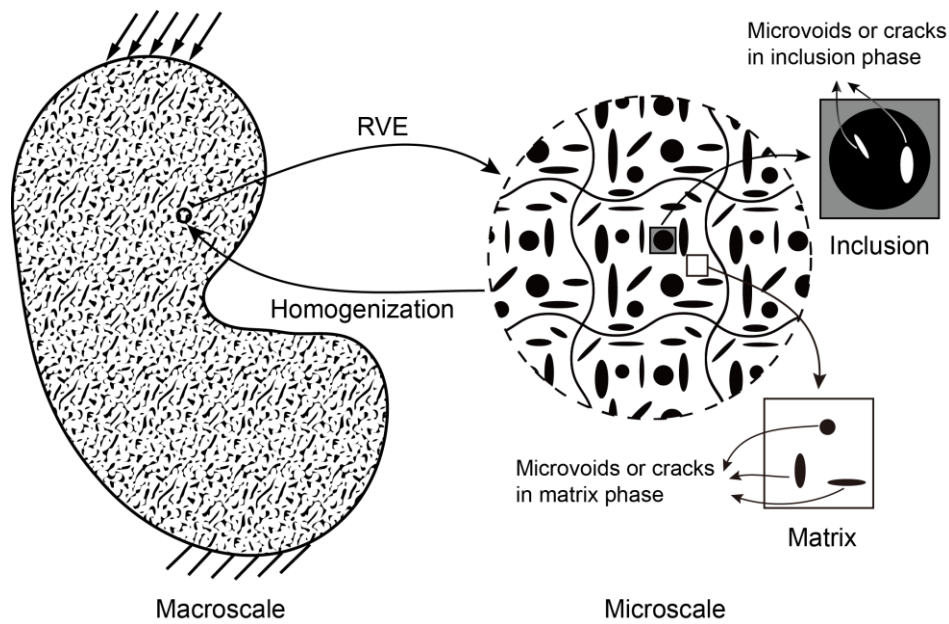


Figure 6.8: Schematic illustration of damage homogenization using RVE.

The homogenized damage variables are hence computed and deduced from the phase fraction, as formulated in Eq. (6.19):

$$\bar{D} = D_F P_F + D_M P_M = D_F (1 - P_M) + D_M P_M \quad (6.19)$$

where  $D_F$  and  $D_M$  denote damage variables in ferrite and martensite,  $P_F$  and  $P_M$  are phase fraction of ferrite and martensite phases. Fig. 6.8 shows a schematic illustration of the damage homogenization procedure. From this figure, proper fracture criterion is introduced in each single phase. And, corresponding material parameters of different phase are calibrated and identified according to the fracture test plans. Therefore, by combining the damage and micromechanics, the damage homogenization can be performed. However, this procedure needs a complex fracture test plan, which consists of several specimens of different materials (matrix and inclusion materials). This will cost numerous experimental works to prepare the specimen, to implement the test and to handle the measurements. In this work, due to the limitation of experiment condition, I have proposed a numerical method to calibrate the material parameters of fracture criterion for specific DP steel. And, a complex fracture testing plan has been proposed to perform on specimens of various DP steels and pure phase (pure martensite or ferrite) steels. By this way, the material parameters of fracture model for each phase can be identify and used to compute the homogenized fracture behaviors. But now, this project is still in progress. Therefore, the implementation of the damage homogenization will be carried on in future work.

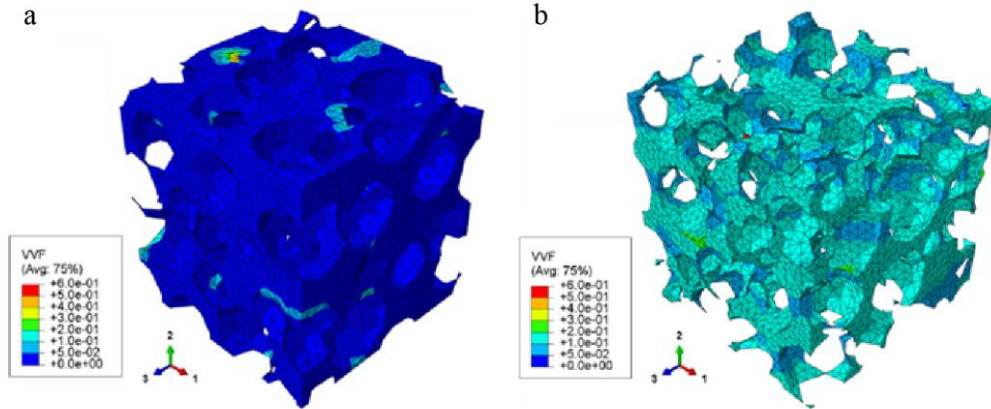


Figure 6.9: Total void volume fraction in matrix phase under uniaxial tensile load at strain level  $\varepsilon = 0.014$ : RVEs with (a) 60% and (b) 80% inclusion phase [134].

An example of the combination of damage and micromechanics is given in Fig. 6.9. In this example, two 3D RVEs are artificially generated using spherical geometry as inclusion phase with fraction of: (a) 60% and (b) 80% [134]. GTN fracture model and identified material parameters are applied in the matrix phase. And, uniaxial

tensile load is imposed on the RVE model. These contours show the total void distribution, which is considered as the damage variable, in the matrix phase at the same strain level  $\varepsilon = 0.014$ . From the observation, there are relatively higher void volume fractions along the interface between different phases. This can confirm the conclusion that we get in Part I. That is, due to the appearance of shear bands along the same interface, as the plastic flow accumulating, shear dominant failure mode continues and leads to final failure of the RVE model.

Additionally, the implementation of this homogenization method needs to identify the fracture model parameters of materials with pure ferrite and martensite. In our work, the specimens with pure ferrite and martensite have been machined by ESI-Group. And, corresponding experiments will be performed to record the load-displacement history. In near future, when the whole fracture test plan has been done, material parameters of the selected fracture criterion can be identified using a calibration process based on bi-level reduced surrogate model. This calibration process will be presented in next chapter.

## **Chapter 7**

### **Calibration process based on bi-level reduced surrogate model**

Recently, numerous experimental investigations [94,104,114,121-125] have been performed to characterize and identify the material parameters of MMC criterion for various ductile metals. Typically, massive quantities of fracture tests need to be performed during the experimental works. This costs enormous amount of time and expenses to prepare specimens and analyze experimental data. Therefore, it particular emphasizes the needs for further improvement in this technique to simplify the identification process.

For aforementioned reasons, a surrogate model [126-129] is employed as a computationally inexpensive alternative to calibrate the MMC fracture criterion in this work. The surrogate model utilizes an approximation based on the results computed at various points in a design space to replace a complex one. The approximation obtained from the surrogate model does not represent the low fidelity versions of computational models derived by simplifying the physics of underlying phenomena. Instead, the surrogate-model based approximation aims to reconstruct the input-output relationship by numerical simulations [107,128]. The application of the surrogate model in this identification process significantly reduces the number of required fracture tests. The diffuse approximation [53,54,63,105,106] is widely used to construct surrogate models. The specialized properties highlight its effectiveness in a range of computational mechanics application varying from structural optimization to surface interpolation for identification of material parameters. A surrogate model based on the diffuse approximation is proposed in the current work to empirically capture the non-linear evolution of material parameters on the fracture onset under uniaxial loading condition. Therefore, the objective is to develop a computationally affordable but accurate model, which utilizes a small set of training data obtained from bi-level models: local critical elements and global 3D finite element (FE) fracture models, to identify the material parameters of MMC criterion for a given DP steel. In the proposed method, the surrogate model is used as an

approximation tool associated with the design of experiments (DOE) [64,107] approach, given current fracture onset displacement and strain.

## 7.1. Experimental work

### 7.1.1 Material description

In this work, fracture testing specimens are cut from 1.6 mm thickness cold rolled DP590 steel sheets. The loading axis of each specimen is always located along the rolling direction. Fig. 3.1 gives the micrograph of DP590 steel using Quanta FEG 250 scanning electron microscope (SEM), which shows an obvious ferritic/martensitic microstructure.

### 7.1.2 Specimen and experimental procedure

Initial fracture calibrations are performed using tensile tests on a smooth and two notched flat specimens with different notch radius of  $R = 20$  mm and  $R = 1$  mm, as shown in Fig. 7.1.

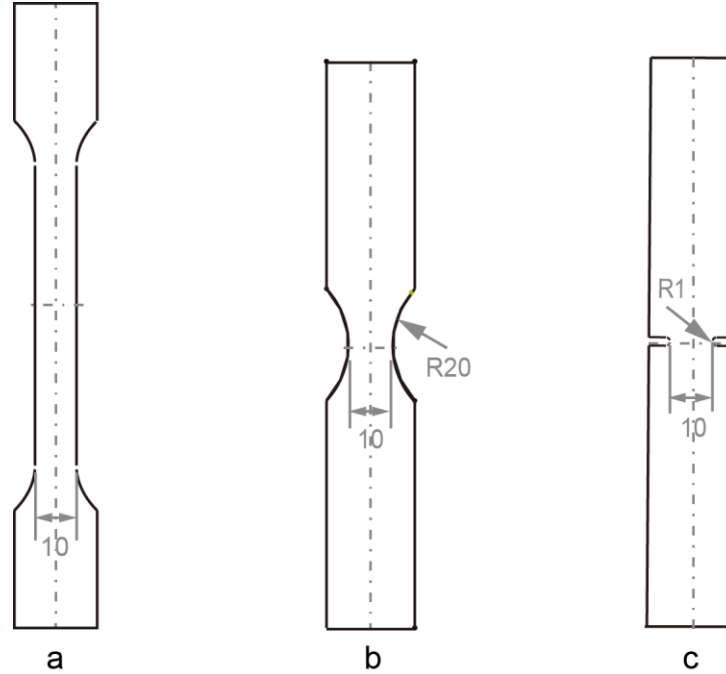


Figure 7.1: Geometry of smooth (a) and notched tensile specimens with notch of  $R = 20$  mm and  $R = 1$  mm.



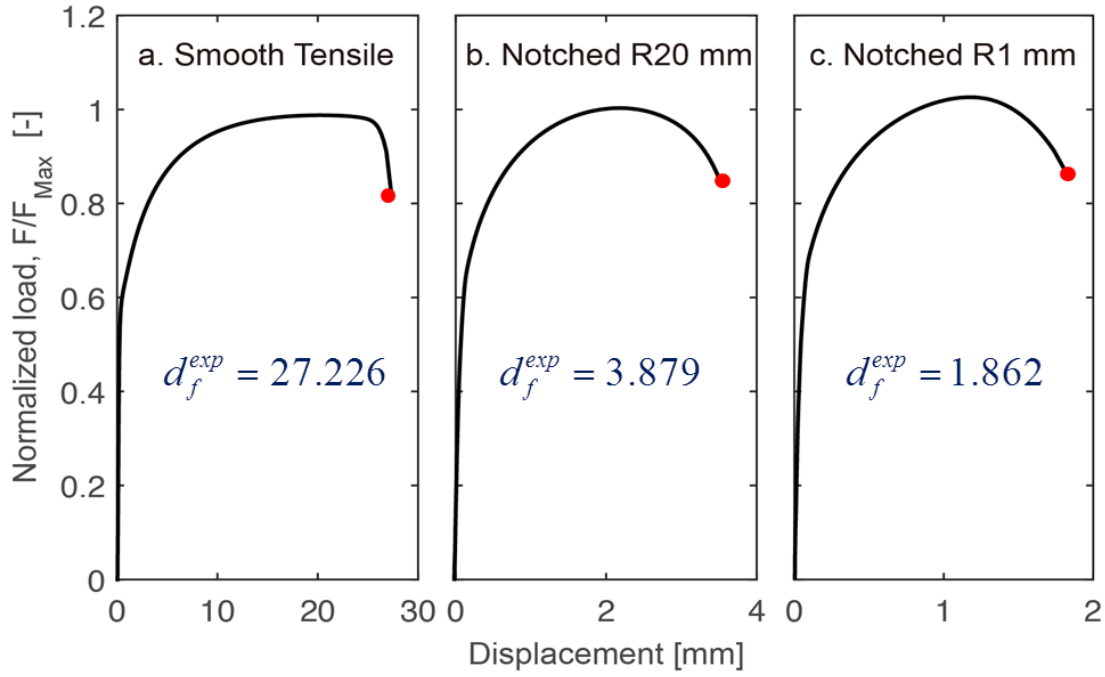


Figure 7.2: Measured load-displacement curves and average fracture onset displacements for (a) smooth, notched tensile specimens with (b) 20 mm and (c) 1mm open cutouts.

The smooth specimen has a 100 mm gauge length and a 10 mm gauge width. Similarly, the  $R = 20$  mm and  $R = 1$ mm notched specimens have the same gauge width of 10 mm and different gauge length of 40 mm and 20 mm, respectively. Experiments are carried out using Zwick Z020 tensile test machine at room temperature, with a quasi-static displacement rate of 2 mm/min. The measurements are depicted in Fig. 7.2. For all specimens, a maximum force is reached before fracture.

The onset of fracture is defined by the first discontinuity in the normalized load-displacement curves. The appearance of the first crack corresponds to the sudden drop of the applied axial force in those tests. The corresponding relative displacement between the test region boundaries is referred as fracture displacement. Three specimens of each geometry are tested to ensure the reproducibility of the results. The variations in the measured fracture displacement are around 2.5% for smooth specimen, and less than 1.5% for each notched specimens. And, the initial input fracture strain ( $\varepsilon_f$ ) is computed as in Eq. (6.16).

### 7.1.3 Strain hardening parameters fitting

The elasto-plastic behavior of DP590 steel is predicted in Part I, which can be described by the J2 plasticity theory, in which a classical Swift power law is utilized to describe the flow stress up to the plastic localization occurrence:

$$\sigma = K(\varepsilon_0 + \varepsilon_p)^n \quad (7.1)$$

where  $\sigma$  is true stress, and  $\varepsilon_p$  is plastic strain.  $K$ ,  $\varepsilon_0$  and  $n$  are material constants to be fitted. Using the flow curve (Fig. 7.3) corresponding to the smooth specimen, the best fit is obtained with the set of parameters reported in Table 7.1.

Table 7.1: Strain hardening parameters.

$K(\text{MPa})$	$\varepsilon_0$	$n$
1080	0.0032	0.21

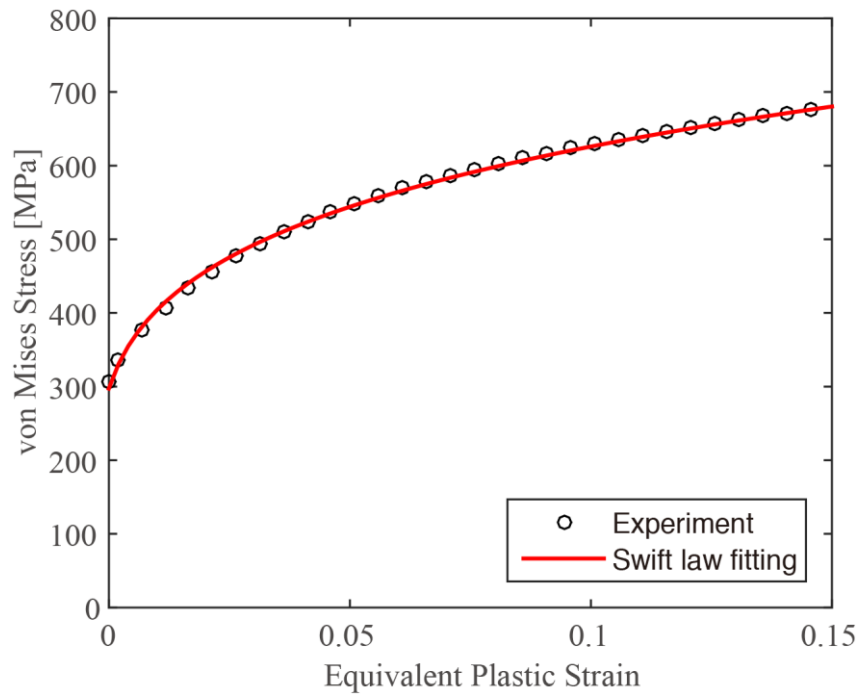


Figure 7.3: Measured and Swift law fitting flow stress of DP590 steel.

The solid line in Fig. 7.3 presents the identified flow stress, and the circles represent the measurements. Since no obvious discrepancy is found in the comparison, Swift

law is utilized along with the von Mises yield criterion to describe the plastic behavior of the investigated DP590 steel.

## **7.2. Surrogate model**

Generally, when an output of interest cannot be easily obtained using direct approaches, such as experimental measurements, a surrogate model [107] can be used as an alternate method to estimate the input-output relation and predict the output. Especially, in most engineering design problems, the design objective and constraint functions usually require experiments or simulations to build their formulations based on design variables. In fact, enormous amount of work, time and computation cost are really necessary to perform these experiments or simulations, which makes it relatively difficult to complete this work. However, with the application of surrogate model, including response surface methodology, diffuse approximation etc., it can significantly simplify the problems by constructing approximation models. Here, surrogate model can not only mimic the behavior of the simulation as closely as possible, but also be computationally cheaper to evaluate.

In addition, Data-driven, bottom-up approaches, in which a limited number of sampled data is obtained via DOE, can be used to construct surrogate model. In these approaches, the input-output relation is pretty important, and we can even ignore the inner mechanism of the simulation method. Only response or output of these sampled data is obtained from the simulator. After that, relationship between input and output is usually approximated with several numerical methods, e.g. polynomial function interpolation, genetic algorithms. By this way, surrogate model can provide prediction efficiently and rapidly.

Concerning the numerical properties of surrogate model, it has been wildly used in various fields of engineering design, which can avoid expensive experiments or simulations.

### ***7.2.1 Response surface methodology***

In statistics, response surface methodology (RSM) [107,127] can be used to investigate the input-output relation between several design and response variables. RSM is a popular method to build surrogate model, which uses a sequence of

designed experiments to calculate and obtain an optimal response. When treatments are from a continuous range of values then the true relationship between the dependent variable  $y$  and independent variables  $x$  might remain unknown. The approximation of the response function  $y = f(x_1, x_2, \dots, x_n) + e$  is called response surface methodology.

In general, the response surface  $f$  can be described using low-order polynomial models. Once it is supposed that only significant explanatory variables are left, then a more complicated design can be implemented to estimate a polynomial interpolation, which is still only an approximation but with the minimum discrepancy. But, the polynomial model can be used to optimize a response, such as maximize, minimize or attain a specific target.

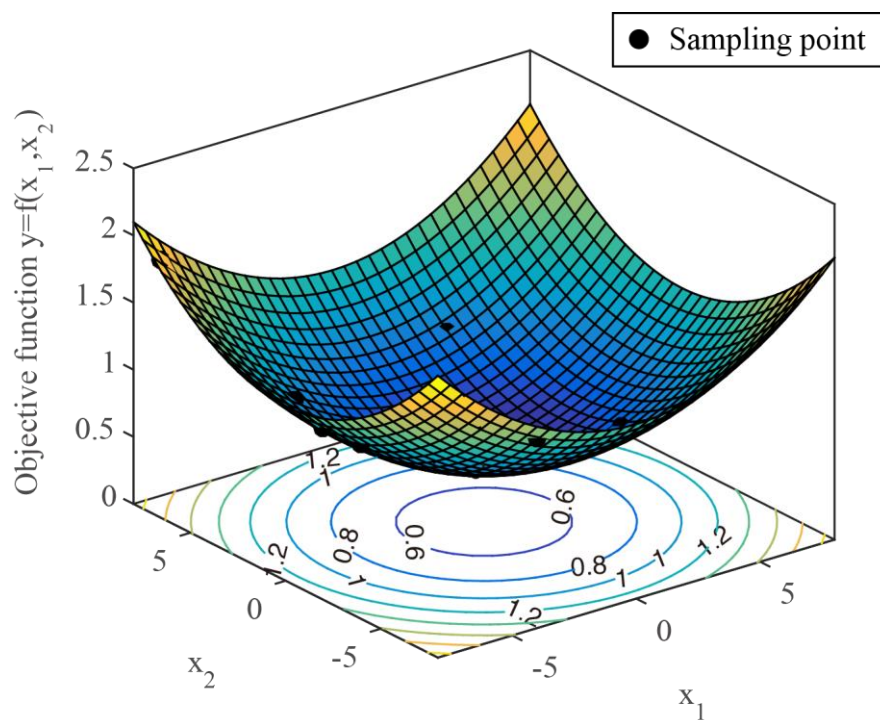


Figure 7.4: Illustrative example of an objective function with two independent variables  $y = f(x_1, x_2)$ : designed experiments (black dots), response surface (fitting surface in color) with second-degree polynomial.

An ordinary example of the application of RSM is to estimate a second-degree polynomial model  $f$  using a factorial experiment or a fractional factorial design. It is sufficient to determine which explanatory variables have an influence on the response variables of interest. As shown in Fig. 7.4, an objective function with two independent variables  $y = f(x_1, x_2)$  is proposed as the target to be approximated. A

specified account of sampling experiments (black dots in Fig. 7.4) is designed to estimate the relationship between these two independent variables and the objective function. Actually, these sampling experiments are from a design of experiments (DOE), which aims to describe or explain the variation of information under conditions that are assumed to reflect the variation. Based on the design of experiments, a second-degree response surface can be constructed as the relevant surrogate model. Moreover, by minimizing the objective function, an optimal solution is reached to achieve the engineering goal.

Recently, the RSM method has been widely used to obtain the optimum material parameters of fracture criterion. In order to achieve this goal, the range in which each variable can be varied was obtained from literatures. Then, based on the experiment design methods, combinations of tensile test simulation were used to construct the corresponding response surface between the experimental load-displacement curve and the simulated one. Further details referred to this method to identify material parameter of GTN model can be found in the literatures [130,131].

### **7.2.2 Diffuse approximation**

As presented in previous section, RSM is a method for replacing a complex model by an approximate one based on results calculated at various points in the design space. The diffuse approximation, also known as moving least squares (MLS) approximation, is a method of reconstructing continuous functions from a set of random point samples via the calculation of a weighted least squares measure biased towards the region around the point at which the reconstructed value is requested [105-107]. The concept of diffuse approximation was first proposed by Nayroles [106] in the early 1990s.

The basic idea of the diffuse approximation is to replace the FEM interpolation by introducing a local weighted least squares fitting in a small neighborhood of a point and based on  $n$ -th nodes close to this point on an element. Later, an approach named diffuse element (DEM) was developed based on this idea.

In this method, a function  $f$  and a set of sampling points  $S = \{(x_i, f_i) \mid f(x_i) = f_i\}$ , where  $x_i$  and  $f_i$  are real numbers. As presented in Section 7.2.1, these sampling points can be designed using different DOE techniques. Then, the diffuse

approximation of  $f$  at the point  $x$  is  $\tilde{f}(x)$ , where  $\tilde{p}$  minimize the weighted least square error over all polynomials  $f$ :

$$\sum_{i \in I} \theta(\|x - x_i\|) (\tilde{f}(x_i) - f_i)^2 \quad (7.2)$$

Here,  $\theta$  is the weighting function and it tends to zero as  $d \rightarrow \infty$ .

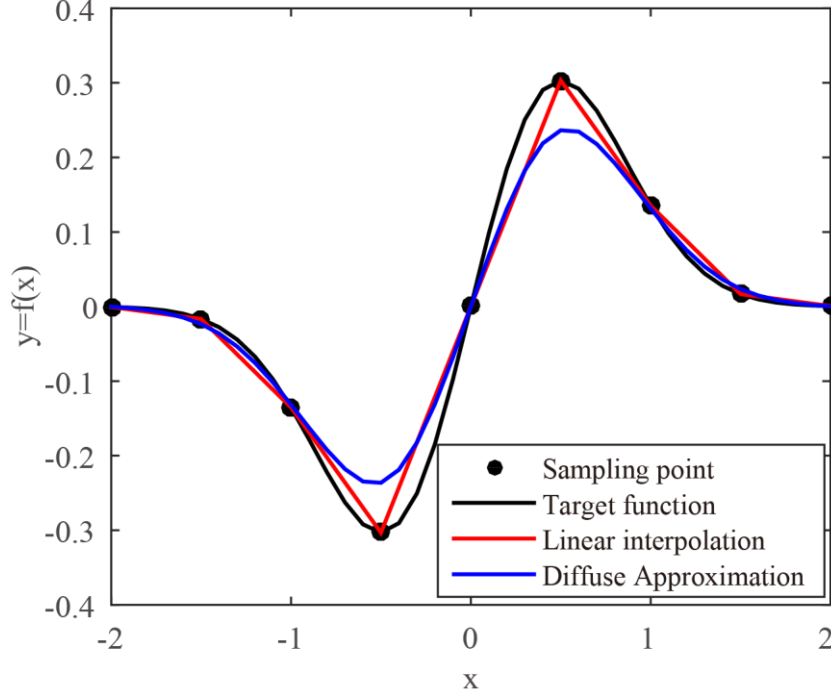


Figure 7.5: Illustrative example of diffuse approximation. Black dots: sampling points, black curve: target function to be approximated, red curve: linear interpolation, and blue one: diffuse approximation of third degree.

An illustrative example is given in Fig. 7.5, where the black dots represent the sampling points from DOE, the black curve denotes the target function, the red and blue curves denote the linear interpolation and diffuse approximation of third degree, which are obtained based on these sampling points. In this example, the weighting function is  $\theta(d) = \exp(-d^2)$ . Here, a quadratic interpolator is utilized as the smooth interpolator to approximate the target function.

### 7.3. Bi-level modelling reduction strategy

As presented in Section 6.1, the original MMC fracture criterion is simplified to a MMC3 criterion using the Eq. (6.9) and (6.10). In order to calibrate and identify

those three unknown parameters ( $c_1, c_2, c_3$ ), a bi-level reduced surrogate model is developed based on the combination of DOE and diffuse approximation approaches. Therefore, this section focuses on the bi-level modelling reduction strategy used to construct the surrogate model.

### ***7.3.1 Global finite element model***

For calibrating the MMC3 criterion, numerical simulations are initially performed on the three fracture specimens described in Section 7.1.2 combined with the strain hardening parameters given in Table 7.1. These preliminary simulations do not include fracture. All specimens are meshed with eight-node 3D solid, reduced integration elements (C3D8R in Abaqus/Explicit [132]). Although the specimen geometries are symmetrical, the initiation of fracture and resulted fracture surfaces do not show the same property. Therefore, whole specimens are considered in the global FE models to investigate the fracture behavior, as shown in Fig. 7.6a.

### ***7.3.2 Local critical element***

Meanwhile, in order to reduce the computational time, a local critical element, in which initiation of fracture occurs, is selected according to the strain localization level, as shown in Fig. 7.6b. From both simulation and experimental observations, it is identified that the local critical elements of the smooth and 20 mm notched tensile specimens are always located at the center of the longitudinal cross-section, while the third specimen reveals that the critical elements are located along the edge of the open notch, as shown in Fig. 7.6. The main reason of this phenomenon indicates that, stress concentration is caused by the geometric irregularity at the vicinity of the 1 mm radius notch.

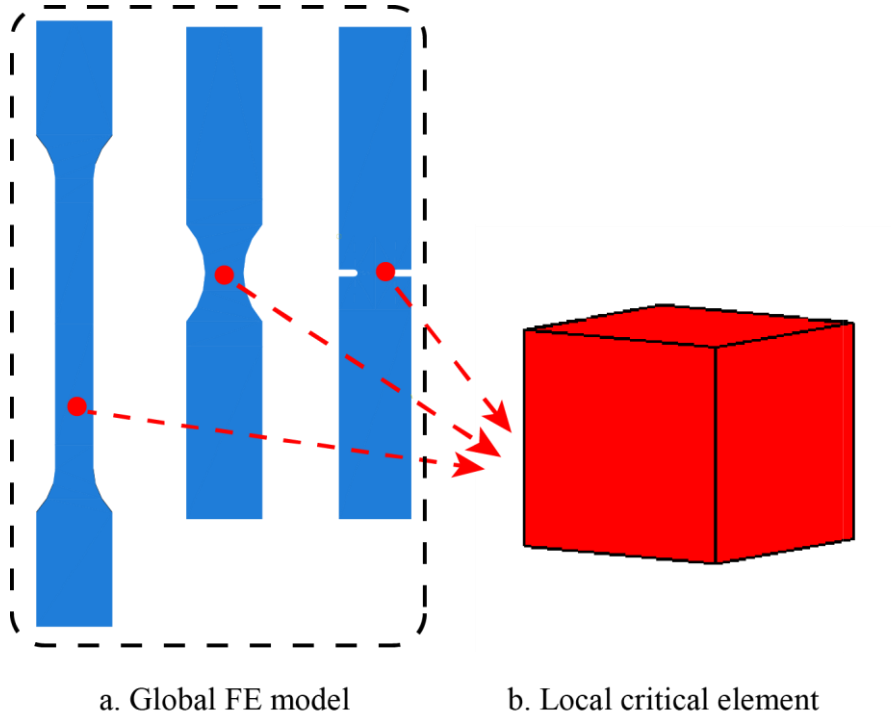


Figure 7.6: Illustration of the bi-level reduced strategy: (a) global FE model and (b) local critical element model.

The histories of the stress triaxiality, normalized Lode angle parameter and equivalent plastic strain in the local element are recorded as with time and plotted in Fig. 7.7a. The values of  $\eta$ ,  $\bar{\theta}$  and  $\bar{\varepsilon}_p$  are also projected on the different individual planes, as shown in Fig. 7.7b-d.



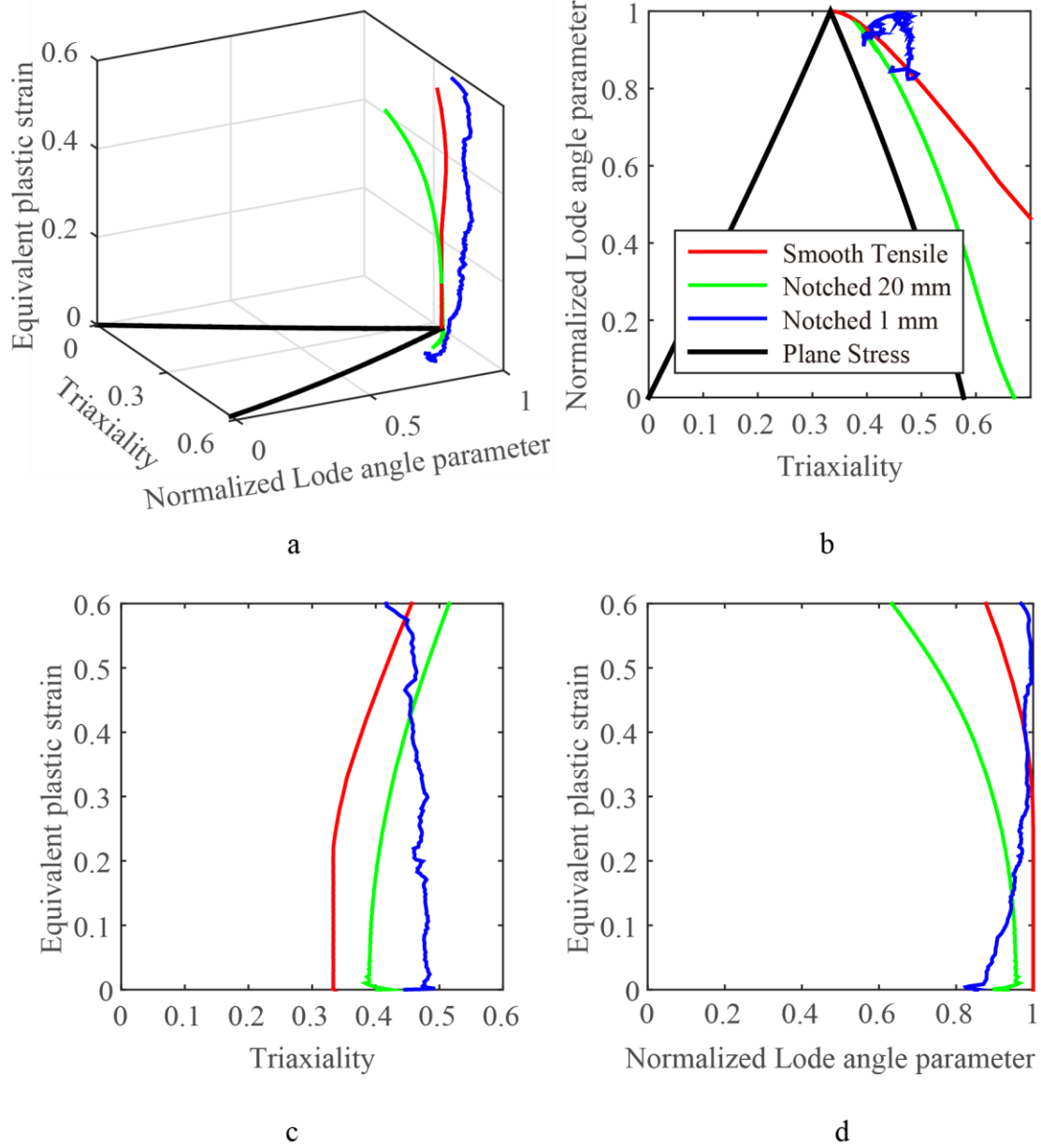


Figure 7.7: Plane stress condition and stress state histories of the local critical element obtained for each tensile specimen without fracture modeling in: (a),  $(\eta, \bar{\theta}, \bar{\varepsilon}_p)$  space, (b),  $(\eta, \bar{\theta})$  plane, (c),  $(\eta, \bar{\varepsilon}_p)$  plane and (d),  $(\bar{\theta}, \bar{\varepsilon}_p)$  plane.

It can be obviously found that the curves of smooth and 20 mm notched tensile specimens closely resemble with the analytical solutions obtained for the plane stress condition (the black line in Fig. 7.7a and b). However, in the case of 1 mm notched tensile specimen, those curves are significantly different from other two cases. This is mainly because that, the corresponding local critical element is not located in the center of specimen's longitudinal cross-section. As those specimens

undergo necking stage, the stress states significantly deviates from the analytical solution.

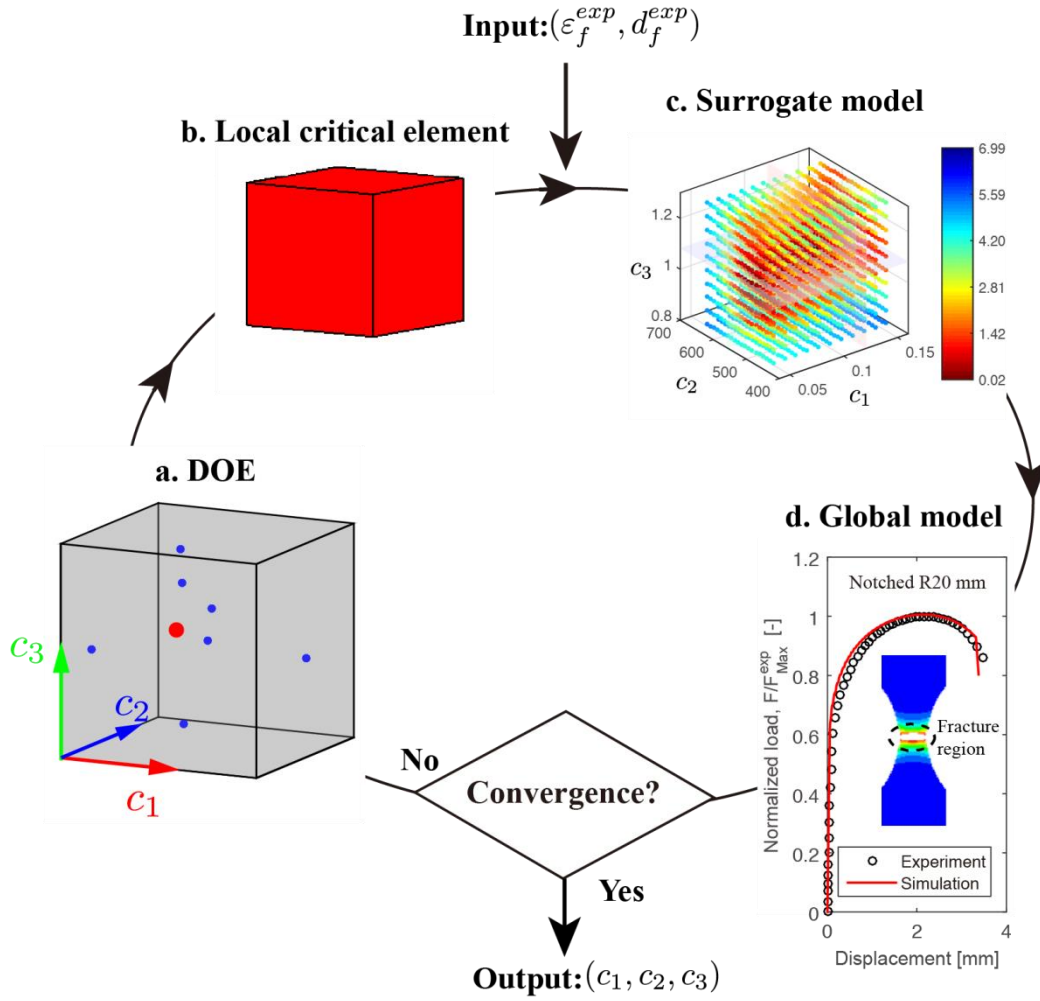


Figure 7.8: Flowchart of the Bi-level modelling reduction strategy.

Based on the stress states paths training experimental points of unknown parameters  $(c_1, c_2, c_3)$  in DOE can be calculated within the local critical element. The corresponding surrogate model is constructed according to diffuse approximation. Fig. 7.8 gives a schematic illustration of the bi-level modelling reduction strategy. In summary, the strategy consists of following steps:

- i. Initial material parameters  $(c_1^0, c_2^0, c_3^0)$  are considered as the center (red dots in

Fig. 7.8a) to create the DOE for the first iteration. Fracture onset strains of each training experimental points (blue dots in Fig. 7.8a) are calculated based on the stress states of the local critical elements (Fig. 7.8b) using Eq. (6.9);

- ii. Fracture strain prediction for the DOE space is approximated using diffuse approximation. A surrogate model (Fig. 7.8c) of the least square error ( $LSE.$ ) between the approximated and measured fracture strain is constructed to identify the material parameters. Identified parameters of each iteration are determined from the surrogate model by:

$$\text{Argmin } LSE. = \frac{1}{m} \sum_{i=1}^m \left( \tilde{\varepsilon}_{f_i}(\mathbf{c}) - \varepsilon_{f_i}^{exp} \right)^2 \quad (7.3)$$

where  $\tilde{\varepsilon}_{f_i}(\mathbf{c})$  is the approximated fracture strain at the point  $\mathbf{c}$ ,  $\varepsilon_{f_i}^{exp}$  is the measured fracture strain, and  $m$  is the number of specimen with different geometries;

- iii. The obtained parameters are then introduced within the global model (Fig. 7.8d) to compute the corresponding  $LSE.$  of the fracture onset displacement:

$$LSE. = \frac{1}{m} \sum_{i=1}^m \left( d_{f_i} - d_{f_i}^{exp} \right)^2 \quad (7.4)$$

where  $d_{f_i}$  and  $d_{f_i}^{exp}$  are the predicted and measured fracture onset displacements, respectively. The DOE of next iteration is designed by shifting the center to the center of the identified parameters and halving the DOE variation;

- iv. Converged material parameters are identified until the variation of DOE space and  $LSE.$  of the fracture onset displacement (in Eq. (7.4)) reach sufficiently acceptable ranges.

The proposed bi-level modelling reduction strategy can guarantee not only the accuracy of identification process with the limited number of experimental tests, but also significantly reduce the computational time. Further details of the aforementioned approaches and methods are given in the following sections.

### 7.3.3 Adaptive correlation between fracture onset displacement and strain

In our experimental test plan, as no DIC technique is used to capture the simultaneous strain when damage initially appears in critical elements, an adaptive deviation of fracture onset displacement is proposed as:

$$\Delta d_{f_i} = d_{f_i} - d_{f_i}^{exp} \quad (7.5)$$

And, the new fracture strain is given as:

$$\left(\varepsilon_{f_i}^{exp}\right)_{new} = \left(\varepsilon_{f_i}^{exp}\right)_{old} + \ln\left(1 + \frac{\Delta d_{f_i}}{L_{0i}}\right) \quad (7.6)$$

where  $d_{f_i}$  is the fracture onset displacement obtained from the global model of the simulation, and  $L_{0i}$  is the initial effective length of each specimen's test region. This adaptive correlation is utilized to ensure that our experimental target varies around the exact value with a decreasing error that eventually becomes negligible.

#### 7.4. Diffuse approximation of fracture strain prediction

By following the procedure given in the flowchart (Fig. 7.8), a 3D material parameter DOE containing  $H$  points is designed in each iteration, expressed by matrix  $\mathbf{c} = [\mathbf{c}_1, \mathbf{c}_2, \mathbf{c}_3] = [\mathbf{c}^1, \mathbf{c}^2, \mathbf{c}^3, \dots, \mathbf{c}^K]^T$ . Let  $\varepsilon_f(\mathbf{c})$  denotes the  $K \times 3$ -dimensional fracture strain computed based on the stress state histories in local critical elements. The surrogate model of the fracture strain prediction  $\varepsilon_f(\mathbf{c})$  for the whole DOE space is constructed using the method of diffuse approximation:

$$\tilde{\varepsilon}_f(\mathbf{c}) = \mathbf{p}(\mathbf{c})^T \mathbf{a}(\mathbf{c}) \quad (7.7)$$

where  $\mathbf{p} = [p_1, p_2, p_3, \dots]^T$  is the polynomial basis vector. In 3D case, the polynomial basis vector expressed in terms of the material parameters for the MMC3 criterion:

$$\mathbf{p} = [1, c_1, c_2, c_3, \dots]^T \quad (7.8)$$

The vector of coefficients  $\mathbf{a} = [a_1, a_2, a_3, \dots]^T$  is the minimizer of function defined by:

$$J(\mathbf{a}) = \frac{1}{2} \sum_{k=1}^K w(\|\mathbf{c} - \mathbf{c}_k\|) (\mathbf{p}^T \mathbf{a} - \varepsilon_f(\mathbf{c}_k))^2 \quad (7.9)$$

where  $w(\|\mathbf{c} - \mathbf{c}_k\|)$  is Gaussian weighting function depending on the Euclidean distance  $d$  between  $\mathbf{c}$  and  $\mathbf{c}_k$ :

$$w(\|\mathbf{c} - \mathbf{c}_k\|) = e^{-(d/h)^2} \quad (7.10)$$

in which  $h$  is a fixed parameter reflecting the anticipated spacing between neighboring points. It can be used to smooth the small fluctuation in data.

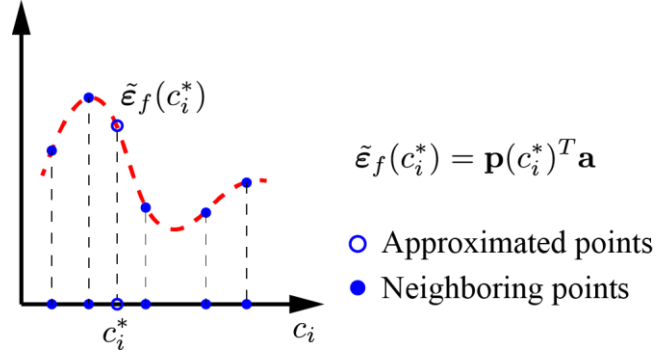


Figure 7.9: Illustration of the diffuse approximation procedure used to estimate the fracture strain surrogate model.

Fig. 7.9 illustrates the approximation procedure for a given fracture strain value of DOE training point. The corresponding approximated values for the whole design space are locally interpolated using diffuse approximation. Therefore, we construct the surrogate model including the *LSE*. between approximated and experimental fracture strain for each specimen, given by Eq. (7.3). A set of optimal parameters are identified in each iteration by minimizing the objective function.

## 7.5. Design and transformation of DOE

In Section 7.4, a diffuse approximation approach is presented to construct the surrogate model. The surrogate model uses a set of experiments in the design space to determine an optimum approximation. Numerical experiments are performed in local critical elements for this set of points in the DOE. The method used to design and transform DOE space is schematically depicted in Fig. 7.10.

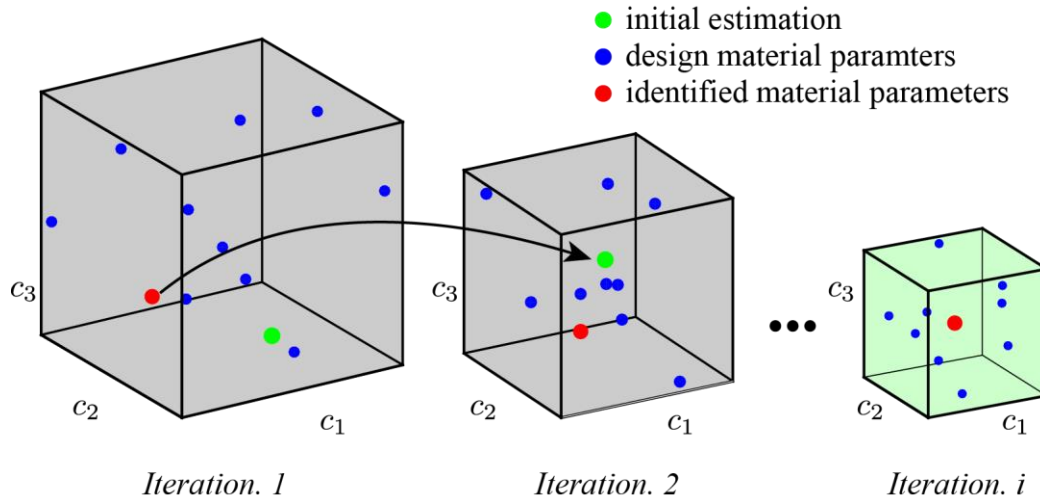


Figure 7.10: Illustration of the DOE design and transformation.

As illustrated in Fig. 7.10, the main idea behind this method is to use an initial estimation (green points in Fig. 7.10) within a sufficiently large design space at the beginning to select the experimental points (blue dots). It must guarantee that the first design space is big enough to consist of the solution that gives the best fit. After that, the identified points (red points) determined using Eq. (7.3) is used as the new center of design space with a smaller size or variation to reselect the experimental points. This procedure is repeated until convergence is reached. In the converged iteration, the center and identified points may be overlapped or located nearby.

## 7.6. Validation on DP590 steel

### 7.6.1 Mesh dependency of MMC3 fracture criterion

Generally, the MMC3 fracture criterion is a strain-based model; thus, the simulation result is dramatically affected by the mesh size. Essentially, high strain gradients are persistent in necking zones so that the calculated normalized load-displacement curves and fracture onset displacements are highly dependent on the mesh size. Therefore, before applying our proposed calibration method, a convergence study of mesh size is preformed to determine an appropriate element size that can be utilized in this work.

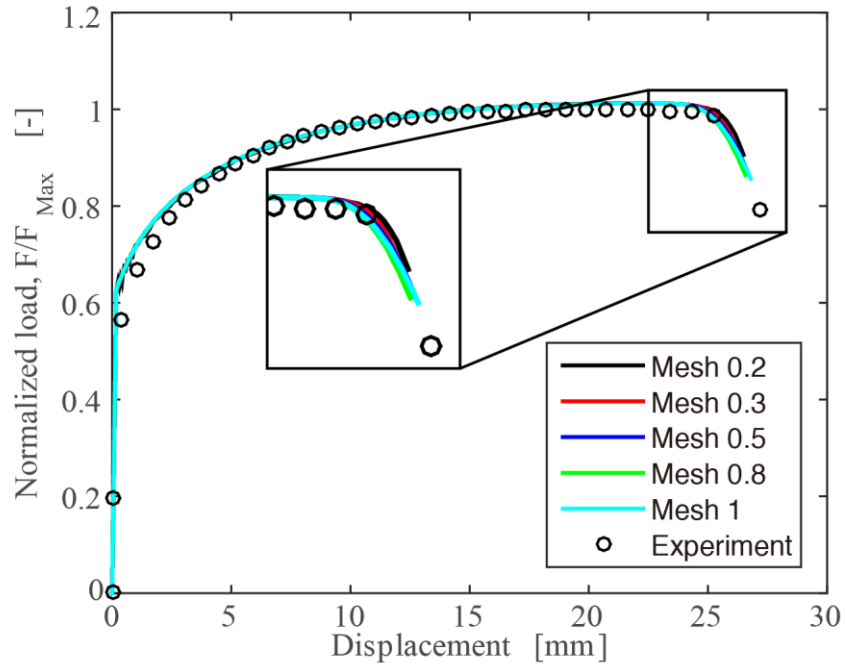


Figure 7.11: Mesh dependent normalized load-displacement curves obtained for the smooth tensile specimen.

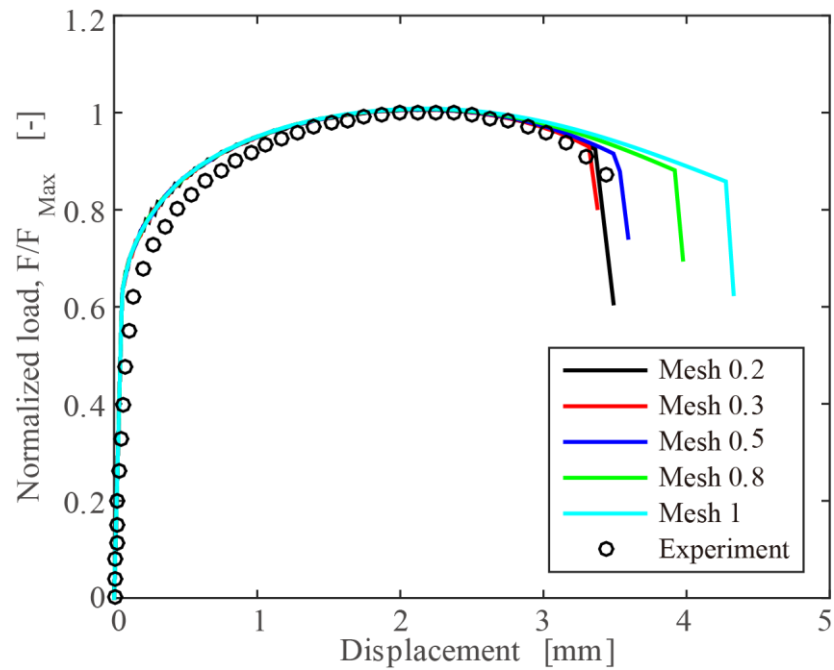


Figure 7.12: Mesh dependent normalized load-displacement curves obtained for the R20 mm notched tensile specimen.

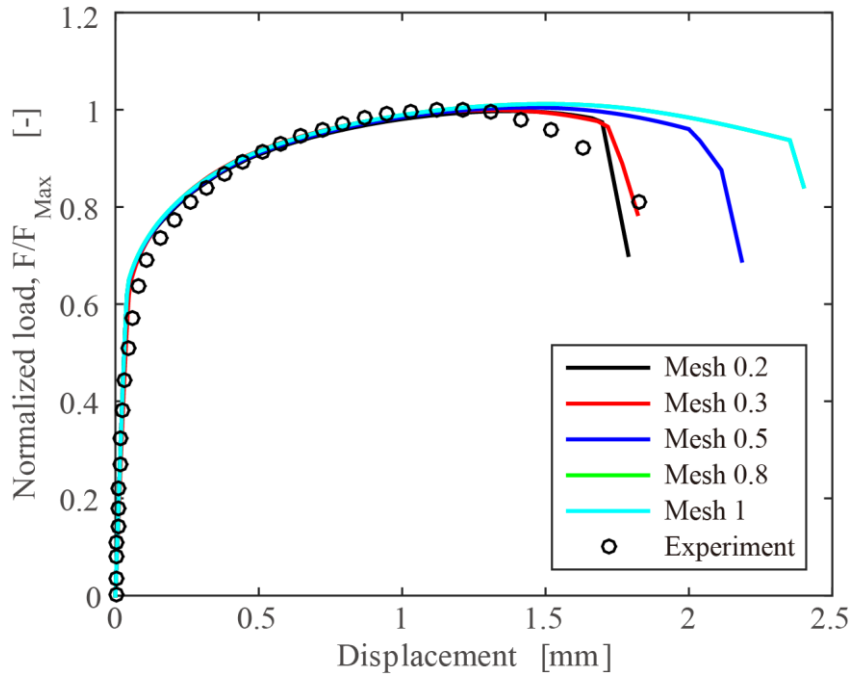


Figure 7.13: Mesh dependent normalized load-displacement curves obtained for the R1 mm notched tensile specimen.

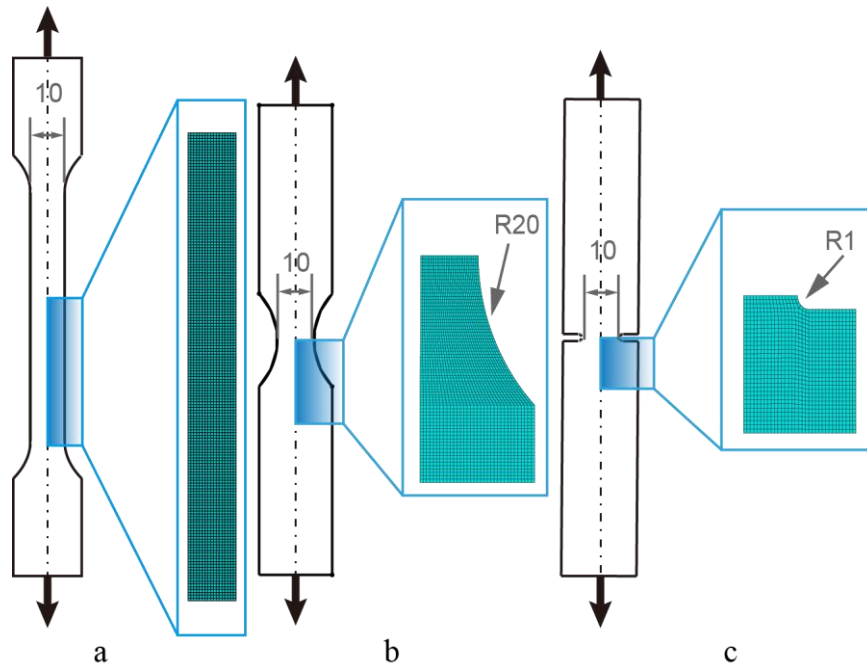


Figure 7.14: FE model with element length of 0.3 mm of: (a) smooth, (b) R20 mm and (c) R1 mm notched specimens.

Figs. 7.11-7.14 illustrate the mesh size dependency of the normalized load-displacement curves obtained for the smooth and notched tensile specimens, with element



length varying from 0.2 mm to 1 mm. For the smooth tensile test, the difference resulted from the mesh size is obvious. But, in other two cases, it has a dramatic influence on the simulation results. Convergence is reached when element length comes to 0.3 mm (red solid lines) or less than 0.3 mm. In order to guarantee the accuracy of the calculation and reduce the computational cost, the converged element length of 0.3 mm is adopted in the calibration process, as shown in Fig. 7.14.

### 7.6.2 MMC3 fracture criterion calibration for DP590 steel

The methodology discussed in the previous sections is used to extract the MMC3 criterion parameters from the current fracture tests. A quadric polynomial basis (second-order), consisting of 10 terms, is adopted to construct the surrogate model in Eq. (7.3). In each iteration, 11 training experiments are chosen from the DOE using latin hypercube sampling (LHS) approach. The identified solution of each iteration step is determined based on the fracture strain approximation for the whole DOE space. After that, the resulted material parameters are introduced in the global fracture test model. The adaptive correlation between the displacement and strain at the fracture onset, is computed to overcome the limitation of the current test plan. Hence, the three free parameters of MMC3 fracture criterion for DP590 steel are identified using the convergence condition given by:

$$\text{Argmin } LSE. = \frac{1}{m} \sum_{i=1}^m \left( d_{fi} - d_{fi}^{exp} \right)^2 \quad (7.11)$$

The error in the identification process is also presented by the *LSE*. between the measured and predicted fracture onset strain and displacement in each tensile specimen.

Based on experience of numerous numerical experiments, first calibration process is begun with the initial guess of material parameters, (0.1, 600 MPa, 1.03), within the reasonable ranges of the first DOE:  $c_1 \in [0, 0.2]$ ,  $c_2 \in [450, 650]$  (unit: MPa) and  $c_3 \in [0.9, 1.3]$ .

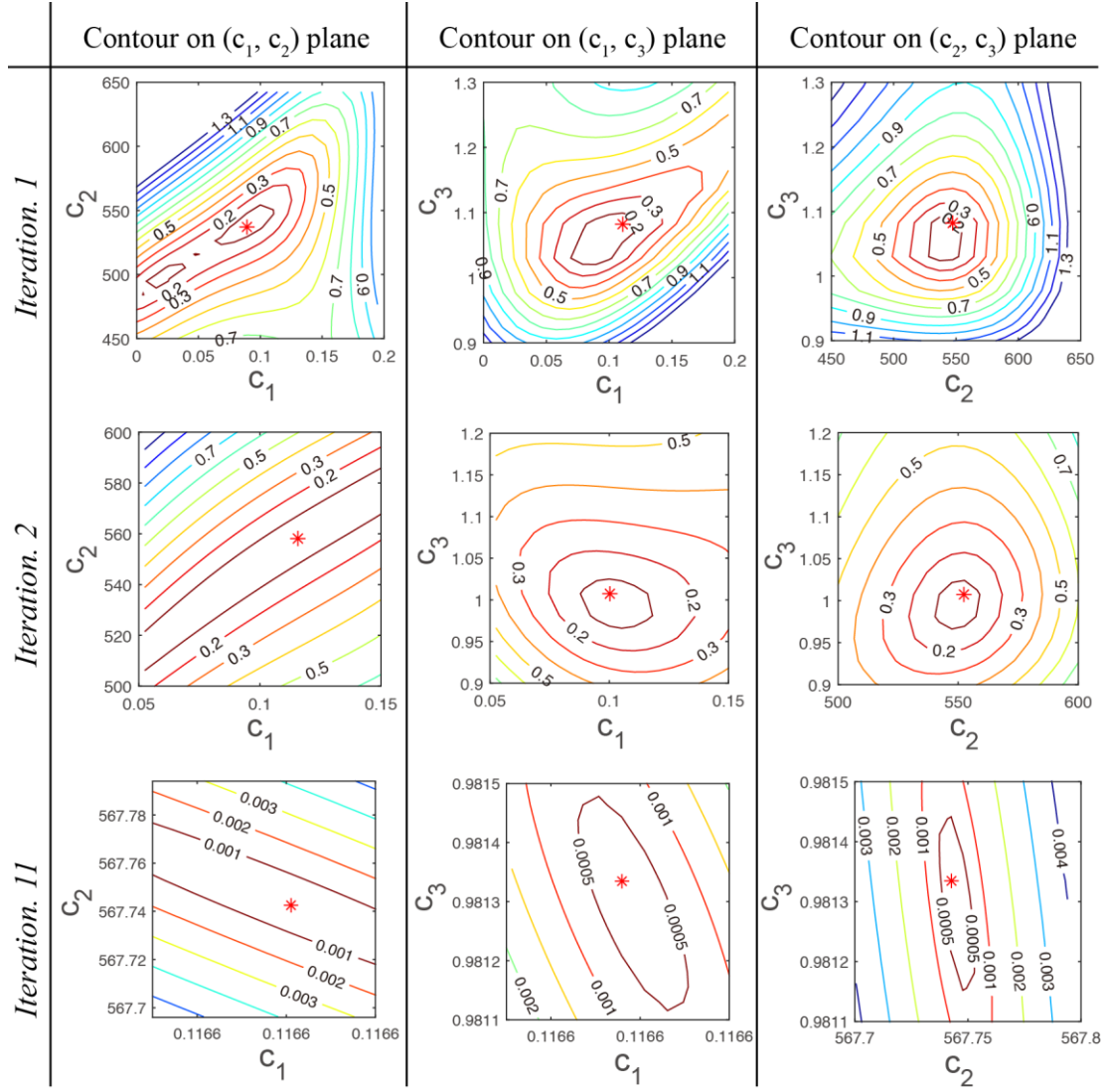


Figure 7.15: Projected contours of the LSE. using the surrogate model between the experimental and approximated fracture strain on various parameter planes.

Successive design spaces and corresponding *LSE*. obtained from the surrogate model between the experimental and approximated fracture strains of Iteration 1, 2 and 11 are shown in Fig. 7.15. Since the surrogate model is four-dimensional, projected contours on various planes are given to illustrate its tendency. The red star in each design space represents the identified material parameters for the corresponding iteration. For example, the identified parameters are (0.094, 542.105 MPa, 1.086) and (0.103, 550 MPa, 0.994) in the first and second iteration, respectively. During the subsequent iterations, the DOE size reduces until the converged results are obtained. When it comes to Iteration 11, material parameters vary only within a small range of  $10^{-4}$  for  $c_1$ , 0.1 MPa for  $c_2$ , and  $0.5 \times 10^{-3}$  for  $c_3$ .

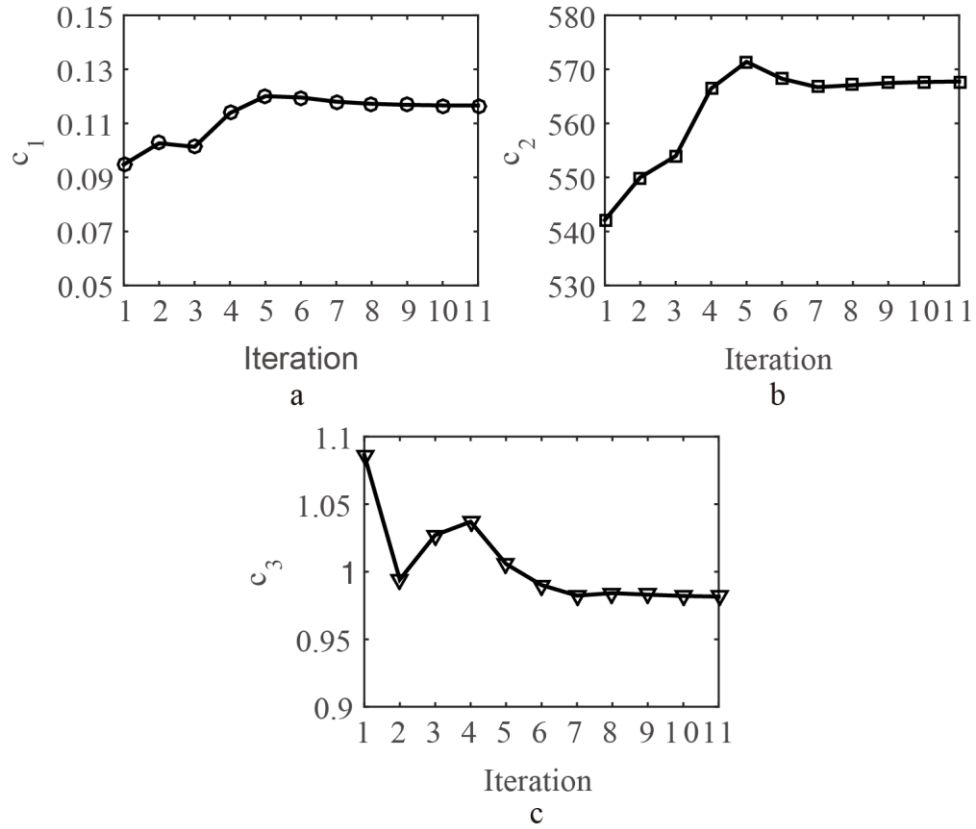


Figure 7.16: Convergence curves for the parametric identification of (a)  $c_1$ , (b)  $c_2$  (unit: MPa) and (c)  $c_3$ .

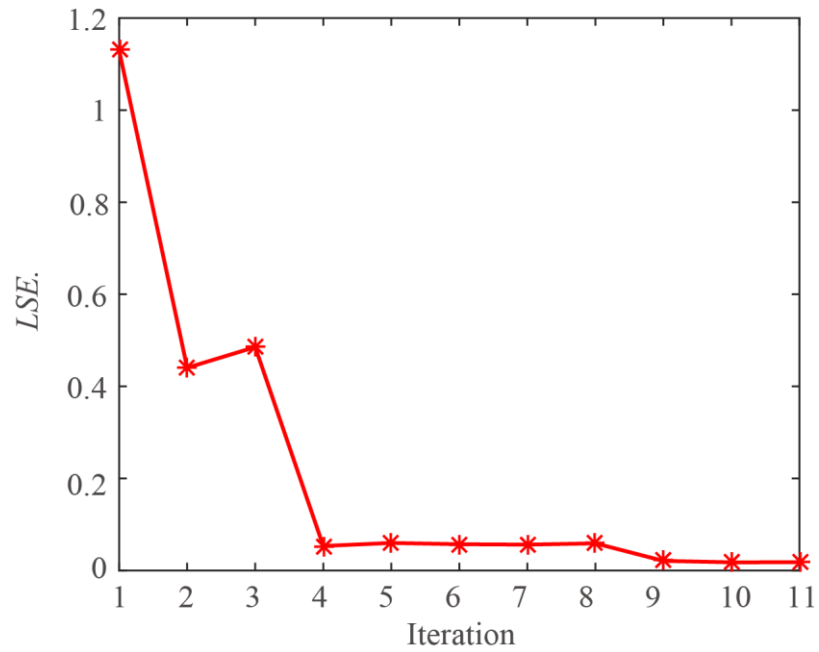


Figure 7.17: Progressive reduction of the LSE. between experimental and simulated fracture onset displacements with identified material parameters.

Fig. 7.16a, b and c show convergence curves for the parametric identification of  $c_1$ ,  $c_2$  and  $c_3$ , respectively. These results clearly indicate that after Iteration 7, each material parameter fluctuates around the converged value. Fig. 7.17 illustrates the progressive reduction of the  $LSE$  between the experimental and simulated fracture onset displacements with the identified material parameters from global FE simulation. Obvious decreases are found, and it stabilized at around 0.02 after 9-th iteration. Note that, the  $LSE$  is more reliable if the design space is smaller for each iteration. This is the reason why the result of Iteration 11 is more suitable than that of Iteration 9. And, the final identified material parameters for MMC3 fracture criterion are achieved as (0.117, 567.748 MPa, 0.982) in the first application.

### 3.6.3 Validation of robustness

In this work, we also aim to minimize the  $LSE$  between the experimental and simulated fracture onset displacements. Our first application to calibrate the material parameters of MMC3 fracture criterion for DP590 steel, shows that the bi-level reduced surrogate model has the capability to achieve this goal.

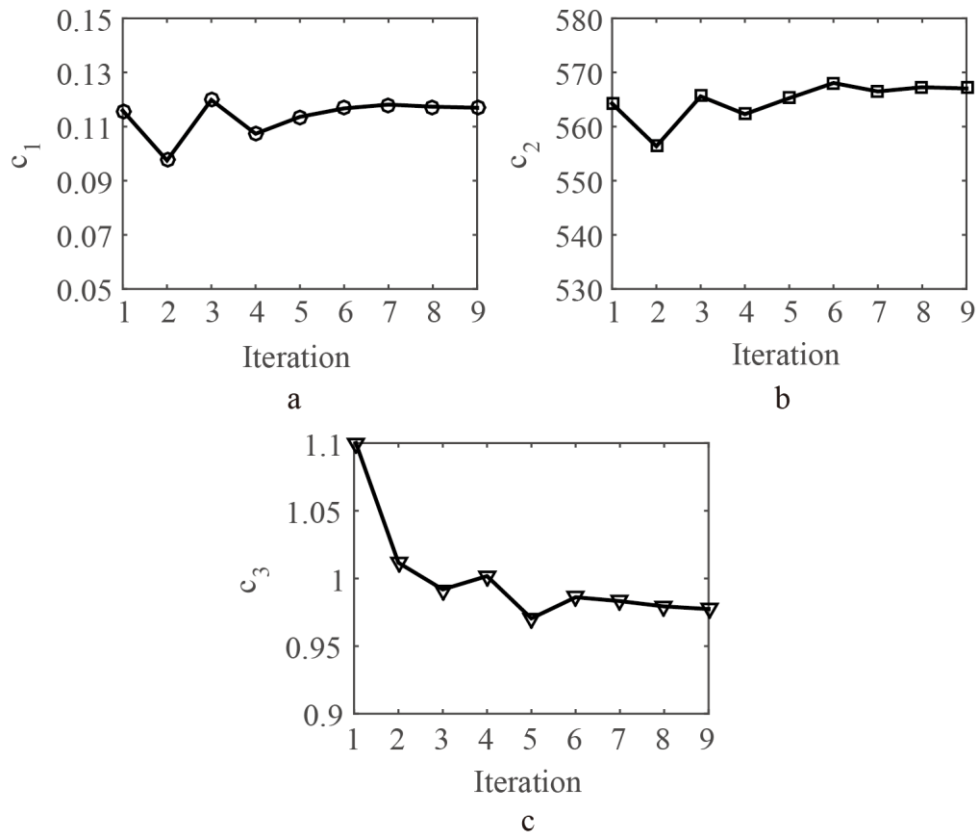


Figure 7.18: Convergence curves for the parametric identification of (a)  $c_1$ , (b)  $c_2$  (unit: MPa) and (c)  $c_3$ , with second group of initial parameter values.

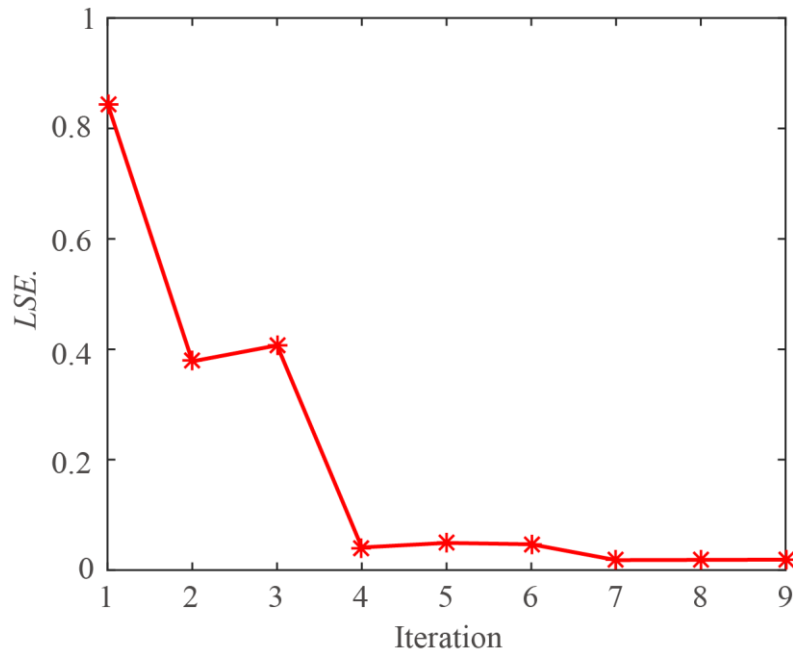


Figure 7.19: Progressive reduction of the  $LSE$ . between experimental and simulated fracture onset displacements with identified material parameters for the second application.

In order to check the robustness of the proposed method, a second application with different initial values of material parameters (0.05, 550 MPa, 1.1) to begin the iteration computation is performed. The same design space ranges with the first application are used.

In addition, the corresponding convergence curves are depicted in Fig. 7.18a, b and c. In this case, the fluctuation of each parameter stabilizes after 6 iterations. Fig. 7.19 shows the corresponding relationship of iteration number and  $LSE$ . between the experimental and simulated fracture onset displacements with those identified material parameters. At Iteration 7, the  $LSE$ . has already reduced to 0.02. Therefore, the final identified material parameters are chosen from 9th iteration, as (0.117, 567.039 MPa, 0.978). These results indicate a close agreement with the first application case, while the discrepancy is negligible. The negligible discrepancy is arisen from the proposed DOE and its transformation algorithms, which can be reduced by increasing the number of iterations. This comparison clearly shows that the calibration is independent of the initial guess; thus, it confirms the robustness of the calibration process for this MMC3 fracture criterion.

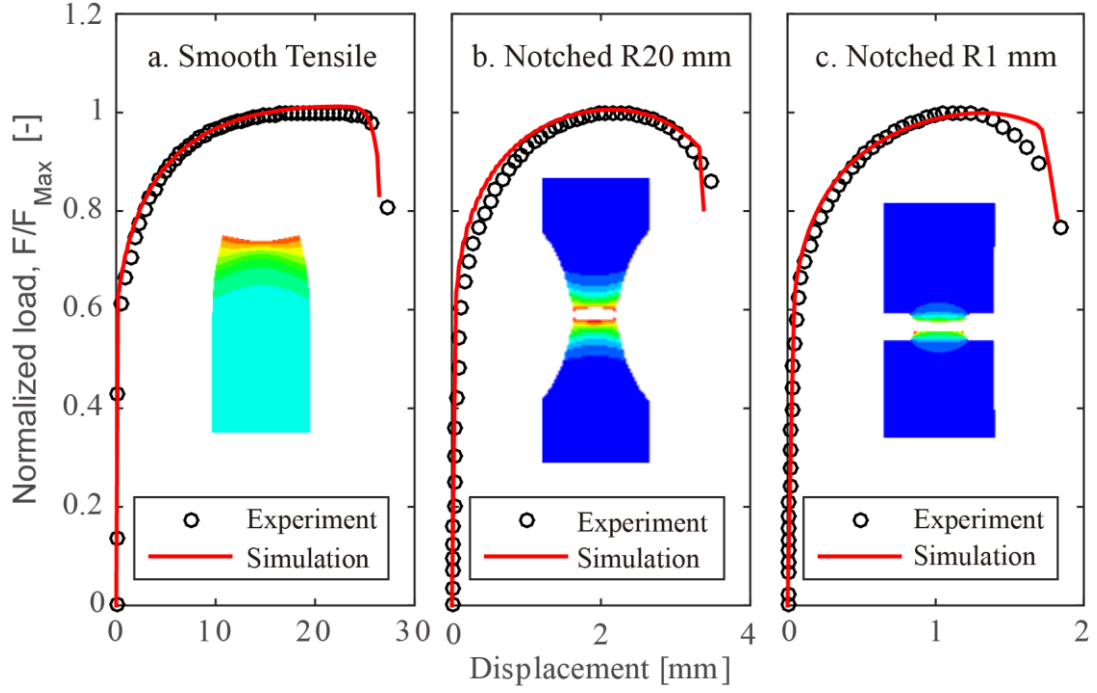


Figure 7.20: Comparison between simulated and measured load-displacement curves for (a) smooth, notched tensile specimens with (b) 20 mm and (c) 1mm open cutouts.

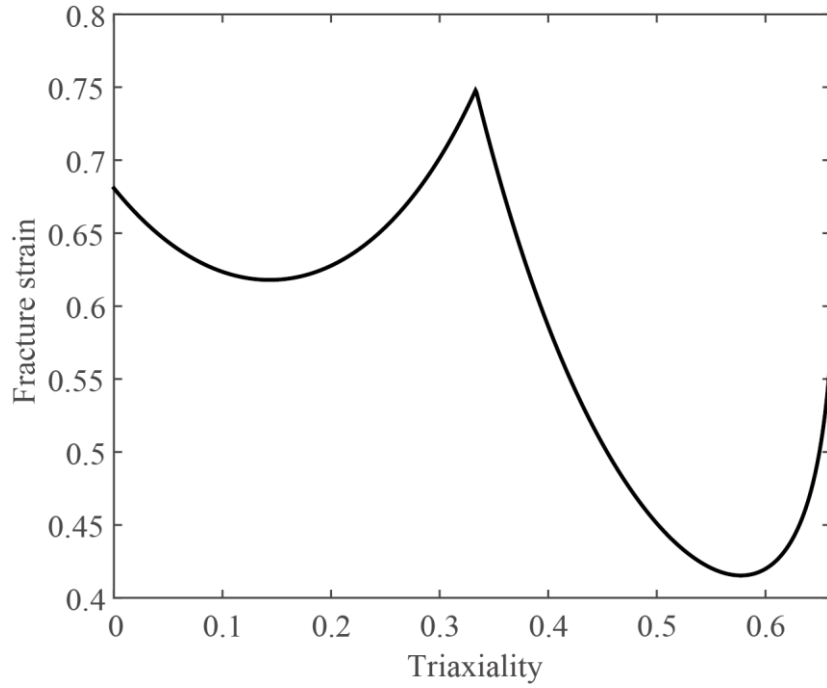


Figure 7.21: Fracture locus of the MMC3 fracture criterion with identified material parameters:  $c_1 = 0.117$ ,  $c_2 = 567.748 \text{ MPa}$  and  $c_3 = 0.982$ .

For the validation purpose, comparisons of the normalized load-displacement curves acquired from the measurements and simulation with identified material parameters are depicted in Fig. 7.20. A good agreement is obtained between the measurements and predictions.

The fracture locus of the MMC3 fracture criterion with identified material parameters is plotted in Fig. 7.21. The MMC3 fracture model shows a complex dependency on the stress triaxiality. For low stress triaxialities ( $0 < \eta < 1/3$ ), the fracture strain reveals as U-shape function of triaxiality. While for the intermediate triaxialities ( $1/3 < \eta < 2/3$ ), the fracture strain firstly decreases with triaxiality, and then it changes its path to rise rapidly.

## 7.7. Conclusions

The ductile fracture has been investigated extensively over decades. Numerous efforts have been done to calibrate the ductile fracture models with massive quantity of experimental tests. In this paper, a bi-level reduced surrogate model, which requires quite a limited number of tests, has been proposed to identify the material parameter of the MMC3 fracture criterion. The proposed method includes diffuse approximation and design of experiments (DOE) approaches to construct the surrogate model.

The bi-level reduced surrogate model is successfully implemented to build local critical element and global fracture tensile test models in each iteration. At the local level, latin hypercube sampling (LHS) algorithm is adopted to select finite number of training points, in which the corresponding fracture strains are computed. Diffuse approximation is utilized to construct the surrogate model of fracture strain that ensures the accuracy as well as reduces the computational cost. By minimizing the *LSE* between the approximated and measured fracture strains, identified parameters are determined and introduced in the global model. At the global level, the relevant fracture onset displacements are obtained using fracture tensile test simulations. Consequently, an adaptive correlation term between fracture onset strain and displacement is computed to update the target fracture strain in the subsequent iteration steps. Meanwhile, the new design space of material parameters is redesigned to reduce its size and center with the identified values. The proposed identification method helps to simplify the calibration of the MMC3 fracture criterion.

Our protocol was validated for DP590 steel with the use of numerical simulations and experimental results. During the first trial of the proposed model, the converged solution is achieved at 11th iteration, while the second trial only required 9 iteration steps. Results obtained from these two trials show a close agreement; this scenario indicates the robustness of this model to identify the material parameters. Further investigation on the robustness of the proposed method has been confirmed with different initial parameter guesses. Moreover, the predicted load-displacement curves using the identified material parameters concurs the experimental results. This study provides a novel numerical technique to identify the material parameters of ductile fracture criterion based on a surrogate model. It could be implemented for different ductile materials and further extended to take account of strain-rate or temperature effect.



## Chapter 8

### Conclusions and perspectives

In this work, we have investigated firstly in Part I the plastic behaviors of dual-phase (DP) steel using micromechanical modelling framework and asymptotic homogenization method by two ingredients: real and artificial microstructures. In contrast to the conventional methods, we develop a novel artificial microstructure generator to reconstruct the microstructural representation of multiphase materials, which are practically obtained from heat treatments.

In order to predict the flow stress of DP steel, the micromechanical modelling framework based on real material microstructures have been investigated in Chapter 3. We have developed an image analysis procedure that can directly transfer the microscopic observation (LOM or SEM) to FE model. The flow curve of each constituent phase is obtained using a dislocation based theory, in which the material parameters related to strain hardening are computed using the local chemical composition. With regard to the computational and calculation accuracy in the microscopic scale, periodic boundary condition (PBC) has been adopted associated with the asymptotic extension homogenization (AEH) method. Predictions of flow stress for DP590 and DP600 steels using this framework are in good agreement with experimental measurements or literature details.

With regard to computational and experimental requirements due to RVE construction of multiphase materials, in Chapter 4 a novel artificial microstructure generator is proposed based on modified Voronoï tessellation and material topology optimization design. Halton sequence is adopted to obtain the modified tessellation that is considered as the polycrystalline aggregate for the microstructure of DP steel. During the generation process, two microstructure parameters have been introduced to describe the phase distribution at microscopic scale. The proposed phase assignment algorithm defines a “pseudo-density” within each Voronoï cell that deduces the discrete value problem to a continuous one. Tailored DP microstructures have been convergently and rapidly. Additionally, a proper orthogonal decomposition (POD) approach has been integrated to identify the optimal

controlling parameters for certain DP steel. Therefore, optimal RVEs have been generated and the corresponding predictions of flow stress concurs the experimental measurements. Based on the identification of various DP steels, the correlation between these controlling parameters is calculated using polynomial interpolation.

We have investigated the plastic behaviors of DP steel using micromechanical modelling approaches. In the observation of microscopic simulation, the path of shear bands that are around  $45^\circ$  to the loading direction, occur in the ferritic phase. It indicates that, as plastic flow accumulating, micro-cracks can be formed and propagated in the strain localization zones. Therefore, in Part II we have also investigated the ductile fracture and damage mechanism, which can be utilized to describe and predict the ductile fracture in DP steel.

In pursuing reduction of experimental and computational costs, a bi-level reduced surrogate model has been proposed in Chapter 7 to identify the material parameters of the MMC3 fracture criterion. With our protocol that cooperates with diffuse approximation and design of experiments (DOE), the identification work only requires quite a limited number of fracture tests. In the bi-level method, training points have been selected according to latin hypercube sampling (LHS) algorithm. At the local level, the corresponding fracture strain of each design point is calculated using the stress states history of the local critical element. The surrogate model of fracture strain is approximated based on diffuse approximation. By minimizing the least square error (*LSE*.) between the approximated and measured fracture strains, identified parameters are determined and introduced in the global model. Fracture tensile test simulations have been performed to compute the relevant fracture displacement, which is utilized to compute an adaptive correlation term between fracture displacement and strain. Afterwards, the target fracture strain is updated according to this correlation term in the following iteration step. In the meanwhile, our DOE transformation algorithm centers with the identified values and reduces the variation size. Via successive iteration steps, the converged solution has been achieved for DP590 steel. The predicted force-displacement curves using the identified material parameters agree well with the experimental results.

In our work, we have developed several numerical approaches to investigate and predict both of the plasticity and damage behaviors of DP steel. To the best knowledge of the author, multiscale modelling of heterogeneous materials is a relatively new field that there still exist many difficulties, especially the damage and large

strain cases. Many potential developments for the proposed multiscale modelling framework can be carried out with respect to any of the three ingredients: homogenization, fracture and damage modelling and reduced-order modelling. In the following we give our perspectives on potential extensions based on the proposed multiscale modelling framework:

- As can be observed from Figs. 3.12 and 4.18, the presence of shear bands in ferritic matrix (mostly along the phase interface) results from inhomogeneous microstructures. These bands may result in the initial material failure or crack at microscopic scale. Therefore, there is necessity to introduce proper fracture or damage mechanisms in different phase materials and interface of the micromechanical model. Moreover, the macroscopic mechanical properties need to be computed using the extension of the asymptotic homogenization approach in two- or multi- field volumetric finite element (FE) simulation.
- In Chapters 3 and 4, we have developed 2D representative volume element (RVE) construction framework for DP steel and multiphase materials. By comparing with experimental results, small discrepancies have been observed that, the predictions of 2D RVE simulations are slightly higher than exact ones. We have attributed these discrepancies to the utilization of plane strain assumption in our numerical simulations. In order to eliminate these discrepancies, our artificial microstructure generator needs to be extended into 3D case. To overcome the key difficulty of huge computation, reduced-order modelling approaches could be applied. In addition, to generate the multiphase microstructure due to practical heat treatments or composite structures, the extension of our proposed phase assignment procedure will be implemented for multiphase materials, which include more than two phases.
- As discussed in Chapter 7, the material parameter identification of modified Mohr-Coulomb (MMC) fracture criterion has been performed using surrogate model. In future work, our identification protocol could be extended to different ductile fracture criteria that consist of more parameters unknown, such as Gurson-type models. Alternatively, the shape manifold learning approach may replace the diffuse approximation to speed the

identification procedure. Additionally, it could benefit to handle higher-order and sophisticated problems.

- Online multiscale modelling of fracture and damage behaviors of heterogeneous material has not been implemented in recent scientific research. Each material point of the macroscopic model could be represented by specific RVE, which may be considered as the microscopic model. During the loading process on macroscopic structure, the stress state of each material point is obtained from FE analysis. Therefore, the micromechanical modelling could be performed by prescribing with boundary conditions, which are related to the corresponding stress state in the material point. The macroscopic mechanical properties, especially the damage indicator at macroscopic scale are homogenized based on the computation of RVE simulation.



## References

- [1] L. Larson, Dreams to automobiles, 2008, United States.
- [2] S. Watts, The People's Tycoon: Henry Ford and the American Century, 2006, United States.
- [3] C.M. Tamarelli, The Evolving Use of Advanced High-Strength Steels for Automotive Applications, Department of Materials Science and Engineering, University of Michigan, United States, 2011, report.
- [4] R.H. Wagoner, Advanced High Strength Steel Workshop, Department of Materials Science and Engineering, The Ohio State University, United States, 2006, report.
- [5] V. Uthaisangskuk, U. Prael, W. Bleck, Modelling of damage and failure in multiphase high strength DP and TRIP steels, Engineering Fracture Mechanics, Volume 78, Issue 3, February 2011, Pages 469-486.
- [6] A. Pineau, matériaux et mobilité, Saint-Germain en Laye, 2012.
- [7] D.K. Matlock, J.G. Speer, E. De Moor, Recent AHSS Developments for Automotive applications: Processing, Microstructures, and Properties, I Advanced High-Strength steels for Automotive light weighting, USCAR offices, Southfield, 2012.
- [8] I.N. Paralikas, Cold roll forming process energy efficiency optimization, University of Patras, Greece, 2012, PhD thesis.
- [9] V.H. Baltazar, Hermamdez, S.S. Nayk, Y. Zhou, Tempering of Martensite in Dual-Phase Steels and Its Effects on Softening Behavior, The minerals, Metals & Materials Society and ASM International, Metallurgical and Materials Transaction A, 2011.
- [10] C. Landron, Ductile damage characterization in Dual-Phase steels using X-ray tomography, INSA-Lyon, France, 2011, PhD thesis.
- [11] C. Landron, E. Maire, J. Adrien, O. Bouaziz, L. Lecarme, A. Bareggi, Validation of void growth models using X-ray micro tomography characterization of damage in dual phase steels, Acta Materialia, Volume 59, Issue 20, December 2011, Pages 7564-7573.

- [12] B. Krebs, A. Hazotte, L. Germain, M. Gouné, Quantitative analysis of banded structures in Dual-Phase steels, *Image Analysis & Stereology*, Volume 29, 2010, Pages 85-90.
- [13] M.S. Niazi, Plasticity induced anisotropic damage modeling for forming processes, University of Twente, Netherlands, 2012, PhD Thesis.
- [14] Dual Phase steels, ArcelorMittal, United Kingdom, 2015, report.
- [15] S. Allain, Comportment mécanique des aciers: des mécanismes fondamentaux à la deformation macroscopique, thesis to obtain the academic accreditation to supervise research, HDR, Lorraine University, 2012.
- [16] J. Fansi, Prediction of DP steel fracture by FEM simulations using an advanced Gurson model, Université de Liège, Belgium, 2013, PhD thesis.
- [17] V. Uthaisangsuk, U. Prah, W. Bleck, Failure modeling of multiphase steels using representative volume elements based on real microstructures, *Procedia Engineering*, Volume 1, Issue 1, July 2009, Pages 171-176.
- [18] X. Sun, K.S. Choi, A. Soulami, W.N. Liu, M.A. Khaleel, On key factors influencing ductile fractures of dual phase (DP) steels, *Materials Science and Engineering: A*, Volume 526, Issues 1–2, 25 November 2009, Pages 140-149.
- [19] W. Wang, X. Wei, The effect of martensite volume and distribution on shear fracture propagation of 600–1000 MPa dual phase sheet steels in the process of deep drawing, *International Journal of Mechanical Sciences*, Volume 67, February 2013, Pages 100-107.
- [20] H. Hosseini-Toudeshky, B. Anbarlooie, J. Kadkhodapour, G. Shadalooyi, Microstructural deformation pattern and mechanical behavior analyses of DP600 dual phase steel, *Materials Science and Engineering: A*, Volume 600, 10 April 2014, Pages 108-121.
- [21] A. Ramazani, K. Mukherjee, U. Prah, W. Bleck, Modelling the effect of microstructural banding on the flow curve behaviour of dual-phase (DP) steels, *Computational Materials Science*, Volume 52, Issue 1, February 2012, Pages 46-54.
- [22] V. Uthaisangsuk, U. Prah, S. Münstermann, W. Bleck, Experimental and numerical failure criterion for formability prediction in sheet metal forming, *Computational Materials Science*, Volume 43, Issue 1, July 2008, Pages 43-50.

- [23] V. Uthaisangsuk, U. Prah, W. Bleck, Stretch-flange ability characterisation of multiphase steel using a microstructure based failure modelling, *Computational Materials Science*, Volume 45, Issue 3, May 2009, Pages 617-623.
- [24] V. Uthaisangsuk, S. Muenstermann, U. Prah, W. Bleck, H.-P. Schmitz, T. Pretorius, A study of microcrack formation in multiphase steel using representative volume element and damage mechanics, *Computational Materials Science*, Volume 50, Issue 4, February 2011, Pages 1225-1232.
- [25] J. Kadkhodapour, S. Schmauder, D. Raabe, S. Ziaei-Rad, U. Weber, M. Calcagnotto, Experimental and numerical study on geometrically necessary dislocations and non-homogeneous mechanical properties of the ferrite phase in dual phase steels, *ActaMaterialia*, Volume 59, Issue 11, June 2011, Pages 4387-4394.
- [26] F.M. Al-Abbasi, J.A. Nemes, Micromechanical modeling of the effect of particle size difference in dual phase steels, *International Journal of Solids and Structures*, Volume 40, Issues 13–14, June–July 2003, Pages 3379-3391.
- [27] H. Hosseini-Toudeshky, B. Anbarlooie, J. Kadkhodapour, Micromechanics stress-strain behavior prediction of dual phase steel considering plasticity and grain boundaries debonding, *Materials & Design*, Volume 68, March 2015, Pages 167-176.
- [28] S.A. Asgari, P.D. Hodgson, C. Yang, B.F. Rolfe, Modeling of Advanced High Strength Steels with the realistic microstructure–strength relationships, *Computational Materials Science*, Volume 45, Issue 4, June 2009, Pages 860-866.
- [29] National Institute of Standards and Technology, Object-Oriented Finite Element Program, Version 2.1.1, United States, 2015.
- [30] A. Ramazani, K. Mukherjee, H. Quade, U. Prah, W. Bleck, Correlation between 2D and 3D flow curve modelling of DP steels using a microstructure-based RVE approach, *Materials Science and Engineering: A*, Volume 560, 10 January 2013, Pages 129-139.
- [31] V. Uthaisangsuk, U. Prah, W. Bleck, Modelling of damage and failure in multiphase high strength DP and TRIP steels, *Engineering Fracture Mechanics*, Volume 78, Issue 3, February 2011, Pages 469-486.
- [32] A. Ramazani, Y. Li, K. Mukherjee, U. Prah, W. Bleck, A. Abdurakhmanov, M. Schleser, U. Reisgen, Microstructure evolution simulation in hot rolled DP600 steel during gas metal arc welding, *Computational Materials Science*, Volume 68, February 2013, Pages 107-116.



- [33] M.E. Kakhki, A. Kermanpur, M.Q. Golozar, Numerical simulation of continuous cooling of a low alloy steel to predict microstructure and hardness, *Modelling and Simulation in Materials Science and Engineering*, Volume 17, Issue 4, 2009, 045007.
- [34] M.E. Kakhki, A. Kermanpur, M.Q. Golozar, Three-dimensional simulation of quenching process of plain carbon steel gears incorporating phase transformations, *Materials Science and Technology*, Volume 28, Issue 2, 2012, Pages 197-204.
- [35] M.E. Kakhki, A. Kermanpur, M.Q. Golozar, Application of polymeric quenchant in heat treatment of crack-sensitive steel mechanical parts: modeling and experiments, *Materials & Design*, Volume 32, Issue 5, May 2011, Pages 2870-2877.
- [36] P. Ferro, Influence of phase transformations on the asymptotic residual stress distribution arising near a v-notch tip, *Modelling and Simulation in Materials Science and Engineering*, Volume 20, Issue 8, 2012, 045007.
- [37] M. Eshraghi, M.A. Tschopp, M.A. Zaeem, S.D. Felicelli, Effect of resistance spot welding parameters on weld pool properties in a DP600 dual-phase steel: A parametric study using thermomechanically-coupled finite element analysis, *Materials & Design*, Volume 56, April 2014, Pages 387-397.
- [38] F.M. Al-Abbasi, J.A. Nemes, Characterizing DP-steels using micromechanical modeling of cells, *Computational Materials Science*, Volume 39, Issue 2, April 2007, Pages 402-415.
- [39] G. Voronoï Nouvelles applications des paramètres continus à la théorie des formes quadratiques. Deuxième mémoire, recherches sur les parallélogrammes primitifs, *Journal für die reine und angewandte Mathematik*, Volume 134, 1908, Pages 198-287.
- [40] M. Nygård, P. Gudmundson, Micromechanical modeling of ferritic/pearlitic steels, *Materials Science and Engineering: A*, Volume 325, Issues 1–2, 28 February 2002, Pages 435-443.
- [41] M. Nygård, P. Gudmundson, Three-dimensional periodic Voronoi grain models and micromechanical FE-simulations of a two-phase steel, *Computational Materials Science*, Volume 24, Issue 4, July 2002, Pages 513-519.
- [42] N.H. Abid, R.K.A. Al-Rub, A.N. Palazotto, Computational modeling of the effect of equiaxed heterogeneous microstructures on strength and ductility of dual phase steels, *Computational Materials Science*, Volume 103, 1 June 2015, Pages 20-37.

- [43] A. Fillafer, C. Krempaszky, E. Werner, On strain partitioning and micro-damage behavior of dual-phase steels, *Materials Science and Engineering: A*, Volume 614, 22 September 2014, Pages 180-192.
- [44] K. Döbrich, C. Rau, C. Krill III, Quantitative characterization of the three-dimensional microstructure of polycrystalline Al-Sn using X-ray microtomography, *Metallurgical and Materials Transactions: A*, Volume 35, Issue 7, 2004, Pages 1953-1961.
- [45] F. Fritzen, T. Böhlke, E. Schnack, Periodic three-dimensional mesh generation for crystalline aggregates based on Voronoi tessellations, *Computational Mechanics*, Volume 43, Issue 5, 2009, Pages 701-713.
- [46] J. Halton, G. Smith, Radical inverse quasi-random point sequence, algorithm 247, *Communications of ACM*, Volume 7, 1964, Page 701.
- [47] M.P. Bendsøe, N. Kikuchi, Generating optimal topologies in structural design using a homogenization method, *Computer Methods in Applied Mechanics and Engineering*, Volume 71, Issue 2, 1988, Pages 197-224.
- [48] M.P. Bendsøe, O. Sigmund, *Topology Optimization: Theory, Methods, and Applications*, Springer Science & Business Media, 2013.
- [49] O. Sigmund, Materials with prescribed constitutive parameters: An inverse homogenization problem, *International Journal of Solids and Structures*, Volume 31, Issue 17, 1994, Pages 2313-2329.
- [50] O. Sigmund, A 99 line topology optimization code written in matlab, *Structural and Multidisciplinary Optimization*, Volume 21, Issue 2, 2001, Pages 120-127.
- [51] O. Sigmund, Morphology-based black and white filters for topology optimization, *Structural and Multidisciplinary Optimization*, Volume 33, Issue 4, 2007, Pages 401-424.
- [52] L. Xia, P. Breitkopf, Concurrent topology optimization design of material and structure within nonlinear multiscale analysis framework, *Computer Methods in Applied Mechanics and Engineering*, Volume 278, 15 August 2014, Pages 524-542.
- [53] L. Xia, P. Breitkopf, A reduced multiscale model for nonlinear structural topology optimization, *Computer Methods in Applied Mechanics and Engineering*, Volume 280, 1 October 2014, Pages 117-134.

- [54] L. Xia, P. Breitkopf, Multiscale structural topology optimization with an approximate constitutive model for local material microstructure, *Computer Methods in Applied Mechanics and Engineering*, Volume 286, 1 April 2015, Pages 147-167.
- [55] L. Xia, P. Breitkopf, Design of materials using topology optimization and energy-based homogenization approach in matlab, *Structural and Multidisciplinary Optimization*, Volume 52, Issue 6, 2015, Pages 1229-1241.
- [56] L. Xia, P. Breitkopf, Recent advances on topology optimization of multiscale nonlinear structures, *Archive of Computational Methods in Engineering*, 2016, Pages 1-23.
- [57] J.H. Zhu, W.H. Zhang, L. Xia, Topology optimization in aircraft and aerospace structures design, *Archive of Computational Methods in Engineering*, 2015, Pages 1-28.
- [58] M.P. Bendsøe, Optimal shape design as a material distribution problem, *Structural Optimization*, Volume 1, Issue 4, 1989, Pages 193-202.
- [59] M. Zhou, G.I.N. Rozvany, The COC algorithm, Part II: Topological, geometrical and generalized shape optimization, *Computer Methods in Applied Mechanics and Engineering*, Volume 89, Issue 1, 1991, Pages 309-336.
- [60] Y.M. Xie, G.P. Steven, A simple evolutionary procedure for structural optimization, *Computers & Structures*, Volume 49, Issue 5, 1993, Pages 885-896.
- [61] G. Allaire, F. Jouve, A.M. Toader, Structural optimization using sensitivity analysis and a level-set method, *Journal of Computational Physics*, Volume 194, Issue 1, 10 February 2004, Pages 363-393.
- [62] M. Burger, B. Hackl, W. Ring, Incorporating topological derivatives into level set methods, *Journal of Computational Physics*, Volume 194, Issue 1, 10 February 2004, Pages 344-362.
- [63] L. Xia, B. Raghavan, P. Breitkopf, W.H. Zhang, Numerical material representation using proper orthogonal decomposition and diffuse approximation, *Applied Mathematics and Computation*, Volume 224, 1 November 2013, Pages 450-462.
- [64] L. Meng, P. Breitkopf, B. Raghavan, G. Mauvoisin, O. Bartier, X. Hernot, Identification of material properties using indentation test and shape manifold learning approach, *Computer Methods in Applied Mechanics and Engineering*, Volume 297, 1 December 2015, Pages 239-257.

- [65] Y. Hou, T. Sapanathan, A. Dumon, P. Culi ère, M. Rachik, A novel artificial dual-phase microstructure generator based on topology optimization, *Computational Materials Science*, Volume 123, October 2016, Pages 188-200.
- [66] Y. Hou, A. Dumon, P. Culi ère, M. Rachik, Artificial microstructure generator for dual-phase steels, VII European Congress on Computational Methods in Applied Sciences and Engineering, Crete Island, Greece.
- [67] I. Gutierrez, A me modelling the mechanical behaviour of steels with mixed microstructures, *Metalurgija*, Volume 11, Issue 3, 2005, Pages 201-214.
- [68] P.T. Pinard, A. Schwedt, A. Ramazani, U. Prahl, S. Richter, Characterization of dual-phase steel microstructure by combined submicrometer EBSD and EPMA carbon measurements, *Microscopy and Microanalysis*, Volume 19, Issue 4, 2013, Pages 996-1006.
- [69] C. Thomser, Modelling of the mechanical properties of dual phase steels based on microstructure, RWTH-Aachen, Germany, 2009, Ph.D. thesis.
- [70] K. Terada, M. Hori, T.Kyoya, N. Kikuchi, Simulation of the multi-scale convergence in computational homogenization approaches, *International Journal of Solids and Structures*, Volume 37, Issue 16, April 2000, Pages 2285-2311.
- [71] Z. Xia, C. Zhou, Q. Yong, X. Wang, On selection of repeated unit cell model and application of unified periodic boundary conditions in micro-mechanical analysis of composites, *International Journal of Solids and Structures*, Volume 43, Issue 2, January 2006, Pages 266-278.
- [72] S. Gall ée, P. Pilvin, Deep drawing simulation of a metastable austenitic stainless steel using a two-phase model, *Journal of Materials Processing Technology*, Volume 210, Issues 6–7, 1 April 2010, Pages 835-843.
- [73] T Mori, K Tanaka, Average stress in matrix and average elastic energy of materials with misfitting inclusions, *Acta Metallurgica*, Volume 21, Issue 5, 1973, Pages 571-574
- [74] L. Brassart, H.M. Inglis, L. Delannay, I. Doghri, P.H. Geubelle, An extended Mori–Tanaka homogenization scheme for finite strain modeling of debonding in particle-reinforced elastomers, *Computational Materials Science*, Volume 45, Issue 3, May 2009, Pages 611-616.

- [75] Y.J. Wei, L. Anand, Grain-boundary sliding and separation in polycrystalline metals: application to nanocrystalline fcc metals, *Journal of the Mechanics and Physics of Solids*, Volume 52, Issue 11, November 2004, Pages 2587-2616.
- [76] P.W. Chung, K.K. Tamma, R.R. Namburu, Asymptotic expansion homogenization for heterogeneous media: computational issues and applications, *Composites Part A: Applied Science and Manufacturing*, Volume 32, Issue 9, September 2001, Pages 1291-1301.
- [77] H.J. Böhm, A short introduction to basic aspects of continuum micromechanics, Institute of Lightweight Design and Structural Biomechanics, Vienna University of Technology, August 2008, Technical report.
- [78] J.D. Eshelby, The Determination of the Elastic Field of an Ellipsoidal Inclusion, and Related Problems, *Proceedings of the Royal Society of London A: Mathematical, Physical and Engineering Sciences*, Volume 241, Issue 1226, August 1957, Pages 376-396.
- [79] B. Hassani, E. Hinton, A review of homogenization and topology optimization I—homogenization theory for media with periodic structure, *Computers & Structures*, Volume 69, Issue 6, December 1998, Pages 707-717.
- [80] MATLAB, User's Manual.
- [81] D. Krajcinovic, Damage mechanics, *Mechanics of Materials*, Volume 8, 1989, Pages 117-197.
- [82] X.H. Hu, X. Sun, S.F. Golovashchenko, Predicting tensile stretchability of trimmed AA6111-T4 sheets, *Computational Materials Science*, Volume 85, April 2014, Pages 409-419.
- [83] J.W. Saunders, L.N. Molino, F.L. Mckoy, Performance of seating systems in a FMVSS No. 301 rear impact crash test, 18th Enhanced Safety of Vehicles (ESV) Conference, 2003.
- [84] F. Abbassi, O. Pantalé S. Mistou, A. Zghal, R. Rakotomalala, Effect of ductile damage evolution in sheet metal forming: experimental and numerical investigations, *Key Engineering Materials*, Volume 446, July 2010, Pages 157-169.
- [85] G. Avramovic-Cingara, Y. Ososkov, M.K. Jain, D.S. Wilkinson, Effect of martensite distribution on damage behaviour in DP600 dual phase steels, *Materials Science and Engineering: A*, Volume 516, Issues 1–2, August 2009, Pages 7-1.

- [86] F.A. McClintock, A criterion for ductile fracture by the growth of holes, *Journal of Applied Mechanics*, Volume 35, Issues 1, 1968, Pages 363-371.
- [87] J.R. Rice, D.M. Tracey, On the ductile enlargement of voids in triaxial stress fields, *Journal of the Mechanics and Physics of Solids*, Volume 17, Issue 3, 1969, Pages 201-217.
- [88] A.L. Gurson, Continuum theory of ductile rupture by void nucleation and growth: Part I: Yield criteria and flow rules for porous ductile media, *Journal of Engineering Materials and Technology*, Volume 99, Issue 1, 1977, Pages 2-15.
- [89] V. Tvergaard, A. Needleman, Analysis of the cup-cone fracture in a round tensile bar, *Acta Metallurgica*, Volume 32, Issue 1, 1984, Pages 157-169.
- [90] J.B. Leblond, G. Perrin, J. Devaux, An improved Gurson-type model for hardenable ductile metals, *European Journal of Mechanics. A. Solids*, Volume 14, Issue 4, 1995, Pages 499-527.
- [91] T. Pardoen, J.W. Hutchinson, An extended model for void growth and coalescence, *Journal of the Mechanics and Physics of Solids*, Volume 48, Issue 12, December 2000, Pages 2467-2512.
- [92] Z.L. Zhang, C. Thaulow, J. Ødegård, A complete Gurson model approach for ductile fracture, *Engineering Fracture Mechanics*, Volume 67, Issue 2, 1 September 2000, Pages 155-168.
- [93] K. Nahshon, J.W. Hutchinson, Modification of the Gurson model for shear failure, *European Journal of Mechanics. A. Solids*, Volume 27, Issue 1, 2008, Pages 1-17.
- [94] Y. Bao, T. Wierzbicki, A comparative study on various ductile crack formation criteria, *Journal of Engineering Materials and Technology*, Volume 126, Issue 3, 2004, Pages 314-324.
- [95] Y. Bai, T. Wierzbicki, A new model of metal plasticity and fracture with pressure and lode dependence, *International Journal of Plasticity*, Volume 24, Issue 6, 2008, Pages 1071-1096.
- [96] Y. Bai, T. Wierzbicki, Application of extended Mohr-Coulomb criterion to ductile fracture, *International Journal of Fracture*, Volume 161, Issue 1, 2010, Pages 1-20.
- [97] D.P. Clausing, Effect of plastic strain state on ductility and toughness, *International Journal of Fracture Mechanics*, Volume 6, Issue 1, 1970, Pages 71-85.

- [98] J.W. Hancock, A.C. Mackenzie, On the mechanisms of ductile failure in high-strength steels subjected to multi-axial stress-states, *Journal of the Mechanics and Physics of Solids*, Volume 24, Issue 2, 1976, Pages 147-160.
- [99] G.R. Johnson, W.H. Cook, Fracture characteristics of three metals subjected to various strains, strain rates, temperatures and pressures, *Engineering Fracture Mechanics*, Volume 21, Issue 1, 1985, Pages 31-48.
- [100] D. Mohr, S. Henn, Calibration of stress-triaxiality dependent crack formation criteria: a new hybrid experimental–numerical method, *Experimental Mechanics*, Volume 47, Issue 6, 2007, Pages 805-820.
- [101] D. Mohr, M. Oswald, A new experimental technique for the multi-axial testing of advanced high strength steel sheets, *Experimental Mechanics*, Volume 48, Issue 1, 2008, Pages 65-77.
- [102] K.L. Lee, A.F. Whitehouse, P.J. Withers, M.R. Daymond, Neutron diffraction study of the deformation behaviour of deformation processed copper–chromium composites, *Materials Science and Engineering: A*, Volume 348, Issues 1–2, 15 May 2003, Pages 208-216.
- [103] Y. Barranger, P. Doumalin, J.C. Dupre, A. Germaneau, S. Hedan, V. Valle, Evaluation of three-dimensional and two-dimensional full displacement fields of a single edge notch fracture mechanics specimen, in light of experimental data using X-ray tomography, *Engineering Fracture Mechanics*, Volume 76, Issue 15, October 2009, Pages 2371-2383.
- [104] M. Dunand, D. Mohr, Hybrid experimental–numerical analysis of basic ductile fracture experiments for sheet metals, *International Journal of Solids and Structures*, Volume 47, Issue 9, 1 May 2010, Pages 1130-1143.
- [105] P. Lancaster, K. Salkauskas, Surfaces generated by moving least squares methods, *Mathematics of computation*, Volume 37, Issue 155, 1981, Pages 141-158.
- [106] B. Nayroles, G. Touzot, P. Villon, Generalizing the finite element method: diffuse approximation and diffuse elements, *Computational mechanics*, Volume 10, Issue 5, 1992, Pages 307-318.
- [107] P. Breitkopf, H. Naceur, A. Rassineux, P. Villon, Moving least squares response surface approximation: Formulation and metal forming applications, *Computers & Structures*, Volume 83, Issues 17–18, June 2005, Pages 1411-1428.

- [108] J. Lemaitre, A course on damage mechanics, Springer Science & Business Media, 2012.
- [109] M. Cockcroft, D. Latham, Ductility and the Workability of Metals, Journal Institute of Metals, Volume 96, 1968, Pages 33-39.
- [110] M.L. Wilkins, R.D. Streit, J.E. Reaugh, Cumulative-strain-damage model of ductile fracture: simulation and prediction of engineering fracture tests, Lawrence Livermore National Lab., CA (USA); Science Applications, Inc., San Leandro, CA (USA), 1980.
- [111] F. Cirak, M. Ortiz, A. Pandolfi, A cohesive approach to thin-shell fracture and fragmentation, Computer Methods in Applied Mechanics and Engineering, Volume 194, Issues 21–24, June 2005, Pages 2604-2618.
- [112] O. Mohr, Welche umstände bedingen die elastizitätsgrenze und denbruch eines materials, Zeitschrift des Vereins Deutscher Ingenieure, Volume 46, Issues 1524–1530, 1900, Pages 1572-1577.
- [113] T. Wierzbicki, L. Xue, On the effect of the third invariant of the stress deviator on ductile fracture, Impact and Crashworthiness Laboratory, Technical Report , 2005.
- [114] M. Dunand, D. Mohr, On the predictive capabilities of the shear modified Gurson and the modified Mohr–Coulomb fracture models over a wide range of stress triaxialities and Lode angles, Journal of the Mechanics and Physics of Solids, Volume 59, Issue 7, July 2011, Pages 1374-1394.
- [115] M.B. Bettaieb, X. Lemoine, O. Bouaziz, A. M. Habraken, L. Duchêne, Numerical modeling of damage evolution of DP steels on the basis of X-ray tomography measurements, Mechanics of Materials, Volume 43, Issue 3, March 2011, Pages 139-156.
- [116] J. Fansi, T. Balan, X. Lemoine, E. Maire, C. Landron, O. Bouaziz, M..B. Bettaieb, A.M. Habraken, Numerical investigation and experimental validation of physically based advanced GTN model for DP steels, Materials Science and Engineering: A, Volume 569, May 2013, Pages 1-12,
- [117] O. Bouaziz, E. Maire, M. Giton, J. Lamarre, Y. Salingue, M. Dimichiele, A model for initiation and growth of damage in dualphase steels identified by X-ray micro-tomography, Revue de Métallurgie, Volume 105, Issue 2, 2008, Pages 102-107.



- [118] E. Maire, O. Bouaziz, M.D. Michiel, C. Verdu, Initiation and growth of damage in a dual-phase steel observed by X-ray microtomography, *Acta Materialia*, Volume 56, Issue 18, October 2008, Pages 4954-4964.
- [119] C. Landron, E. Maire, O. Bouaziz, J. Adrien, L. Lecarme, A. Bareggi, Validation of void growth models using X-ray microtomography characterization of damage in dual phase steels, *Acta Materialia*, Volume 59, Issue 20, December 2011, Pages 7564-7573.
- [120] D. Mohr, M. Oswald, A new experimental technique for the multi-axial testing of advanced high strength steel sheets, *Experimental Mechanics*, Volume 48, Issue 1, 2008, Pages 65-77.
- [121] T.K. Eller, L. Greve, M.T. Andres, M. Medricky, A. Hatscher, V.T. Meinders, A.H. van den Boogaard, Plasticity and fracture modeling of quench-hardenable boron steel with tailored properties, *Journal of Materials Processing Technology*, Volume 214, Issue 6, June 2014, Pages 1211-1227.
- [122] G. Gruben, O.S. Hopperstad, T. Børvik, Evaluation of uncoupled ductile fracture criteria for the dual-phase steel Docol 600DL, *International Journal of Mechanical Sciences*, Volume 62, Issue 1, September 2012, Pages 133-146.
- [123] F. Ebnoether, D. Mohr, Predicting ductile fracture of low carbon steel sheets: Stress-based versus mixed stress/strain-based Mohr–Coulomb model, *International Journal of Solids and Structures*, Volume 50, Issues 7–8, April 2013, Pages 1055-1066.
- [124] T.S. Cao, A. Gaillac, P. Montmitonnet, P.O. Bouchard, Identification methodology and comparison of phenomenological ductile damage models via hybrid numerical–experimental analysis of fracture experiments conducted on a zirconium alloy, *International Journal of Solids and Structures*, Volume 50, Issue 24, November 2013, Pages 3984-3999.
- [125] J. Papasidero, V. Doquet, D. Mohr, Ductile fracture of aluminum 2024-T351 under proportional and non-proportional multi-axial loading: Bao–Wierzbicki results revisited, *International Journal of Solids and Structures*, Volumes 69–70, September 2015, Pages 459-474.
- [126] W.J. Roux, N. Stander, R.T. Haftka, Response surface approximations for structural optimization, *International Journal for Numerical Methods in Engineering*, Volumes 42, Issue 3, 1988, Pages 517-534.

- [127] N. Slander, The successive response surface method applied to sheet metal forming, First MIT Conference on Computational Fluid and Solid Mechanics, 2001.
- [128] V.K. Hombal, S. Mahadevan, Surrogate modeling of 3D crack growth, *International Journal of Fatigue*, Volume 47, February 2013, Pages 90-99.
- [129] H. Li, L. Gutierrez, H. Toda, O. Kuwazuru, W. Liu, Y. Hangai, M. Kobayashi, R. Batres, Identification of material properties using nanoindentation and surrogate modeling, *International Journal of Solids and Structures*, Volume 81, March 2016, Pages 151-159.
- [130] A. Ramazani, M. Abbasi, U. Prahl, W. Bleck, Failure analysis of DP600 steel during the cross-die test, *Computational Materials Science*, Volume 64, November 2012, Pages 101-105.
- [131] M. Abbasi, B. Bagheri, M. Ketabchi, D.F. Haghshenas, Application of response surface methodology to drive GTN model parameters and determine the FLD of tailor welded blank, *Computational Materials Science*, Volume 53, Issue 1, February 2012, Pages 368-376.
- [132] ABAQUS/Explicit: User's Manual, Vol. 1, Hibbitt, Karlsson and Sorenson Inc., 2001.
- [133] T. Wu, M. Coret, A. Combescure, Numerical simulation of welding induced damage and residual stress of martensitic 15-5PH, *International Journal of Solids and Structures*, Volume 45, Issues 18–19, September 2008, Pages 4973-4989.
- [134] F. Cheng, S.M. Kim, J.N. Reddy, R.K. Abu Al-Rub, Modeling of elastoplastic behavior of stainless-steel/bronze interpenetrating phase composites with damage evolution, *International Journal of Plasticity*, Volume 61, October 2014, Pages 94-111.

